

# The Christmas Storm 2016: Comparing Snow Observations and the Operational Forecast Model MEPS

Franziska Hellmuth



Thesis submitted for the degree of  
Master in Meteorology  
60 credits

Department of Geoscience  
Faculty of Mathematics and Natural Sciences

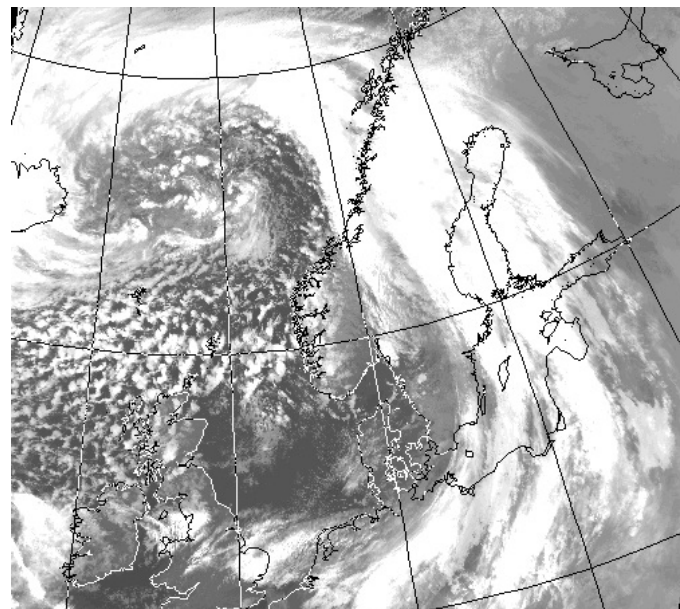
UNIVERSITY OF OSLO

June 2018



# **The Christmas Storm 2016: Comparing Snow Observations and the Operational Forecast Model MEPS**

Franziska Hellmuth



Satellite image of the extreme extratropical cyclone on 24 December 2016 at the coast of Norway. Image obtained from the Dundee Satellite Receiving Station <http://www.sat.dundee.ac.uk>.

© 2018 Franziska Hellmuth

The Christmas Storm 2016: Comparing Snow Observations and the Operational Forecast Model  
MEPS

<http://www.duo.uio.no/>

Printed: Reprocentralen, University of Oslo

## ABSTRACT

Previous studies showed the importance to have information about the vertical distribution of precipitation to simulate snow and related cyclone development correctly in regional, mesoscale models. During Christmas 2016, an extreme storm affected the local infrastructure of Eastern, Southern, and Western Norway. In this thesis, the Christmas storm 2016 is investigated for snow observations and the operational forecast model at Haukeliseter (991 m above sea level), Norway.

The WMO measurement site Haukeliseter is equipped with conventional meteorological instruments and a double fence snow gauge instrument to reduce wind effects and increase catch-ratios for frozen precipitation. In winter 2016/2017, three additional instruments were installed for a US National Science Foundation funded field campaign, to estimate snow water content in the column with the help of the optimal estimation retrieval. In November 2016, the AROME-MetCoOp ensemble prediction system (MEPS) became operational at the Norwegian Meteorological Institute. In this thesis, the extreme weather event is studied using European Centre for Medium-Range Weather Forecasts weather analysis, meteorological measurements, including double fence gauge and radar observations, optimal estimation retrieval, and MEPS.

During 21 and 26 December 2016, two cyclones as well as frontal passages affected Norway. Observed frozen and liquid precipitation is associated with the cyclones and the fronts. The meteorological analysis of surface properties from observations and MEPS forecasts agree on the passages of occlusions and warm sector. Wind speeds and surface precipitation amount are predicted too high by MEPS (mean absolute error: up to  $10 \text{ m s}^{-1}$  and 15 mm) during the entire event with westerlies revealing a better agreement with observations than south-easterlies. A sensitivity study of the optimal estimation retrieval shows the advantage of using the Multi-Angular Snowfall Camera to choose the correct particle habit. During the Christmas 2016 storm, the average difference between the double fence gauge observations and the retrieved surface amount for assumed rimed aggregates is less than -5 % for 12 h and 24 h surface snow accumulation. With longer lead time the average difference decreases between double fence gauge observations and forecasted precipitation amount for 12 h and 24 h accumulation (+135 % and +33 %). However, for 24 and 26 December 2016, the surface precipitation amount is predicted too high compared to double fence gauge observations (+60 %). Liquid precipitation was observed at Haukeliseter in the afternoon on 25 December 2016. MEPS initialisations 24 h and 48 h prior successfully simulate the thickness and duration of the liquid layer in the lower most atmosphere, but it predicts less snow water content ( $\leq 1.2 \text{ gm}^{-3}$ ) than the profiles of retrieved snow profiles ( $\leq 1.5 \text{ gm}^{-3}$ ). Local topography effects by the surrounding mountains lead to continuous snow patterns during strong westerlies and weak south-easterlies, show high amount of snow water content with a pulsing pattern. Finally, orography impacts on snow observations and model forecast are discussed.



# TABLE OF CONTENTS

<b>CHAPTER 1: INTRODUCTION</b>	<b>1</b>
<b>CHAPTER 2: DATA AND METHODS</b>	<b>5</b>
2.1 Haukeliseter Site . . . . .	5
2.2 Climate at Haukeliseter . . . . .	7
2.3 Instruments . . . . .	8
2.3.1 Double Fence Snow Gauge . . . . .	8
2.3.2 Micro Rain Radar . . . . .	9
2.3.3 Precipitation Imaging Package . . . . .	12
2.3.4 Multi-Angular Snowfall Camera . . . . .	12
2.4 Optimal Estimation Retrieval Algorithm . . . . .	13
2.4.1 Snowfall Retrieval Scheme . . . . .	14
2.4.2 Environmental Masks for the Optimal Estimation Retrieval . . . . .	17
2.5 Operational Weather Forecast Model . . . . .	18
2.5.1 Ensemble Prediction System . . . . .	18
2.5.2 MetCoOP Ensemble Prediction System . . . . .	19
2.5.3 Meso-NH and the ICE3 Scheme . . . . .	20
2.5.4 AROME-MetCoOp Adjustment . . . . .	23
2.6 Computing Snow Quantities . . . . .	24
2.6.1 MEPS . . . . .	24
2.6.2 Snow Water Content . . . . .	25
2.6.3 Snow Water Path . . . . .	25
2.7 Statistics . . . . .	26
2.8 Extreme Weather . . . . .	27
2.9 Integrated Vapour Transport . . . . .	28
2.10 North Atlantic Oscillation . . . . .	28
<b>CHAPTER 3: ANALYSIS OF THE CHRISTMAS STORM 2016</b>	<b>29</b>
3.1 Dynamic Tropopause . . . . .	29
3.2 Surface, Thickness, Wind . . . . .	30
3.3 Integrated Vapour Transport . . . . .	32
3.4 Observations . . . . .	32
3.5 Large Scale Circulation . . . . .	34
<b>CHAPTER 4: SNOW OBSERVATIONS AND MEPS COMPARISON</b>	<b>43</b>
4.1 The Christmas Storm 2016 - Meteorology . . . . .	43
4.2 Snow . . . . .	59

4.2.1	Sensitivity of the Optimal Estimation Retrieval . . . . .	60
4.2.2	Surface Observations . . . . .	62
4.2.3	Surface Observation and MEPS . . . . .	64
4.2.4	Snow Water Content . . . . .	73
4.2.5	Discussion . . . . .	88
<b>CHAPTER 5:</b>	<b>SUMMARY AND OUTLOOK</b>	<b>95</b>
5.1	Outlook . . . . .	97
<b>LIST OF ABBREVIATIONS</b>		<b>99</b>
<b>REFERENCES</b>		<b>101</b>
<b>APPENDIX A:</b>	<b>FORWARD MODEL</b>	<b>108</b>
A.1	Scattering Model . . . . .	108
<b>APPENDIX B:</b>	<b>MEPS SNOW WATER CONTENT</b>	<b>110</b>
B.1	Ensemble Mean: Deterministic and First Perturbed Member . . . . .	110
B.2	All Ensemble Member . . . . .	113

# CHAPTER 1: INTRODUCTION

Global warming is predicted to cause an increased frequency of extreme weather events such as heat waves, droughts, heavy rains or extremely high winds [Hansen et al., 2014]. Weather and climate extremes can have serious effects on human society and infrastructure, as well as on ecosystems and wildlife. Precipitation observations are important for hydrological, climate and weather research, as more than one-sixth of the world's population receives water from glaciers and seasonal snow packs [Barnett et al., 2005]. Severe weather events are mostly in the focus of media reports with respect to global warming [Meehl et al., 2000]. Understanding and predicting the impact of extreme weather events is one of the grand challenges of current climate research [Field et al., 2014, Stocker et al., 2013].

This work focuses on the extreme weather event during Christmas 2016, comparing snow measurements and ensemble model forecasts at the measurement site Haukeliseter (991 m above sea level) in Southern Norway. The Christmas storm 2016, named 'Urd' by the Norwegian Meteorological Institute (Met-Norway), had a large impact on Eastern, Southern, and Western Norway. The financial costs associated with this storm are estimated to about 180 million Norwegian kroner. 'Urd' led to major traffic problems for cars, trains, ferries and air planes. Most mountain crossings were kept closed during Christmas 2016 [Olsen and Granerød, 2017]. An increase in temperature and therefore a change of frozen to liquid precipitation followed an increase in avalanche danger. In addition, 40 emergency power stations failed, affecting around 70.000 households (Figure 1.0.1). Since human beings are affected by extreme weather it is important to accurately measure and forecast severe storms. The use of accurate observations will lead to better performing weather forecast models, which rely heavily on observations [Joos and Wernli, 2012].

It has long been known that measuring precipitation, especially in the form of snow, is challenging. Winter precipitation measurement shows biases of more than 100 % between different gauge observation networks and different regions leading to different habit and size of frozen aggregates [Kochendorfer et al., 2017]. An adjustment transfer function for single fence gauges represents a capture efficiency as a function of air temperature and wind speed to delimit the error of measured snowfall. Uncertainties in precipitation measurements under windy conditions can affect water balances calculation and the calibration of remote sensing algorithms [Wolff et al., 2015].

Estimates of snowfall from radar reflectivities are non-unique. This means that a given reflectivity can yield different estimates of snowfall depending upon the precise microphysical assumptions used in the retrieval scheme. Kulie and Bennartz [2009], for example, used the CloudSat Cloud Profiling Radar (CPR) to estimate global snowfall from one year of available reflectivity data. They

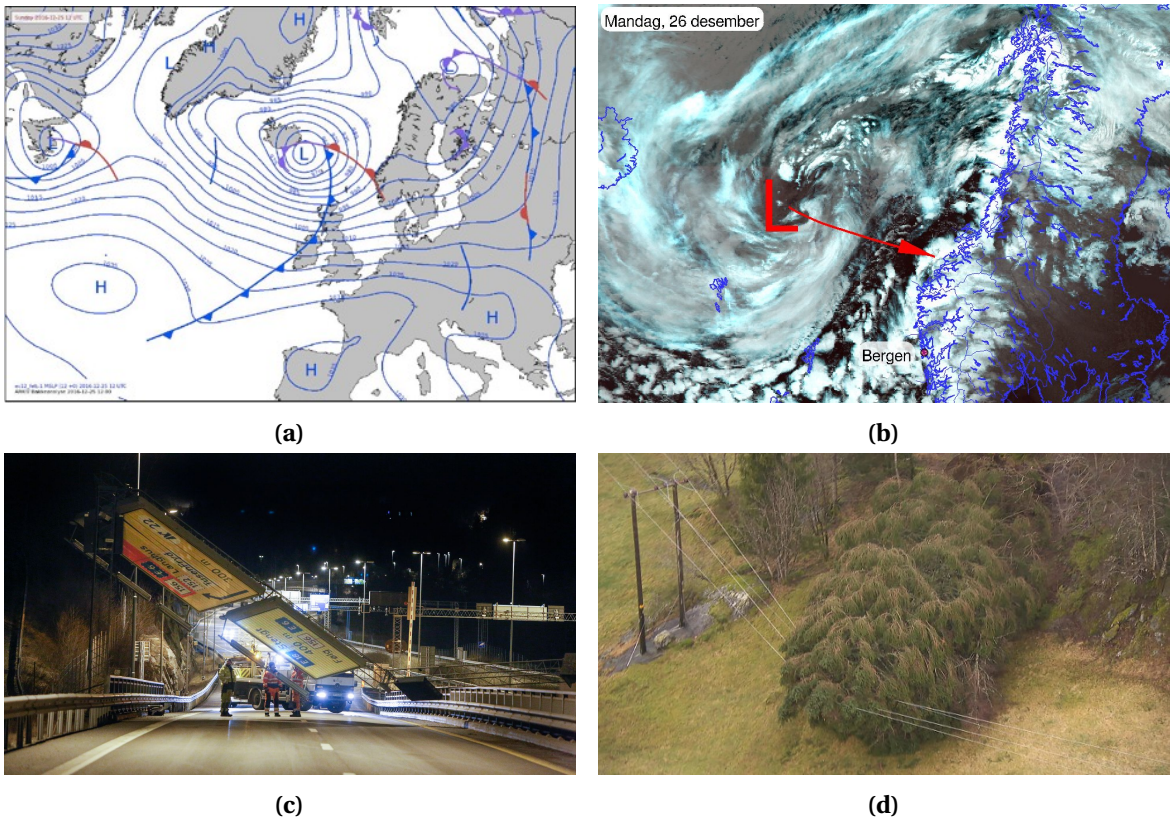


**Figure 1.0.1:** Weather situation during the extreme Christmas storm and impact on the infrastructure. a: Weather situation Sunday 25 December 2016 at 12 UTC from [Olsen and Granerød, 2017]. b: Tweet from Meteorologene [2016] on 26 December 2016 at 9:34 am. c and d: Consequences related to the high wind speeds during Christmas 2016 [Farestveit, 2016, Ruud et al., 2016].

found that snowfall estimates critically depend on assumed snowfall particle size distribution, shape and fall speed. They concluded that the use of traditional Z-S relationships, in which snow (S) is derived only from knowledge of radar reflectivity (Z), can lead to large retrieval uncertainties for a given snowstorm. Subsequent studies have tried to incorporate scene dependent microphysical information into the retrieval scheme. Wood [2011] incorporated a particle size distribution-temperature relationship into the CloudSat operational snowfall retrieval to help reduce retrieval non-uniqueness. In turn, Cooper et al. [2017] used in-situ estimates of snowflake particle size distribution and habit from ground-based instrumentation to explore surface snowfall retrieval performance at Barrow, Alaska. They found reasonable agreement within 20 % of nearby snow gauge measurements. Given the limited snowfall observations at Barrow, Alaska, the authors could not give any definitive conclusion about retrieval performance.

With the increasing expansion of computational power, developments of high-resolution numerical weather forecasting models with  $\leq 4$  km scales can be able to represent small-scale phenomena, such as convective dynamics [Gowan et al., 2018]. Information on magnitudes and location of maximum precipitation amount and wind speed is of significant importance when warnings are published by meteorological services for severe weather events and for further use, e.g. the Norwegian Water Resources and Energy Directorate's hydrological model for flooding and avalanche risk. The ability to use high-resolution models is also followed by various challenges, such as

physical parametrisation schemes, accurate representation of topography such as in Norway, and data assimilation of high-resolution data [Sun, 2005]. Uncertainties on a convective scale can lead to a rapid error growth [Lorenz, 1969]. Hence high-resolution ensemble prediction makes it possible to limit the forecast uncertainty by performing several model runs, each with different initial conditions.

The Meteorological Cooperation on Operational Numerical Weather Prediction (MetCoOp) Ensemble Prediction forecast (MEPS) has been operational at Met-Norway since November 2016. The ensemble prediction system uses the previous deterministic AROME-MetCoOp, a version of the Météo-France Applications of Research to Operations at MEscale (AROME). In addition to the deterministic forecast, nine perturbed ensemble members are initialised in MEPS.

The Christmas storm in 2016 was an excellent test case for analysing unique available precipitation observations at Haukeliseter, Norway, together with the newly available ensemble system MEPS. Haukeliseter has been a World Meteorological Organization (WMO) measuring station with single and double fence precipitation instruments since 2010. During winter 2016/17, the Haukeliseter site also housed a Micro Rain Radar (MRR), Multi-Angle Snow Camera [MASC; Garrett et al., 2012], and Precipitation Imaging Package (PIP) as part of US National Science Foundation (NSF) funded field campaign. The combination of radar and in-situ microphysical observations provides a unique opportunity mean to estimate precipitation profiles, snowfall and snow water content [Cooper et al., 2017]. Such profiles, in turn, could be used to evaluate snow water in the weather prediction forecasts for storms such as Urd. Joos and Wernli [2012] stressed the need for improved observational constraints of precipitation profiles for forecast models. They showed that the storm development in a regional forecast model depends upon whether or not the location of the precipitation is correctly simulated. The precise profile of precipitation determines the latent heat profile, which can lead to either potential vorticity generation or destruction.

This thesis is investigating if the Norwegian ensemble prediction system is able to forecast the variation of an extreme winter event such as 'Urd' and if MEPS is able to predict large scale weather systems as well as frozen precipitation. Furthermore, the use of an ensemble prediction system will give the opportunity to compare the variation of snowfall precipitation at the surface and in the vertical at Haukeliseter.

Observations will help to validate MEPS. The following research questions will be addressed: Does the regional mesoscale model cover local effects associated with the topography surrounding the measurement site? How well does the model predict surface snowfall at the Haukeliseter measurement site during the Christmas storm 2016? Are large scale synoptic weather systems resolved by MEPS? Is there a difference between estimated surface snow accumulation for different optimal estimation assumptions and locations?

The thesis is structured as following: Chapter 2 gives an overview of the data and method. Results will be presented and discussed in Chapter 3, by analysing the Christmas storm 2016, and Chapter 4 will compare snow observations with MEPS forecasts. Chapter 5 summarises the thesis results and gives an outlook into future work.



# CHAPTER 2: DATA AND METHODS

This chapter describes the data and method used in this study. The purpose of this study is to compare the meteorological observations from the Haukeliseter site and the output from the Norwegian operational forecast model for the extreme weather event during Christmas 2016. A strong focus lies on snow profiles following the measurement site, instruments, the optimal estimation retrieval and the regional forecast model used to determine the vertical profile of snow water content for observed snow events. The last section will give an insight on how the data was analysed to compare the different systems.

## 2.1 HAUKELISETER SITE

Haukeliseter, shown in Figure 2.1.1 is a mountain plateau 991 m above sea level, located in the Norwegian county 'Telemark' ( $59.81^{\circ}$  N,  $7.21^{\circ}$  E, Figure 2.1.1). The meteorological station measures precipitation, temperature, snow depth and wind and is operated by the Norwegian Meteorological Institute. It has served as a measurement site for snow accumulation since the winter of 2010/2011 [Wolff et al., 2010] and serves as a WMO station.

The study site is surrounded by mountain tops being 100 m to 500 m higher than the flat area. As seen in Figure 2.1.1b Haukeliseter is more open to the south and the south-west and the closest

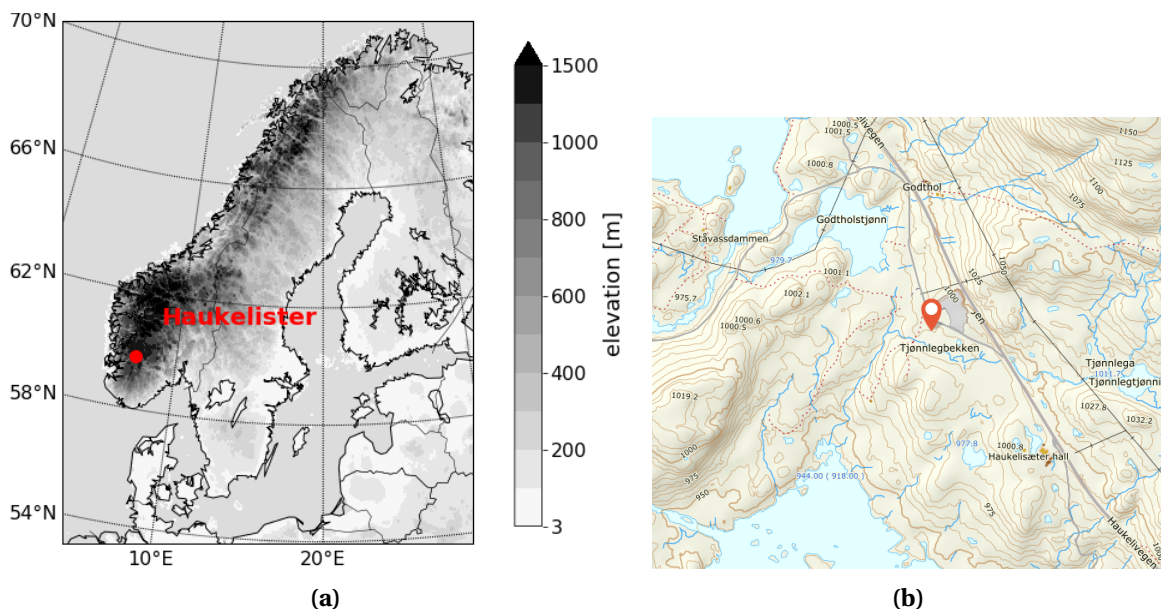


**Figure 2.1.1:** a: Elevation map of Northern Europe, data taken from NOAA [2017]. b: Topographic map of the measurement site Haukeliseter [Kartverket, 2018].

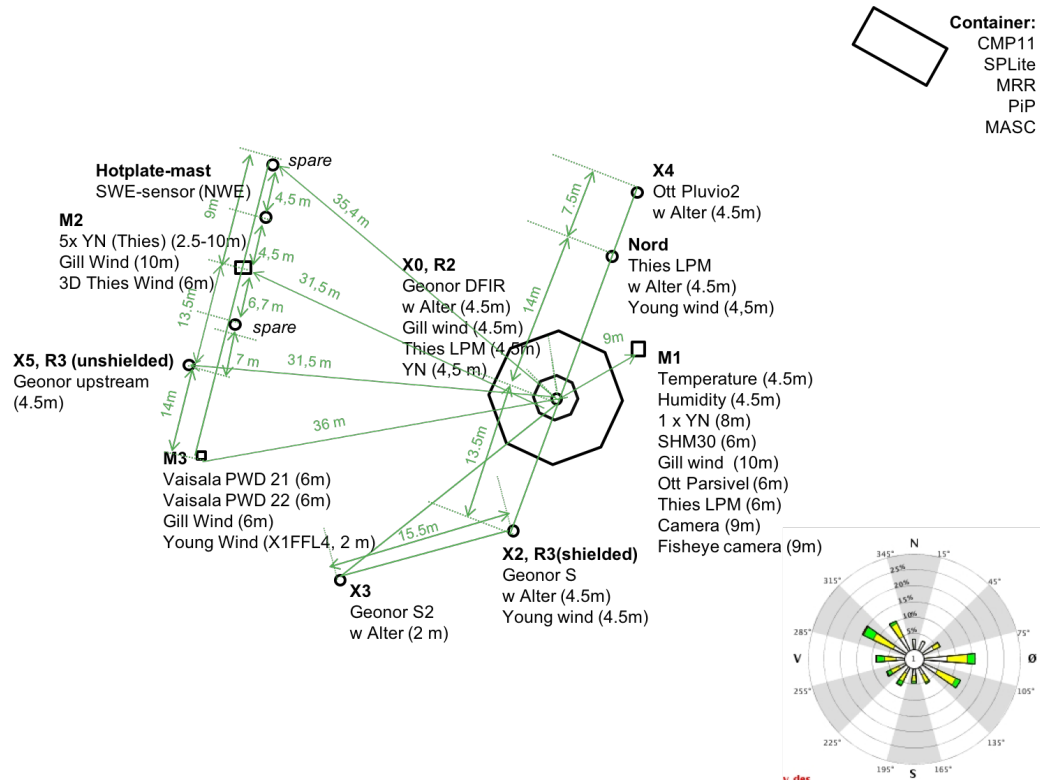


**Figure 2.1.2:** Instrument setting at the Haukeliseter measurement site during winter 2016/2017. **X0**, Double fence gauge (double octagon), **M1**, weather mast with pressure, temperature and 10 m wind sensor. **Container**, with Micro Rain Radar, Particle Imaging Package, and Multi-Angular Snowfall Camera. The windrose indicates the mean wind direction from either from west-north-west or east-south-east averaged from three winters [adapted from Wolff et al., 2015].

mountain top (situated to the NE) has an altitude of 1162 m above sea level. The mountains to the west and north exceed elevations of 1600 m above sea level.

A detailed setting of the measurement site is shown in Figure 2.1.2. The precipitation sensors are perpendicular to the predominant wind. Additional measurements of other meteorological parameters such as temperature, wind, and pressure are used to connect the large-scale weather situation with the local measurements. The data is provided by weather- and climate data-server from Met-Norway [eklima, 2016], where the temperature is measured at double fence height. The hourly value of temperature is represented by the last minute value of the previous hour measurement. The 10 m wind is measured by an ultrasonic wind sensor from Gill, mounted at the tower close to the double fence. Wind data is obtained from eklima [2016] and represents 10 min averages from the last 10 min of an hour.

## 2.2 CLIMATE AT HAUKELISETER

The general climate at Haukeliseter can be defined with the updated Köppen-Geiger climate types presented in Peel et al. [2007]. Figure 8 in Peel et al. [2007] show, that Haukeliseter may lay in a transition zone and can be categorized as ET, a polar tundra climate type (hottest month temperature  $T_{hot} \geq 0^{\circ}\text{C}$ ) or as Dfc, a cold climate without dry season and cold summers.

Haukeliseter presents a typical Norwegian climate condition. At the measurement site, frequent snow events combined with high wind speeds are observed during a six to seven month winter period. In addition, a snow amount of about two to three meter can be expected, where 50 % of the yearly precipitation is frozen [Wolff et al., 2015].

The mean wind direction (Figure 2.1.2) for solid precipitation is from the west/east with maximum wind speed above  $15 \text{ m s}^{-1}$ , observed during a 10-year winter period at a nearby station [Wolff et al., 2015].

Figure 2.2.1 shows the observations at the Haukeliseter site during December 2016. In Figure 2.2.1, the green dashed line ( $-6^{\circ}\text{C}$ ) represents the 30-year climate temperature in December [1961 to 1990, eklima, 2016]. December 2016 was warmer with an anomaly of  $+4.9 \text{ K}$  above the climate mean. In December 2016, the precipitation was 200 % higher than the climate mean. This difference could be associated with the new installation of the double fence - Geonor gauge at Haukeliseter. Wolff et al. [2015, Figure 5] shows that single fence precipitation gauges underestimate the amount of precipitation with approximately 80 % during high wind speed events. The double fence gauge was not installed before 2010/2011, this might have led to an observation of too little precipitation at Haukeliseter during winter and leading to incorrect climate statistic. The precipitation observed in the period of 21 to 26 December 2016 were 30 % of the total accumulated precipitation in December 2016. Furthermore, a maximum 10 m wind speed of  $19 \text{ m s}^{-1}$  was observed in this period, which is considered as a gale.

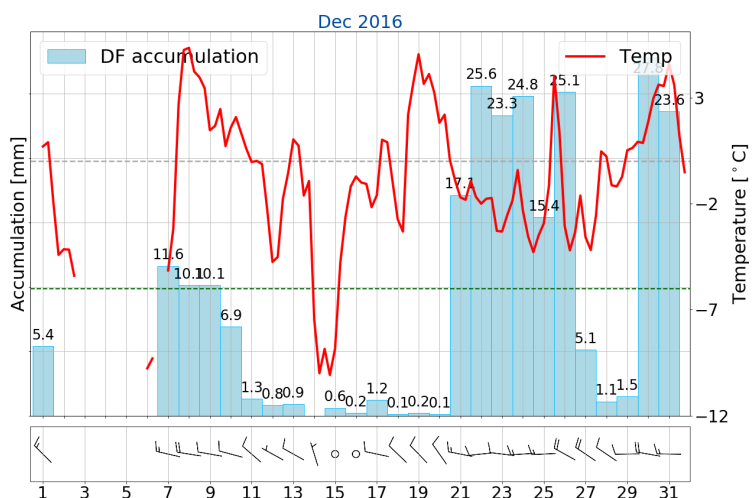


**Figure 2.2.1:** Observations at Haukeliseter weather mast during December 2016. The daily accumulation is presented in light blue [mm]; the six hour mean temperature in red, [ $^{\circ}\text{C}$ ], and daily maximum 10 m wind as barbs [ $\text{m s}^{-1}$ ]. The freezing temperature is indicated by the grey dashed line and the monthly normal value ( $-6.0^{\circ}\text{C}$ ) by the green [eklima, 2016]. Note, no data was available from 2 to 6 December 2016.

## 2.3 INSTRUMENTS

The WMO site Haukeliseter, operated by Met-Norway serve numerous meteorological measurements of temperature, wind speed and direction. 10 m wind and 4.5 m air temperature are measured at the tower **M1** close to the double fence (Figure 2.1.2). The wind measurements are performed with an ultrasonic wind sensor from Gill (Wind observer II with extended heating). Air temperature is obtained with a pt100 element at gauge height and protected by standard Norwegian radiation screen [Wolff et al., 2015]. Further information about the WMO site and the instrument setting, can be found in Wolff et al. [2013, 2015].

A collaboration between the University of Utah, the University of Wisconsin, and Met-Norway made it possible to install three additional instruments at the measurement site during winter 2016/2017. A Micro Rain Radar (MRR) is used to obtain particle reflectivity and Doppler velocity aloft, thus providing the vertical structure of the storm. Additionally, a Multi-Angle Snowflake Camera (MASC) and a Precipitation Imaging Package (PIP) will be used to determine the snow habit, the snowfall particle size distribution, and the near-surface fall speed. Since many factors such as humidity and temperature contribute to snowflake geometry, the use of these instruments will provide knowledge of snowflake habits, particle size distributions, and fall speed crucial to reduce error in snowfall retrievals.

A sketch of the instrumentation setting is presented in Figure 2.1.2. The octagonal (**X0**) indicates the double fence gauge. The **container** is north-east from the double fence having the MRR, MASC and PIP mounted at the top. **M1** in Figure 2.1.2 is the 10 m weather mast, providing the hourly eklima [2016] temperature, pressure, and wind measurements. The mean wind direction is from west-north west and east-south east as shown in the wind rose in Figure 2.1.2.

### 2.3.1 DOUBLE FENCE SNOW GAUGE

Since the winter 2010/2011, Haukeliseter is equipped with several precipitation gauges (**X0, X2, X3, X4, X5, Nord** in Figure 2.1.2). The wind shielded gauges are placed perpendicular to the main wind direction (easterly/westerly wind, Figure 2.1.2).

The double fence gauge (**X0** in Figure 2.1.2) is presented in Figure 2.3.1a to the left of the image. Inside the double fence is a precipitation-weighing gauge Geonor T-200B3 [3-wire transducers, 1000 mm, Geonor Inc., 2015] (Figure 2.3.1b) with an Alter wind screen to reduce wind turbulence around the gauge. At Haukeliseter the orifice height of the Geonor T-200B3 is 4.5 m above the ground because of expected snow height of two to three meter during a winter season and the likelihood of measuring drifting snow [Wolff et al., 2013, 2015].

A vertical cross section of the T-200B gauge is shown in Figure 2.3.1b. The precipitation particles fall through the 200 cm<sup>2</sup> orifice (pink) protected with a heated collar into a cylinderic bucket filled with frost protection (cyan). The bucket is placed on top of a bucket support dish (yellow) [Figure 2.3.1b, Geonor Inc., 2015]. This dish is connected with three wire sensors (green) having an eigenfrequency changing with the weight inside the bucket.

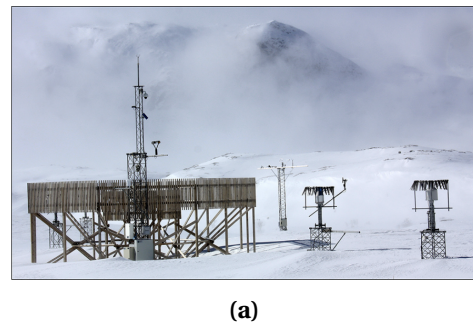
The three sensors provide a reduction of an error in connection with an unlevel installation. Met-Norway averages the values of all three sensors and provide hourly accumulated data at eklima.

In this thesis, the hourly precipitation amount provided by eklima is accumulated over 48 h.

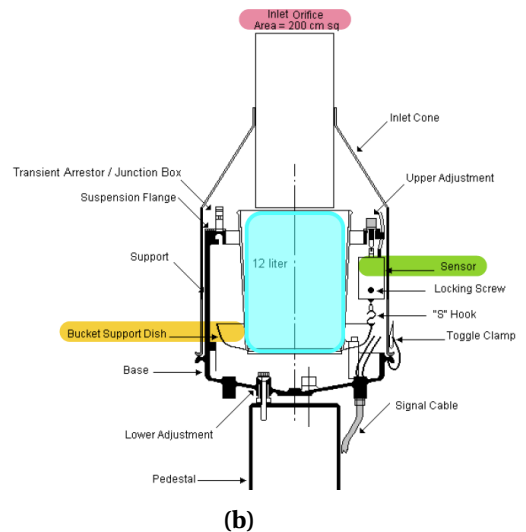
Measurement uncertainties can be caused by the instrument itself, which varies with wind speed, gauge wind shielding, and shape, size, phase, and fall velocity of hydrometeors [Kochendorfer et al., 2017, Wolff et al., 2015]. Wind plays different roles in the amount of accumulation depending on the kind of precipitation. For temperatures below  $-2^{\circ}\text{C}$  the wind influences the falling snow. Less precipitation can be observed at higher wind speeds or more precipitation can be measured if too much is blown into the gauge. Since wind has an influence on frozen precipitation, a WMO precipitation analysis between 1987 and 1993 recommended that the *double-fence intercomparison reference* should be used for snow measurements [Goodison et al., 1998]. An adjustment for unshielded and single-shielded precipitation gauges followed in 2010 [Nitu and Wong, 2010].

Wolff et al. [2015] showed the catch ratio between the standard Geonor precipitation gauge and the Double Fence - Geonor T-200B3 (Figure 2.3.1). Only 80 % of solid precipitation is observed at wind speeds of  $2\text{ m s}^{-1}$  whereas only 40 % at  $5\text{ m s}^{-1}$  [Wolff et al., 2015, Figure 5].

The precipitation gauge protected by an octagonal double fence (**X0**, Figure 2.1.2) is more accurate than the single fence (**X2**, Figure 2.1.2) and are used as the reference to all surface accumulation measurements in this thesis. The double fence creates an artificial calm wind and therefore maximize the catch of precipitation, [Wolff et al., 2015]. The wind inside the double fence is measured to be below  $5\text{ m s}^{-1}$  even if the winds outside exceed  $20\text{ m s}^{-1}$ . Alternatively, a bush gauge is a precipitation gauge surrounded by a large bush to create artificial calm winds to increase the catch ratio of frozen precipitation and is considered as the best available measurement for solid precipitation [Wolff, unpublished]. Unfortunately, there are only two bush gauges in the world available, and because of local limitations a double fence construction was developed [Goodison et al., 1998]. Wolff [unpublished] comparison between bush gauge and double fence precipitation measurements have shown that the double fence has a negative bias of 10 % for wind speeds up to



(a)



(b)

**Figure 2.3.1:** (a) From left to right: Double fence gauge (**X0**) and unprotected precipitation gauges (**Nord, X4**) at Haukeliseter, from Wolff et al. [2015]. The prevailing easterly (westerly) wind from the lower, left corner in a (the opposite site). In front of the double fence gauge is the 10 m weather mast (**M1**). (b) Vertical cross section of Geonor T-200B3 precipitation gauge. pink: orifice; cyan: cylindric bucket with frost protection; yellow: bucket support dish; green: wire sensor [adapted from Geonor Inc., 2015].

$9 \text{ m s}^{-1}$ . As for now, no detailed comparison between bush gauge and double fence exists at thigh wind speeds. Therefore, comparisons from bush and double fence gauge were extrapolated for higher wind speed. These results revealed that the double fence has a negative bias up to 20% during high wind speed and frozen precipitation.

### 2.3.2 MICRO RAIN RADAR

Radar are very useful to observe the vertical profile of hydro meteors in the atmosphere. The instrument detects mesoscale features and makes it possible to visualise the vertical structure of storms [Markowski and Richardson, 2011].

The Micro Rain Radar (MRR, Figure 2.3.2) measures profiles of Doppler frequencies [METEK, 2010]. The MRR in Figure 2.3.2 transmits electromagnetic radiation (transmitter) at a frequency of 24 GHz. The principle of radar measurement is based on an electromagnetic wave, which is emitted from the radar transceiver over the parabolic dish into the atmosphere. The electromagnetic wave interacts with the falling hydrometeors along the beam, were a small fraction is scattered back to the antenna (parabolic dish) and radar receiver (Figure 2.3.2). The quantity of scattering depends on the shape and structure of the reflected particle. Due to the falling particles exists a frequency difference between the transmitted and the received signal (Doppler frequency). The Doppler frequency describes the movement of the particle. Particles have different size diameters and therefore different fall velocity, hence the backscatter signal consists of a distribution of different Doppler frequencies. From the Doppler frequencies a power spectrum can be calculated and from this a reflectivity spectrum is computed with the use of calibration parameters [METEK, 2010].

The transmitting signal is send out continuously as a linearly decreasing saw tooth signal which makes it possible to achieve profiles of reflectivity. Vertical profiles of reflectivity give information about the diameter of the target object. The MRR has a frequency of 24 GHz and a temporal and spatial resolution of 60 s and 100 m, respectively. The radar height range from 100 m (because of ground clutter) to 3.000 m [METEK, 2010].

MRR radar reflectivity ( $Z$ ) is transformed from  $1 \text{ mm}^6/\text{m}^3$  to radar equivalent reflectivity ( $Ze$ ) dBZ, by the following relationship;

$$Ze = 10 \log_{10} \left( \frac{Z}{1 \text{ mm}^6/\text{m}^3} \right) \quad [\text{dBZ}] \quad (2.3.1)$$

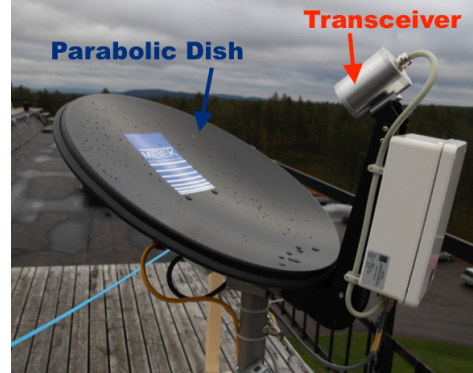


**Figure 2.3.2:** Micro Rain Radar at the measurement site in Kiruna. Transceiver transmits Radar signal using the antenna (parabolic dish) and receives backscatter signal over the antenna. During winter 2016/2017 installed at Haukeliseter (**container**).

**Table 2.3.1:** Typical reflectivity values for different precipitation types, obtained from measurements, models, and observations. The rainfall rate  $R$  is calculated with Equation (2.3.2) [Doviak and Zrnic, 1993].

	<b>Ze</b> [dBZ]	<b>R</b> [mm h <sup>-1</sup> ]
<b>Drizzle</b>	<25	1.3
<b>Rain</b>	25 to 60	1.3 to 205.0
<b>Snow</b>		
dry, low density	<35	5.6
Crystal; dry, high density	<25	1.3
wet, melting	<45	23.7
<b>Graupel</b>		
dry	40 to 50	11.5 to 48.6
wet	40 to 55	11.5 to 99.9
<b>Hail</b>		
small; <2 cm, wet	50 to 60	48.6 to 205.0
large; >2 cm, wet	55 to 70	99.9 to 864.7
<b>Rain &amp; Hail</b>	50 to 70	48.6 to 864.7

A transformation to rainfall rates can be performed by the  $Z$ - $R$  relationship ( $R$ , rain rate [mm h<sup>-1</sup>]). The rainfall rate in each layer can be estimated by the use of typical fall speeds and the Marshall-Palmer particle size distribution for liquid particles [Rinehart, 2010],

$$Z = 200R^{\frac{8}{5}} \quad [\text{mm}^6 \text{m}^{-3}]$$

$$R = \left( \frac{10^{\frac{Ze}{10}}}{200} \right)^{\frac{8}{5}} \quad [\text{mmh}^{-1}]. \quad (2.3.2)$$

The  $Z$ - $R$  relationship (Equation (2.3.2)) and transformation to radar equivalent reflectivity can be used to estimate rain rate for polarimetric measurands obtained from modelling, measurements, and literature [Doviak and Zrnic, 1993] is represented in Table 2.3.1.  $Z$ -snowfall relationships were developed but showed to be difficult to apply due to the variation of size and density of the particles. It was found that using traditional  $Z$ -snowfall relationships did not provide accurate results for all snow events [L'Ecuyer, 2017]. This shows the need to combine ground-based observations together with an optimal estimation retrieval to estimate accurate results for snowfall events.

In this thesis the data was provided in dBZ ( $Ze$ ) and then transformed to  $Z$  [mm<sup>6</sup>m<sup>-3</sup>] with the inverse of Equation (2.3.1). After the transformation the reflectivity is averaged for every 200 m thickness layer, where only values above 300 m altitude were taken into account. Reflectivity at 400 m represents the mean value of reflectivity between 300 m and 500 m.

Afterwards the averaged reflectivity is used as a-priori guess in the optimal estimation retrieval (Section 2.4.1).

In Section 4.2.4 the measured  $Ze$  are used to give a first estimate about the type of precipitation with the help of Table 2.3.1.

### 2.3.3 PRECIPITATION IMAGING PACKAGE

The Precipitation Imaging Package (PIP) is a video disdrometer that is a modification of the Snowflake Video Imager presented by Newman et al. [2009]. It consists of a halogen lamp and a video system that samples at 60 Hz (Figure 2.3.3). Both lamp and lens have a distance of approximately 3 m that follows a field of view: 24 mm by 32 mm.

In front of the halogen lamp is a frosted window, so that the background light is uniform over all time. A falling particle appears as a 2-D shadow in the video image. Particle size distribution (PSD) and fall speed of precipitation can be determined from the black and white images provided by the system. The instrument also can give first order estimates of snowflake particle habit when in focus in the images. Newman et al. [2009] describes the details of the algorithm applied to the system to get information about the snow-particle habit.

The winds have almost no effect on the result of the video distrometer [Newman et al., 2009]. To reduce eventual wind effects, the distrometer was oriented perpendicular to the mean wind.



**Figure 2.3.3:** Precipitation Imaging Package at Haukeliseter mounted at the **container** pointing towards the double fence gauge.

### 2.3.4 MULTI-ANGULAR SNOWFALL CAMERA

The Multi-Angular Snowfall Camera (MASC) takes high-resolution images of hydrometeors in free fall and measures the fall-speed simultaneously.

The MASC consists of three cameras, three flashes, and two near-infrared sensors, pointing at a ring centre (Figure 2.3.4). A hydrometeor has to pass through the ring in a certain way to trigger the near-infrared sensors. At the same time three cameras take a picture of the falling particle. Since the cameras take pictures from three different angles, the particles size, shape, and orientation can be specified from an algorithm applied to the image, described in Garrett et al. [2012]. Furthermore, the form and heritage of the hydrometeor, such as collision-coalescence, riming, capture nucleation, or aggregation, can be

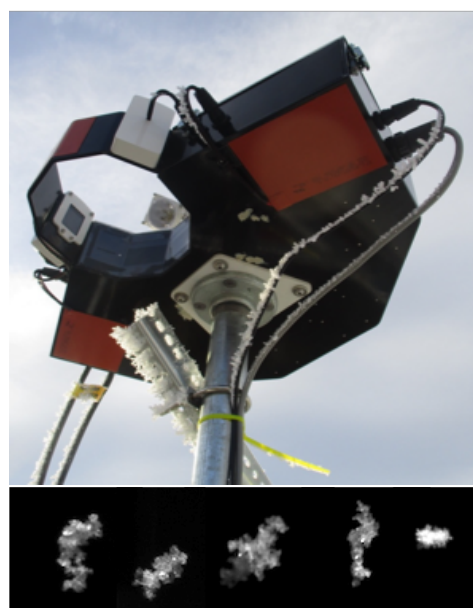


**Figure 2.3.4:** Multi-Angular Snowfall Camera and images taken by the instrument during the Christmas storm 2016. Located on **container**.

estimated. The near-infrared sensors are used to trigger the cameras and the lights. Furthermore the fall-speed of the hydrometeors is measured. The time difference between the upper trigger and the lower trigger is calculated while a particle passes.

Particle images from PIP and MASC were analysed for 21 to 26 December 2016 by the University of Utah. In this thesis this the result of the University of Utah was used to determine habit and rimed particles to apply to the optimal estimation retrieval (Section 2.4) and perform a sensitivity study (4.2.1).

## 2.4 OPTIMAL ESTIMATION RETRIEVAL ALGORITHM

The purpose of this study is to apply an optimal-estimation snowfall retrieval on ground based measurements to estimate the surface accumulation and vertical snow water content for an extreme event during Christmas 2016. These will later be used to compare to 48 h MEPS model forecasts to see if the model was able to predict synoptical features and precipitation related to the extreme event 'Urd' in 2016. The quantitative estimation of snowfall at the global scale from spaceborne measurements has been available only recently. Initial retrieval approaches were based on passive microwave measurements [Noh et al., 2006, Skofronick-Jackson et al., 2004]. But since these passive measurements can only assess total integrated snow water path for a given column, such efforts were unable to provide much information on the profiles of snow water content. The launch of the CloudSat 94 GHz Cloud Profiling Radar (CPR) in 2006, however, provided the first opportunity to examine such vertical structure at a global scale. Several studies have shown, that estimated snow rate depends upon retrieval assumptions such as snowflake habit and particle size distribution (PSD) and can give large differences for a given radar reflectivity.

For the operational CloudSat snowfall retrieval scheme (2C-SNOW-PROFILE), Wood et al. [2015] developed snowflake particle models based upon video snow disdrometer observations from the Canadian CloudSat-CALIPSO Validation Project [C3VP, Hudak et al., 2006]. Scattering properties for these snow particle models were based upon the Discrete Dipole Approximation (DDA) method. In addition, they derived an a priori relationship between particle size distribution and temperature that they could use as an additional constraint for the snowfall scheme. Use of the flexible optimal-estimation retrieval framework allowed to develop a best estimate of snow properties that are consistent with both the CPR reflectivities and the a priori constraint.

They have also been used to estimate snowfall in remote locations such as the Antarctic and Arctic [Kulie et al., 2016, Palerme et al., 2014] that in turn have been used to evaluate the representation of snowfall in climate models [Christensen et al., 2016, Palerme et al., 2017]. These estimates have been used to assess the performance of ground-based radar schemes such as those based upon the operational weather radar system in Sweden [Norin et al., 2015]. Despite such progress, however, the CloudSat scheme can still lead to uncertainties in the retrievals of up to 140 % to 200 % [Wood, 2011] for individual storms.

Again, these uncertainties arise from the large variance in snowflake microphysical properties as observed in nature. In response, Cooper et al. [2017] explored the use of in-situ, event specific observations of snowflake microphysical properties to improve radar-based retrievals of snowfall.

This work was based upon observations from the Ka-band ARM (The Atmospheric Radiation Measurement) Zenith Radar (KAZR) and Multi-Angle Snow Camera (MASC) deployed at the ARM Climate Facility Site at Barrow, Alaska in Spring 2014. This ground-based 35 GHz retrieval scheme was modified from the space-borne 94 GHz CloudSat retrieval scheme developed by Wood [2011]. But instead of using a temperature dependent a priori characterisation of PSD, Cooper et al. introduced the in-situ observations of particle size distribution through the a priori terms of the optimal-estimation framework.

Preliminary analyses suggested good performance for this retrieval scheme at Barrow, Alaska. Estimates of snowfall from the Cooper et al. [2017] approach differed by 18 % relative to nearby National Weather Service snow gauge measurements for total accumulation over multiple snow events. However, given limited snowfall observed at Barrow during the deployment of the MASC, it was difficult to come to any definitive conclusions about retrieval performance. The NSF (National Science Foundation) funded field campaign with MRR, MASC, and PIP (Precipitation Imaging Package) deployment at Haukeliseter provides an ideal opportunity to further explore the Cooper et al. [2017] retrieval approach. This thesis will continue to examine the sensitivity of retrieval surface snowfall rate to assumptions of habit, fall speed, and particle size distribution as in Cooper et al. [2017]. In addition, this study here will examine the vertical profiles of snowfall profiles in the atmospheric column.

#### 2.4.1 SNOWFALL RETRIEVAL SCHEME

The optimal-estimation snowfall retrieval scheme was modified for the Barrow instrumentation described in Cooper et al. [2017] to the 24 GHz MRR, MASC, and PIP located at Haukeliseter. This scheme was then used to derive surface snowfall rates and vertical profiles of snow water content using different combinations of retrieval assumptions based upon in-situ observations. Here a discussion of the optimal-estimation framework is presented so that the reader can understand exactly how the different measurements in the retrieval scheme were incorporated. The differences in the forward and inverse problem are reviewed in the beginning. Both, forward and inverse problem underlie the basic methodologies of remote sensing.

The general concepts of forward and inverse problems are illustrated in Figure 2.4.1. The forward problem describes the relationship between the physical parameters of interest and the measurements (Figure 2.4.1a). In Figure 2.4.1b, the physical parameter is the reindeer and the measurements are its tracks. In the here presented thesis snowfall scheme, the physical parameters are the vertical profiles of snow water content (SWC) and the measurements are the MRR reflectivities. The inverse

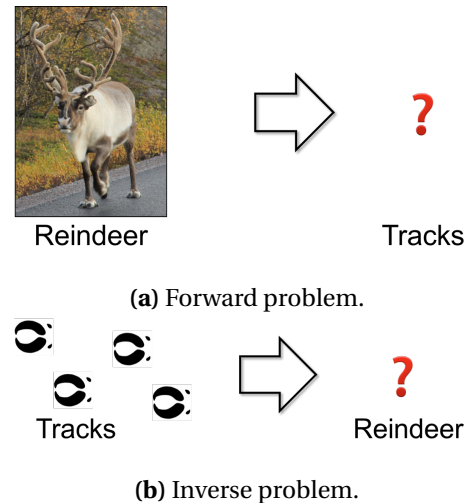


**Figure 2.4.1:** a: Forward problem, relationship between parameter of interest (reindeer) and the unknown parameter of measurements (tracks). b: An inverse problem when the parameter of measurements is known, but the parameter of interest is not [Stephens, 1994].

problem represents the opposite goal. The physical entity (reindeer and SWC) must be inferred from the measurements (reindeer tracks or MRR reflectivities).

The optimal-estimation framework is used to solve the inverse problem for the thesis work. But it is more complex than the direct inversion as represented in Figure 2.4.1b. Instead of inverting directly for the parameter of interest (SWC) from the measurements [dBze], the scheme includes additional information based upon an ‘a priori’ understanding of the physics of the retrieval problem. Thus, it represents a weighted balance between what the data can tell about the state and what is already known about it. For the CloudSat retrieval scheme, this a priori information came from a parametrisation relating particle size distribution (PSD) to temperature. For the Barrow and Haukeliseter schemes, the a priori information could also come from the in-situ observations of snowflake microphysics. These constraints also add numerical stability to the inversion process when there are either calibration errors in the measurements or uncertainties in the forward model that relates the physical parameter to measurement space. Details of the radar forward model are discussed at the end of this section.

The optimal estimation method is based on Gaussian statistics. It solves for snowfall properties of interest or retrieval vector,  $\mathbf{x}$ , by minimizing the scalar cost function,  $\Phi$ , as in Equation (2.4.1).

$$\begin{aligned}\Phi(\mathbf{x}, \mathbf{y}, \mathbf{a}) = & (\mathbf{y} - F(\mathbf{x}))^T \mathbf{S}_y^{-1} (\mathbf{y} - F(\mathbf{x})) \\ & + (\mathbf{x} - \mathbf{a})^T \mathbf{S}_a^{-1} (\mathbf{x} - \mathbf{a})\end{aligned}\quad (2.4.1)$$

Specifically, or this thesis retrieval scheme,  $\mathbf{x}$  represents the PSD parameters of slope and number intercept of an assumed exponential size distribution for each radar range bin as in Equation (2.4.2).  $\mathbf{y}$  is the vector of MRR reflectivities. The vector  $\mathbf{a}$  is the a priori guess for slope parameter and number in each range bin.  $F(\mathbf{x})$  represents the forward model that translates snow properties into reflectivity space. Minimizing the cost function therefore seeks to reduce the difference between the observations,  $\mathbf{y}$ , and simulated observations,  $F(\mathbf{x})$  and between the a priori guess ( $\mathbf{a}$ ) and the retrieval vector ( $\mathbf{x}$ ).

$$n(r) = N_0 \exp(-\lambda r) \quad [\text{m}^{-3} \text{ mm}^{-1}] \quad (2.4.2)$$

The  $\mathbf{S}_y$  and  $\mathbf{S}_a$  terms, in Equation (2.4.1), represent the forward model and measurement error covariance matrix and the a priori error covariance matrix, respectively. The relative differences between  $\mathbf{S}_a$  and  $\mathbf{S}_y$  weight the importance of the observations and the a priori considerations in determining our best estimate of PSD properties.

Newtonian iteration is used until the value of the cost function converges and our best estimate of snowfall properties are found. The optimal-estimation scheme also provides error diagnostics through the retrieval error covariance matrix,  $\mathbf{S}_x$ , as in Equation (2.4.3).

$$\mathbf{S}_x = \left( \mathbf{S}_a^{-1} + \mathbf{K}^T \mathbf{S}_y^{-1} \mathbf{K} \right)^{-1} \quad (2.4.3)$$

The Jacobian matrix,  $\mathbf{K}$ , represents the sensitivity matrix of the perturbed result of the forward model. The true state  $\mathbf{x}$  is perturbed by 0.2 % and thus  $\mathbf{K}$  represents the relation between simulated

values to the true state and how sensitive the simulated values are to small changes when starting a new retrieval cycle. The closer  $\mathbf{K}$  is diagonal, the more is  $\mathbf{x}$  determined by the real observed and a priori values. If the limit of the partial derivative is close to unity, the retrieved value  $\mathbf{x}$  is its true state [Wood, 2011].

In practical application for this multiple layer retrieval scheme, log-transformed particle size distribution parameters of slope and number intercept were used due to the large expected range of these variables. The state vector,  $\mathbf{x}$ , is defined in Equation (2.4.4).

$$\mathbf{x} = \begin{bmatrix} \log(\lambda)_0 \\ \vdots \\ \log(\lambda)_{\text{nlayer}} \\ \log(N_0)_0 \\ \vdots \\ \log(N_0)_{\text{nlayer}} \end{bmatrix} \quad \text{nlayer} = 14 \quad (2.4.4)$$

The usage of a priori terms were explored both from in-situ microphysical observations and from the PSD-temperature relationship developed for the CloudSat scheme as in Equations (2.4.5) and (2.4.6). Temperatures in °C at Haukeliseter were taken from site measurements with an assumption of a moist adiabatic lapse rate for the observed snow events. The log transformed slope and number intercept values were taken from Wood [2011].

$$\log(\lambda) = -0.03053 \cdot T_{ap} - 0.08258 \quad [\log(\text{mm}^{-1})] \quad (2.4.5)$$

$$\log(N_0) = -0.07193 \cdot T_{ap} + 2.665 \quad [\log(\text{m}^{-3} \text{mm}^{-1})] \quad (2.4.6)$$

The log-transformed equations are useful, since the results from C3VP were similar to other observations. The study showed, that  $N_0$  ranges over several order of magnitude as well as  $\lambda$  was non-Gaussian for the snow events Wood [2011]. The diagonal matrix elements in  $\mathbf{S}_a$  (Equations (2.4.1) and (2.4.3)) are equal to 0.133 and 0.95 for the particle slope parameter and the number intercept, respectively, as from Eq. 7.35 and 7.36 in Wood [2011]. The diagonal matrix elements for  $\mathbf{S}_y$  are 2.5<sup>2</sup> in Equations (2.4.1) and (2.4.3).

After the best estimate of PSD parameters are found, the snow water content in each layer is calculated using the snow particle mass-dimension relationships as in Appendix A.1.

$$\text{SWC} = \int_{r_{min}}^{r_{max}} m(r)n(r)dr \quad [\text{g m}^{-3}] \quad (2.4.7)$$

$r$  is the particle maximum dimension and  $m(r)$  the related mass.

This thesis work considered the database of particle models developed for the CloudSat mission, e.g. different types of aggregates, sector plates, and columns. Scattering properties for these snowflakes were calculated for the 24 GHz frequency using discrete dipole approximation (DDA). Observations from the MASC of snowflake habit were used to guide particle selection. Snow water content, in turn, was translated into a snowfall rate using fall speed observations (MASC, PIP, or MRR Doppler

velocity) or climatological analyses ( $V = 0.85 \text{ m s}^{-1}$ ). Surface snowfall rate is estimated using the SWC from the lowest non-noise reflectivity and radar bin.

The forward model that calculates simulated 24 GHz MRR reflectivities from PSD parameters was modified from that used in the CloudSat 94 GHz operational snowfall product (2C-SNOWPROFILE). Backscatter from frozen hydrometeors in each radar bin is summed up as in Equation (2.4.8) form which reflectivity factor,  $Z$ , can be found (Equation (2.4.9)).

$$\eta_{bk} = \int_{r_{min}}^{r_{max}} n(r) \sigma_{bk} dr \quad [\text{m}^{-1}] \quad (2.4.8)$$

$$Ze^{ss,na} = \frac{\Lambda^4}{\|K_w\|^2 \pi^5} \eta_{bk} \quad [\text{mm}^6 \text{m}^{-3}] \quad (2.4.9)$$

Where,  $\Lambda$  is the wavelength of the radar;  $\|K_w\|^2$  is the complex refractive index of water. Radar backscatter values were estimated using discrete dipole approximation for the CloudSat particle models at 24 GHz. Unlike the 94 GHz spaceborne CloudSat mission, multiple scattering and attenuation can be neglected for 24 GHz MRR and the short path length retrievals as viewed from the ground perspective.

#### 2.4.2 ENVIRONMENTAL MASKS FOR THE OPTIMAL ESTIMATION RETRIEVAL

Different steps and assumptions are done in the here presented snowfall retrieval, to achieve vertical profiles of snowfall from MRR. The snowfall rate at the surface can be estimated from one of the lower levels. The optimal estimation retrieval is only performed for profiles, which are likely to have observed snow.

This value was chosen as sensitivity studies [e.g. Wood et al., 2013] that a days worth of such re-

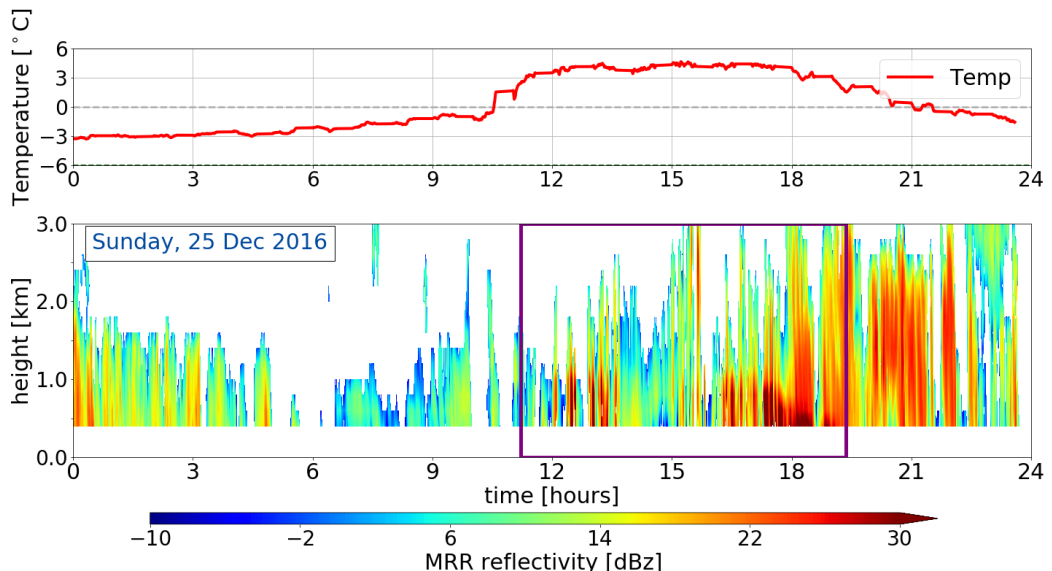


**Figure 2.4.2:** A priori temperature dependence within the optimal estimation retrieval for an all day precipitation event on 25 December 2016. The upper panel shows the surface a priori guess,  $T_{ap}$ , measured at the Haukeliseter site. The lower panel presents the reflectivity measure by the MRR. Additionally, the purple frame indicates the time, where the MRR reflectivity was larger than  $-10 \text{ dBZ}$  and surface temperatures less than  $2^\circ\text{C}$ .

flectivities would produce only a trace of snow. Such a value therefore guarantees that a significant snow event is not missed and that any storms with lower dBZ values would not produce meaningful precipitation. The Haukeliseter measurement site is equipped with a weather mast, measuring the air temperature every minute at two-meter height (compare Figure 2.4.2, upper panel). Since the MRR measures above 300 m and temperature measurements exists only at the surface, a priori temperature ( $T_{ap}$ ) at the surface is assumed to be similar to the observed near-surface air temperature. The use of a moist adiabatic lapse rate of  $dT/dz = 5 \text{ K km}^{-1}$  gives  $T_{ap}$  in each layer. Snow existence at temperature measurements up to a threshold of +2 °C are assumed. Liu G. [2008] validated this threshold, by analysing present weather reports to find the distinction between liquid and solid precipitation.

The purple line in the lower panel of Figure 2.4.2 represents the time frame during 25 December 2016, where the MRR reflectivity is less than –15 dBZ, and a priori temperature passes the 2 °C limit at the surface.

## 2.5 OPERATIONAL WEATHER FORECAST MODEL

MetCoOp Ensemble Prediction System (MEPS) became operational at Met-Norway in November 2016 when the extreme Christmas storm occurred over Norway. Comparing model data with actual observations helps to validate model predictions.

MEPS is used as weather forecast at the Norwegian Meteorological Institute, the Swedish Meteorological and Hydrological Institute (SMHI) and the Finnish Meteorological Institute (FMI), [Køltzow, 2017, Müller et al., 2017]. It replaced Météo-France Applications of Research to Operations at MEsoscale (AROME)-MetCoOp, which was operational from March 2014 until November 2016. Both models are a branch of the Hirlam Aladin Regional Meso-scale Operational NWP In Europe (HARMONIE) AROME model, version 40h1.1. MEPS and AROME-MetCoOp therefore built on the bases of AROME-France a convective-scale model. The physical parametrisations are from the French mesoscale non-hydrostatic atmosphere model (Meso-NH). The model got operational in 2008 and has a horizontal resolution of 2.5 km [Seity et al., 2010].

### 2.5.1 ENSEMBLE PREDICTION SYSTEM

The main difference between AROME-MetCoOP and MEPS is that AROME-MetCoOp only contains a deterministic prediction whereby MEPS has additionally nine individual perturbed ensemble member [MetCoOp Wiki, 2017].

Figure 2.5.1 shows the schematic of an ensemble prediction system (EPS). An ensemble forecasting system requires the definition of the initial amplitude and the horizontal and vertical structure of the perturbation. In general, the initial perturbation is chosen to be close to the observations. The initial condition for the disturbance is within a circle (Figure 2.5.1) of the observation uncertainty. In an ensemble prediction system one of the members is the deterministic forecast (single control forecast) where the other forecast members start from a slight perturbed state of the deterministic forecast. For a short time, should the forecast members be close together, this is a few hours in mesoscale prediction (deterministic in Figure 2.5.1). After a certain period of time, the forecast

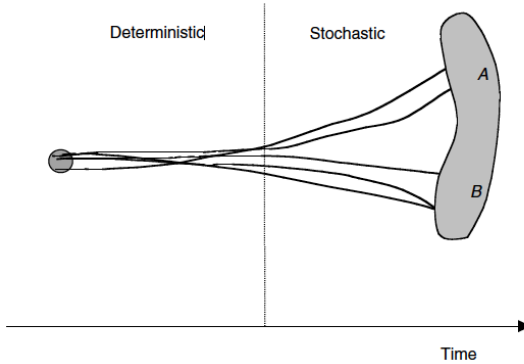


**Figure 2.5.1:** Schematic of ensemble prediction. Circle, representing the uncertainty of the initial conditions. Individual lines, perturbed ensemble member from the initial conditions ending in solution space, grey area [Kalnay, 2003].

of the different perturbed members are so large that they have to be considered as stochastic (Figure 2.5.1).

Important is, that the observations, which are going to be used for the initialisation are within the spread of the individual ensemble member forecasts [Kalnay, 2003].

### 2.5.2 METCOOP ENSEMBLE PREDICTION SYSTEM

In principle, MEPS is a short-term weather forecast consisting of ten ensemble members with 66 h prediction time and a horizontal resolution of 2.5 km and 65 vertical levels. Hourly 66 h forecast data is available at Met-Norway for the deterministic and the first perturbed ensemble member. 54 h forecasts are stored for the three hourly values.

The lower layer, near the ground is approximately 12 km height. With increasing height decreases the vertical resolution of 25 m to 200 m in the lower 3 km. The model top is located at approximately 23 km. The initialisation of each member is performed at 0 UTC, 6 UTC, 12 UTC and 18 UTC [MetCoOp Wiki, 2017]. Forecast data saved for the deterministic and first ensemble member have a time resolution of one hour for the 66 h forecast period. The other eight members have data stored every three hours for up to 48 h forecast time.

Figure 2.5.2a shows the MEPS model domain and its elevation as it was operational for December 2016. It covers Scandinavian countries including open water such as the Atlantic Ocean, the North and the Baltic Seas. A representation of the horizontal resolution zoomed for the Haukeliseter site is shown in Figure 2.5.2b. The topographical resolution of MEPS and its influence on local wind and precipitation will be discussed in Section 4.2.5. To compare the measurements from the surface with the MEPS data, the closest model grid point to Haukeliseter, is used (Figure 2.5.2). The closest grid point to Haukeliseter is 59.80° N, 7.22° E at 1041 m above sea level.

The centre of the model is approximately at 63.5° N, 15° E. The horizontal grid points are Lambert projected to receive the same area size of each grid cell. The regional model MEPS receives initial and boundary conditions from the global ECMWF-IFS (European Centre for Medium-Range Weather Forecasts Integrated Forecasting System) before it can produce its own regional forecasts. In addition, to produce the forecast analysis the background model is initiated for upper-air and surface data assimilation [Müller et al., 2017]. The horizontal resolution of the parent ECMWF

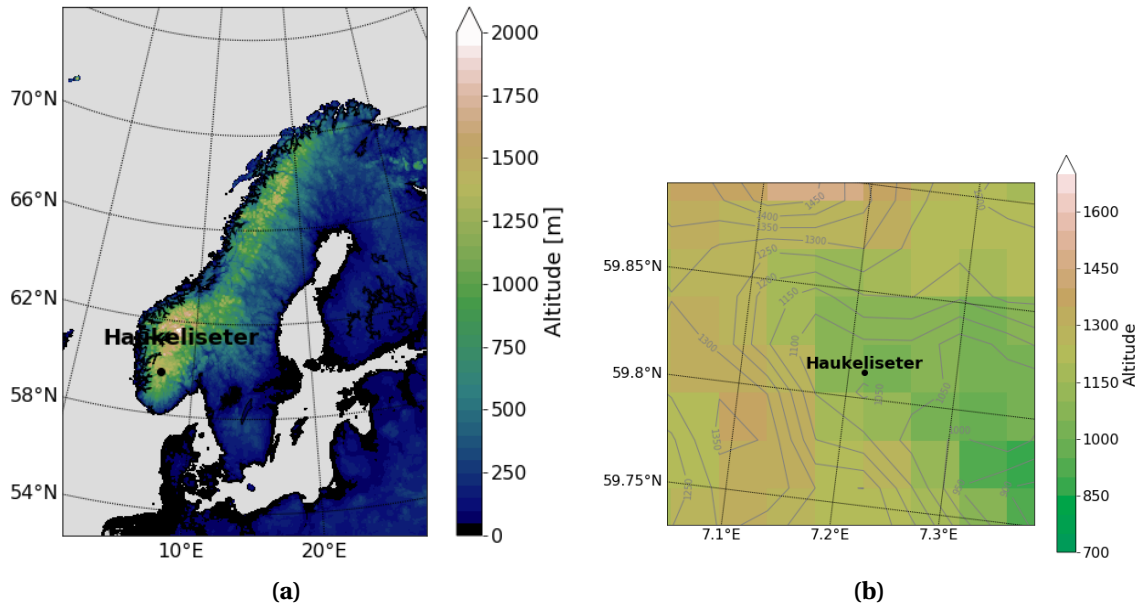


**Figure 2.5.2:** a: Elevation map of MEPS model domain. b: Representation of the topography around the measurement site Haukeliseter in MEPS. Contours and shading present the elevation of the grid cells.

grid is 9 km, has 137 model levels, and the model level top is at 80 km. The ECMWF-IFS forecasts are available 5 h later than the model runs at Met-Norway. MEPS is updated each third hour using observations received in real-time from the global observing system [Homleid and Tveten, 2016]. Since initial conditions such as observations have uncertainties as well as the model has internal variability, it has to reach a background climatology state (spin-up) before the output can be analysed. Warner et al. [1997] states, spin-up time varies depending on the amount and quality of the initial and boundary conditions. If only a few mesoscale initial condition are available then the model should be initialised well before the forecast time. This will allow the model to spin-up mesoscale structures that are responsive to large-scale and local forcing. In MEPS, the spin-up time can be assumed to be 6 h for precipitation [personal communication, Køltzow, 2018].

To model the snow in AROME-MetCoOp an one-layer atmosphere model scheme is implemented. The representation is covered by an adjustment of the three-class ice parametrization (ICE3) scheme (Section 2.5.4). This includes three variables such as: snow water equivalent (SWE), snow density, and snow albedo [Müller et al., 2017]. How liquid-phase processes are separated from slow ice-phase processes are described in Section 2.5.3.

### 2.5.3 MESO-NH AND THE ICE3 SCHEME

The physical parametrisation within AROME is based on the French research communities' Meso-NH. The microphysical scheme in the Meso-NH atmospheric simulation system is based on the Kessler scheme for liquid processes whereas the ICE3 parametrisation scheme is for cold processes [Meteo France, 2009]. The purpose of the scheme is to model as correctly as possible the ice phase in the atmosphere. The three-class parametrisation scheme is coupled to a Kessler scheme for the warm processes [Pinty and Jabouille, 1998]. McCumber et al. [1991] concluded from their case study of simulating two different types of tropical convection, that at least three different ice

categories are necessary to cover most precipitation but that applications might be case specific. According to the Meteo France [2009] documentation, the ice phase microphysical scheme includes:

**i:** pristine ice phase

**s:** snowflake type from lightly rimed large ice crystals or dry clusters, and

**g:** heavily rimed crystals, such as graupel, frozen drops or hail.

Within the ICE3 scheme no distinction between hail and graupel exists and therefore the physical discrimination is in the growth mode of graupel and hail is neglected.

To achieve snow water content within MEPS the number intercept parameter ( $N_0$ , [ $\text{m}^{-3}/\text{mm}$ ]), slope parameter of exponential size distribution ( $\lambda$ , [ $\text{m}^{-1}$ ]), mass diameter ( $D$ , [ $\text{mm}$ ]) and the particle size distribution [ $\text{m}^{-3}/\text{mm}$ ] of pristine ice ( $n_i$ ), snowflakes ( $n_s$ ), and rimed crystals ( $n_g$ ) has to be determined. According to Caniaux et al. [1994], the particle size distribution in the ICE3 scheme follows the Marshall-Palmer distribution (Equation (2.4.2)). The goal in ICE3 is to use a varying intercept parameter dependent on the ice category. The study of Caniaux et al. [1994] has shown that  $N_0$  can be parametrised with:

$$N_0 = C\lambda^x \quad (2.5.1)$$

$$\log_{10} C = -3.55x + 3.89$$

where  $C$  and  $x$  are constants depending on the ice category (Equation (2.5.1)).

The ice water content for primary ice, snowflakes, and rimed crystals is then assumed to be similar to Equation (2.4.7), but the integration limits range from zero to infinity and mass ( $(m$ , [ $\text{kg}$ ])), and particle size distribution ( $n(D)$ ) are dependent on the diameter of the hydrometeor particle. The mass of a single particle and PSD (Equations (2.5.2) and (2.5.3)) are represented depending on the ice category (Table 2.5.1)

$$m(D) = aD^b \quad (2.5.2)$$

$$n(D) = N_0 g(D) \quad (2.5.3)$$

$a$ ,  $b$  are the characterisations of the parameters according to their type (Table 2.5.1) and  $g(D)$  the generalised Gamma function:

$$g(D) = \frac{\alpha}{\Gamma(\nu)} \lambda^{\alpha\nu} D^{\alpha\nu-1} \exp(-(\lambda D)^\alpha) \quad (2.5.4)$$

with  $\alpha$ ,  $\nu$  the shape and tail dispersion parameters and  $\Gamma(\nu)$  the gamma function.

After following the above equations including Equation (2.4.7) the exponential slope parameter of pristine ice, snow, and rimed crystals,  $\lambda$  can be generated with  $G(b)$ , the gamma function:

$$\lambda = \left( \frac{\text{SWC}}{aG(b)} \right)^{\frac{1}{x-b}} \quad (2.5.5)$$

**Table 2.5.1:** Characterization parameters for primary ice (**i**), snowflakes (**s**) and rimed crystals (**g**). Values are based on Meteo France [2009] and Pinty and Jabouille [1998]. The mixing ratio **r** for primary ice, snowflakes, and rimed crystals [ $\text{kg kg}^{-1}$ ]; dispersion parameter  $\alpha$  - shape,  $v$  - tail; characterisation parameter according to particle type  $a, b$ ; parameters of the fall speed-diameter relationship  $c, d$ ; ice category constants  $C, x$ .

	<b>r<sub>i</sub></b>	<b>r<sub>s</sub></b>	<b>r<sub>g</sub></b>
$\alpha, v$	3.3	1.1	1.1
$a$	0.82	0.02	196
$b$	2.5	1.9	2.8
$c$	800	5.1	124
$d$	1.0	0.27	0.66
$C$		5	$5 \times 10^5$
$x$		1	-0.5

For all hydrometeors the terminal fall velocity based on the diameter,  $D$  is assumed.

$$V(D) = c D^d \left( \frac{\rho_{00}}{\rho_{dref}} \right)^0 .4. \quad (2.5.6)$$

In Equation (2.5.6) the last factor is the Foote and Du Toit [1969] correction of the air density and  $\rho_{00}$  being the air density at the reference pressure level  $P_{00}$ .

Figure 2.5.3 shows the summary of the microphysical processes for mixed phase clouds. The study focuses mostly on solid precipitation particles and therefore only the initiation and growth of pristine ice crystals **i**, snowflakes **s**, and rimed crystals **g** is presented.

Following Pinty and Jabouille [1998] and Figure 2.5.3 it can be seen how AROME calculates ice growth.

- The ICE3 scheme starts with *cold* - 'slow' processes for ice processes (right side in Figure 2.5.3)
  - homogeneous (HON) and heterogeneous (HEN) nucleation
  - vapour deposition of snow and graupel particles (DEP)
  - aggregation (AGG) and auto conversion (AUT)
- The second step is to initiate the *warm* processes (left side in Figure 2.5.3)
- Then including the
  - aggregation and conversion-melting (CVM) for snowflakes and
  - contact freezing of raindrops (CFR)
- Followed by AGG and melting for graupel (MLT)
- And the melting from pristine ice and the Wegener-Bergeron-Findeisen (BER) effect
- finally integrate the sedimentation terms

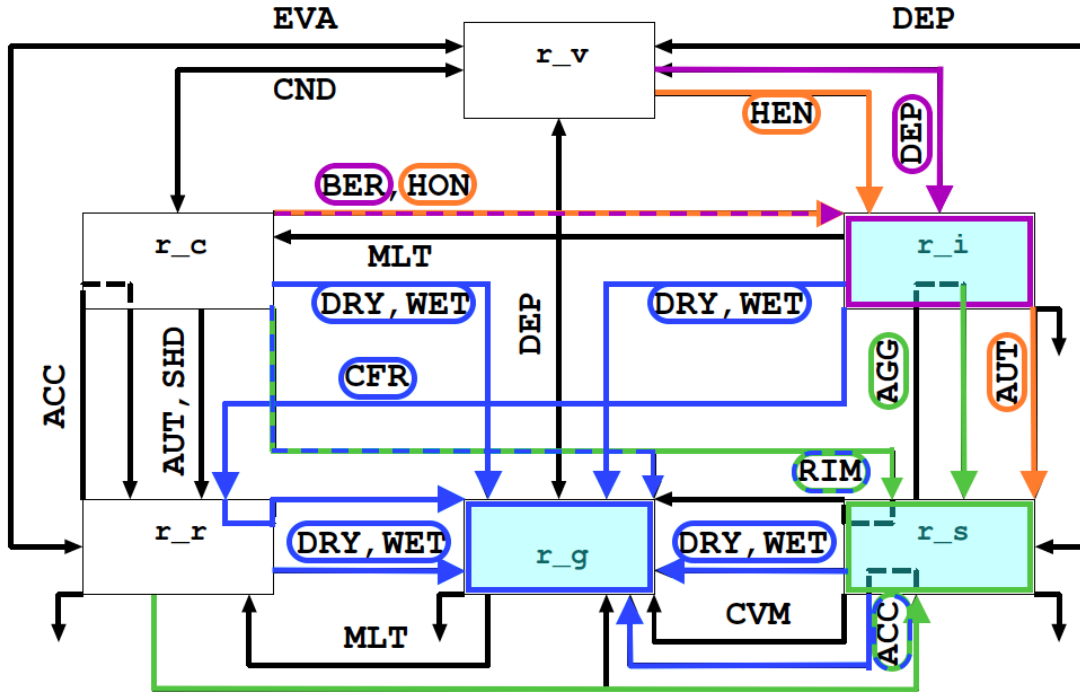


**Figure 2.5.3:** Microphysical processes for mixed phase clouds in the ICE3 scheme in AROME [adapted from Meteo France, 2009]. Orange lines show the initiation processes of pristine ice crystals and snowflakes (**s**). Purple lines and boxes present the growth mechanisms of **i** (BER, DEP). Green lines demonstrate the expansion of the snowflakes (RIM, AGG, ACC). Graupel (**g**) forms as an effect of heavy riming (RIM) by collision of larger raindrops with snowflakes (ACC), WET/DRY growth or contact freezing of raindrops (CFR). All graupel growth processes are indicated by blue lines were hail formation is included.

#### 2.5.4 AROME-METCoOP ADJUSTMENT

Since the ICE3 scheme showed some weaknesses in AROME-MetCoOp for the boreal winter month, Müller et al. [2017] introduced some modifications. During cold conditions (2 m temperature between  $-5^{\circ}\text{C}$  and  $-10^{\circ}\text{C}$ ) the ICE3-scheme followed too low 2 m temperature in AROME-MetCoOp. Furthermore, too much ice fog or low clouds were simulated for 2 m temperature  $\leq -15^{\circ}\text{C}$ , all year long. After implementing the modifications such as separating fast liquid-phase processes from the slower ice-processes, as well as reducing sublimation speed of ice particles. Also, taking into account the difference of optical thickness between ice-phase clouds and water, mixed-clouds reduced the negative 2 m temperature bias [Müller et al., 2017]. A negative aspect of these adjustments was that the occurrence of fog increased.

## 2.6 COMPUTING SNOW QUANTITIES

The following section describes how the different model variables where processed to achieve a comparison between the retrieved observed values and the forecast model output.

### 2.6.1 MEPS

Vertical hybrid coordinates are terrain-following and are mass-based, [Müller et al., 2017]. MEPS underlies non-hydrostatic dynamics, MetCoOp Wiki [2017].

MEPS has a vertical resolution in hybrid sigma pressure coordinates, which starts at the surface and decreases with height. To calculate the actual vertical pressure in [hPa], AROME uses the vertical discretisation based on Simmons and Burridge [1981].

$$p(n, k, j, i) = a_p(k) + b_p(k) \cdot p_s(n, j, i) \quad [\text{Pa}]. \quad (2.6.1)$$

$p_s$  is the surface air pressure in Pa,  $a_p$ ,  $b_p$  are the vertical coordinate parameters. Prognostic variables are at model level  $k$ .  $n$  is the forecast time,  $j$  and  $i$  are the latitudal and longitudinal grid points, respectively.

The next step was to convert pressure-levels into actual heights with the help of the hypsometric equation. Here, the air temperature in model levels is used to calculate the mean temperature of each thickness layer.

$$\bar{T} = \frac{\int_{p_1}^{p_2} T \partial \ln p}{\int_{p_1}^{p_2} \partial \ln p} \quad [\text{K}] \quad (2.6.2)$$

Martin [2006] presents steps of differentiating the hypsometric equation by using the virtual air temperature. But when the atmospheric mixing ratio is large, the virtual temperature will only be 1 % larger than the actual air temperature. Since the error is small, calculations are done with the provided air temperature in model levels.

The thickness,  $\Delta z$ , of each layer is then calculated by using the hypsometric equation from Martin [2006] and the previously calculated mean temperature (Equation (2.6.2)):

$$\Delta z = z_2 - z_1 = \frac{R_d \bar{T}}{g} \ln \left( \frac{p_1}{p_2} \right) \quad [\text{m}] \quad (2.6.3)$$

where  $R_d$  is gas constant for dry air with a value of  $287 \text{ J kg}^{-1} \text{ K}^{-1}$ , standard gravity  $g = 9.81 \text{ m s}^{-2}$ .  $p_1$  and  $p_2$  are the pressure levels at lower and higher levels ( $p_2 < p_1$ ).

### 2.6.2 SNOW WATER CONTENT

To get a valid comparison between the SWC from the optimal estimation retrieval and the results from MEPS, the SWC is averaged hourly respectively three hourly. Taking the model initialisation of MEPS at 0 UTC the instantaneous model forecast values are saved every hour for the deterministic and first ensemble member. Three hourly data is available for the second to tenth perturbed member. To approach hourly mean values from the retrieved SWC an average over 30 min prior and 30 min after each full hour is performed. Hence, in Section 4.2.4 and 4.2.5 hourly (three-hourly) retrieved averages are compared with instantaneous forecast values.

Since MEPS has a higher vertical resolution than the optimal estimation snowfall retrieval, each vertical profile of SWC is averaged in 200 m intervals. To accomplish the same vertical resolution only values above 100 m altitude are used to start at the same range height as given from the MRR (Section 2.3.2).

Within the output from MEPS snow water content does not exist for each model layer. Hence the calculation of the SWC is performed by using the three solid precipitation categories given in MEPS. Namely the instantaneous mixing ratio of snow ( $r_s$ ), graupel ( $r_g$ ) and the cloud ice ( $r_i$ ). The mixing ratios are represented in  $\text{kg kg}^{-1}$  and a transformation to  $\text{gm}^{-3}$  is performed. Densities of each model level ( $\rho$ ) are calculated with Equation (2.6.1) and the model level air temperature. These are then multiplied with the sum of the solid precipitation mixing ratio.

$$\rho = \frac{p}{R_d T} \quad [\text{kg m}^{-3}] \quad (2.6.4)$$

$$SWC = \rho \cdot (r_s + r_g + r_i) \cdot 10^6 \quad [\text{gm}^{-3}]. \quad (2.6.5)$$

The same is done for liquid water content in the atmosphere, just cloud condensed water and rain amount are summed.

### 2.6.3 SNOW WATER PATH

The snow water path (SWP) is the vertically integrated and averaged SWC (Equations (2.4.7) and (2.6.5)):

$$SWP = \int_{h_0}^{h_1=3000\text{m}} SWC(h) dh \approx \frac{h_1 - h_0}{6} \left[ SWC(h_0) + SWC(h_1) + 4SWC\left(\frac{h_0 + h_1}{2}\right) \right] \quad [\text{gm}^{-2}] \quad (2.6.6)$$

The snow water path is a measure of the weight of frozen particles per unit area. It indicates the total amount of ice in the atmosphere.

## 2.7 STATISTICS

For this thesis I calculated ensemble mean, coefficient of variation, mean error, mean absolute error, and percent difference. The model ensemble mean ( $\bar{f}$ ) is the average of all ten ensemble members ( $f_i$ ) of MEPS.

$$\bar{f} = \frac{\sum_{i=1}^n f_i}{n} \quad (2.7.1)$$

The coefficient of variation (CV) is represented by the standard deviation,  $\sigma$  with respect to the ensemble mean. The standard deviation is defined as:

$$\sigma = \sqrt{\frac{\sum_{i=1}^n (f_i - \bar{f})^2}{n-1}}. \quad (2.7.2)$$

The CV gives the variability between the individual ensemble member forecast for SWC (Table 4.2.5). Furthermore, the variation around the deterministic forecast shows. Since the CV is normed over the ensemble mean, daily variations can be compared to each other for the Christmas 2016 storm period (Section 4.2.4).

$$CV = \frac{\sigma}{\bar{f}} \quad (2.7.3)$$

In Section 4.1 mean error ( $ME$ ) and mean absolute error ( $MAE$ ) is used. The  $ME$  for each model ensemble member and from the observations ( $o_i$ ) is calculated with:

$$ME = \frac{\sum_{i=1}^n f_i - o_i}{n} \quad (2.7.4)$$

For the mean absolute error ( $MAE$ ) follows then:

$$MAE = \frac{\sum_{i=1}^n |f_i - o_i|}{n} \quad (2.7.5)$$

The percentage difference of double fence gauge and retrieved surface accumulation (Table 4.2.1 and 4.2.2) and MEPS forecasts (Table 4.2.3 and 4.2.4) are calculated by:

$$\% \text{Difference} = \frac{f_i - o_i}{o_i} \times 100 \quad (2.7.6)$$

$f_i$  presents the snowfall from the retrieval or the MEPS ensemble forecast. The mean is then taken from all % Difference values to see the average deviation during the Christmas storm 2016.

## 2.8 EXTREME WEATHER

'Extreme weather' is a meteorological term, associated with the extent of a weather type. The Norwegian Meteorological Institute declares an extreme event, if strong winds, large amounts of precipitation and large temperature changes are expected before the event occurs. As well as a large avalanche risk is present and coastal areas are influenced by extremely high-water levels. Generally, an event is divided into four phases by Met-Norway to be called extreme event [Pedersen and Rommetveit, 2013].

**Phase A:** *Increased monitoring before the possible extreme weather.* The meteorologists give special attention to the weather situation. At this point it is not certain, that there will be an extreme weather event.

**Phase B:** *Short-term forecasts.* It is decided, that there will be an extreme event. The forecasts are more detailed, and updates will be published at least every six hours. The event will get a name.

**Phase C:** *The extreme weather is in progress.* The meteorologists send out weather announcements at least every six hours.

**Phase D:** *The extreme weather event is over. Clean-up and repairs are in progress.* When the extreme weather is over the public is notified and information about the upcoming weather and clearing work is given.

The Christmas storm was considered an extreme event by the Met-Norway, named 'Urd' [Olsen and Granerød, 2017]. The average wind along the coast of Western Norway reached hurricane strength (observed:  $40 \text{ ms}^{-1}$  to  $55 \text{ ms}^{-1}$ ). In South and Eastern Norway, west to north-west winds between  $25 \text{ ms}^{-1}$  to  $40 \text{ ms}^{-1}$  were measured. At Haukeliseter, 136.4 mm of precipitation were measured from 21 to 27 December 2016. The 2016 Christmas storm was just above the limit of been called an extreme weather event.

To understand which damage a storm can have, Færaas et al. [2016] released a table to associate wind strength with damage (see Table 2.8.1).

**Table 2.8.1:** Damage related to wind speed, from Færaas et al. [2016].

slight storm	$20.8 \text{ ms}^{-1}$ – $24.4 \text{ ms}^{-1}$	Large trees sway and hiver. Roofs can blow down.
full storm	$24.5 \text{ ms}^{-1}$ – $28.4 \text{ ms}^{-1}$	Trees are pulled up with clutter. Big damages to houses.
strong storm	$28.5 \text{ ms}^{-1}$ – $32.6 \text{ ms}^{-1}$	Extensive damage.
hurricane	$>32.6 \text{ ms}^{-1}$	Unusually large destruction.

## 2.9 INTEGRATED VAPOUR TRANSPORT

An atmospheric river (AR) is a filament structure of intense moisture transport from the tropics to higher latitudes. Heavy precipitation can be associated with it, because the air is warm and moist. This can often be observed at mountain ranges at west coasts such as in Norway [Azad and Sorteberg, 2017]. Due to orographic lifting the moisture will be released and follow high amounts of precipitation.

An atmospheric river is characterised if the integrated vapour transport shows values higher than  $250 \text{ kg m}^{-1} \text{ s}^{-1}$  and a continuous region larger than 2000 km [Rutz et al., 2014].

The integrated vapour transport (IVT, Section 3.3) was calculated from the ECMWF data as followed:

$$IVT = \frac{1}{g} \int_{p_{sfc}}^{100\text{hPa}} q \mathbf{V} dp \quad [\text{kg m}^{-1} \text{ s}^{-1}] \quad (2.9.1)$$

where  $g$  is the standard gravity,  $q$  the specific humidity, and  $\mathbf{V}$  the total wind vector at each pressure level  $p$ . The numerical, trapezoidal integration is performed by using data from the surface pressure  $p_{sfc}$  to 850 hPa in 50 hPa intervals and from 700 hPa to 100 hPa in 100 hPa intervals.

## 2.10 NORTH ATLANTIC OSCILLATION

It has long been known that precipitation and temperature fluctuations occur during European winter in connection with NAO (North Atlantic Oscillation). The NAO is a redistribution of atmospheric mass between the North Atlantic high (Azores high), and the polar low (Iceland low). The NAO index is defined as the gradient between the sea level pressure of the Azores high and the Icelandic low during the winter months (December - March) [Hurrell, 1995]. Positive index shows the deepening of the Icelandic low and a strengthening of the Azores high and negative indexes respectively [Uvo, 2003].

Positive NAO is associated with stronger westerlies than usual across the middle latitudes of the Atlantic [Uvo, 2003]. In addition, more moisture is transported to Scandinavia [Hurrell, 1995]. A positive NAO during winter is often associated with higher temperatures than normal and with an increase in precipitation in northern Europe and low temperatures in southern Europe [Uvo, 2003].

# CHAPTER 3: ANALYSIS OF THE CHRISTMAS STORM 2016

Extreme storm Urd was chosen for an in depth examination for a number of intriguing reasons:

- I) the Haukerlister site is a WMO sanctioned weather station with single and double fence rain gauge measurements,
- I) additional instruments were placed at the site for the winter 2016/2017 season allowing for the vertical profiling of snow properties and snowfall accumulation
- III) the MEPS forecasting system had recently become the operational model platform for Met-Norway, and
- IV) the unique temporal evolution of the precipitation properties during the event

A preliminary analysis identified periods of both good agreement of snow accumulation measurements by MEPS in comparison to the ground observations, as well as periods of overestimation by MEPS. The above factors make for an interesting study to assess and better understand the usefulness of the measurements in question.

The next sections will provide a definition of an extreme weather event, a description of the weather maps that were utilized, and a presentation of the synoptic scale evolution of the storm.

Prior to the analysis, each weather maps' purpose will be presented to understand the connections between them. All the weather maps are generated using data from ECMWF operational model Cycle 43r1. The analysis consists of 137 model levels. To reduce computational costs it is reduced to the *octahedral reduced Gaussian grid* and then interpolated to a N640 Gaussian grid [Dando, 2016].

## 3.1 DYNAMIC TROPOPAUSE

The dynamic tropopause maps (DT), presented herein (e.g. Figure 3.2.0a) are comprised of the potential temperature (shading) and wind barbs [ $\text{m s}^{-1}$ ] on the two PVU surface (one PV unit =  $10^{-6} \text{ m}^2 \text{s}^{-1} \text{K kg}^{-1}$ ), and the 925–850 hPa averaged relative vorticity (black contours - every  $0.5 \times 10^{-4} \text{ s}^{-1}$  only positive values are plotted). An example is presented in Figure 3.2.0a. High (low) values of potential temperature represent an elevated (suppressed) tropopause. Regions with a large horizontal gradient of potential temperature indicate a steeply-sloping tropopause that is associated with an enhanced pressure gradient force and winds. From this, the mid-latitude

jet stream can be pointed out. The low-level averaged relative vorticity is plotted to provide a three-dimensional (in the vertical) picture of the atmosphere. It is useful for identifying cyclone centres and attendant frontal boundaries.

The 925–850 hPa layer-averaged surface relative vorticity is shown in black contours, every  $0.5 \times 10^{-4} \text{ s}^{-1}$ . It represents the rotation of a fluid.

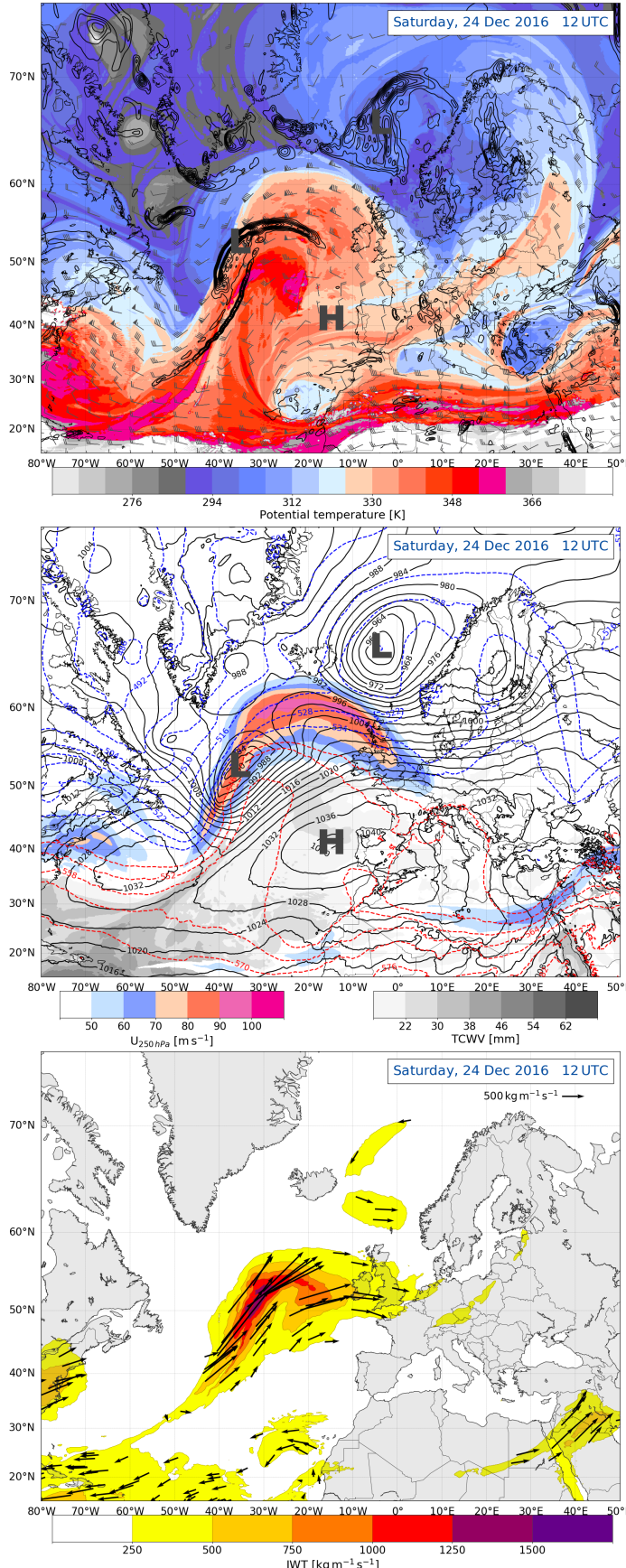
Along the Rossby-Wave-Guide, troughs and ridges are seen which can be combined with the surface relative vorticity to understand the vertical dynamic interaction in the atmosphere. Wave disturbance travel along the wave guide or regions of strong gradients. At the dynamic tropopause level the Rossby-Wave-Guide is the region of strong potential temperature gradient, shading in Figure 3.2.0a [Nielsen-Gammon, 2001]. In case of a westward tilt between the surface cyclone and an upper level through an intensification of the surface cyclone is more likely to occur.

## 3.2 SURFACE, THICKNESS, WIND

A complementary view of the three-dimensional structure of the atmosphere is also presented: 250 hPa wind speed (colour shading,  $\text{m s}^{-1}$ ), mean sea level pressure (black contours, hPa), 1000–500 hPa thickness (dashed contours) and the total precipitable water (black-white shading, mm). See Figure 3.2.0b for an example.

The dashed, coloured contours in Figure 3.2.0b show the vertical thickness between the 1000 hPa and 500 hPa surface, every 6 dam. The thickness between two pressure levels can be interpreted via the hypsometric equation (Equation (2.6.3)), which equates the thickness to the mean temperature of the layer in question. In a relative sense, a larger thickness indicates a warmer air mass. In addition, strong horizontal gradients in the thickness field can be related to frontal boundaries. Specific to the discussion in this thesis, the thickness field also provides useful information regarding the form of precipitation (liquid, frozen).

Analysis of the mean sea level pressure can be used to identify cyclones (L) and anticyclones (H) at the surface as well as provide supplementary information regarding frontal boundaries (Figure 3.2.0b). The total precipitable water is a measure of the column integrated moisture. It represents an instantaneous measure of moisture in time and space, which can be useful when assessing the amount of moisture that may fall as precipitation in future time steps. The 250 hPa wind speeds are used to identify strong upper-level flow (i.e. the jet stream) and can be directly compared to the dynamic tropopause map (Figure 3.2.0a).



**a:** Dynamic tropopause analysis map at 2 PVU. Potential temperature [K] at the 2 PVU surface, shaded according to the colour bar. Total wind, barbs [ $\text{m s}^{-1}$ ], and 925 – 850 hPa layer-averaged surface relative vorticity (black contours, every  $0.5 \times 10^{-4} \text{ s}^{-1}$ ).

**b:** Jet, thickness, mean sea level pressure, and total precipitable water synoptic analysis. 250 hPa wind speed, shaded according to the colour bar, [ $\text{m s}^{-1}$ ]. 1000 – 500 hPa thickness, dashed contours every 6 dam, MSLP, black contours every 4 hPa, total column water vapour [mm], shaded according the grey scale.

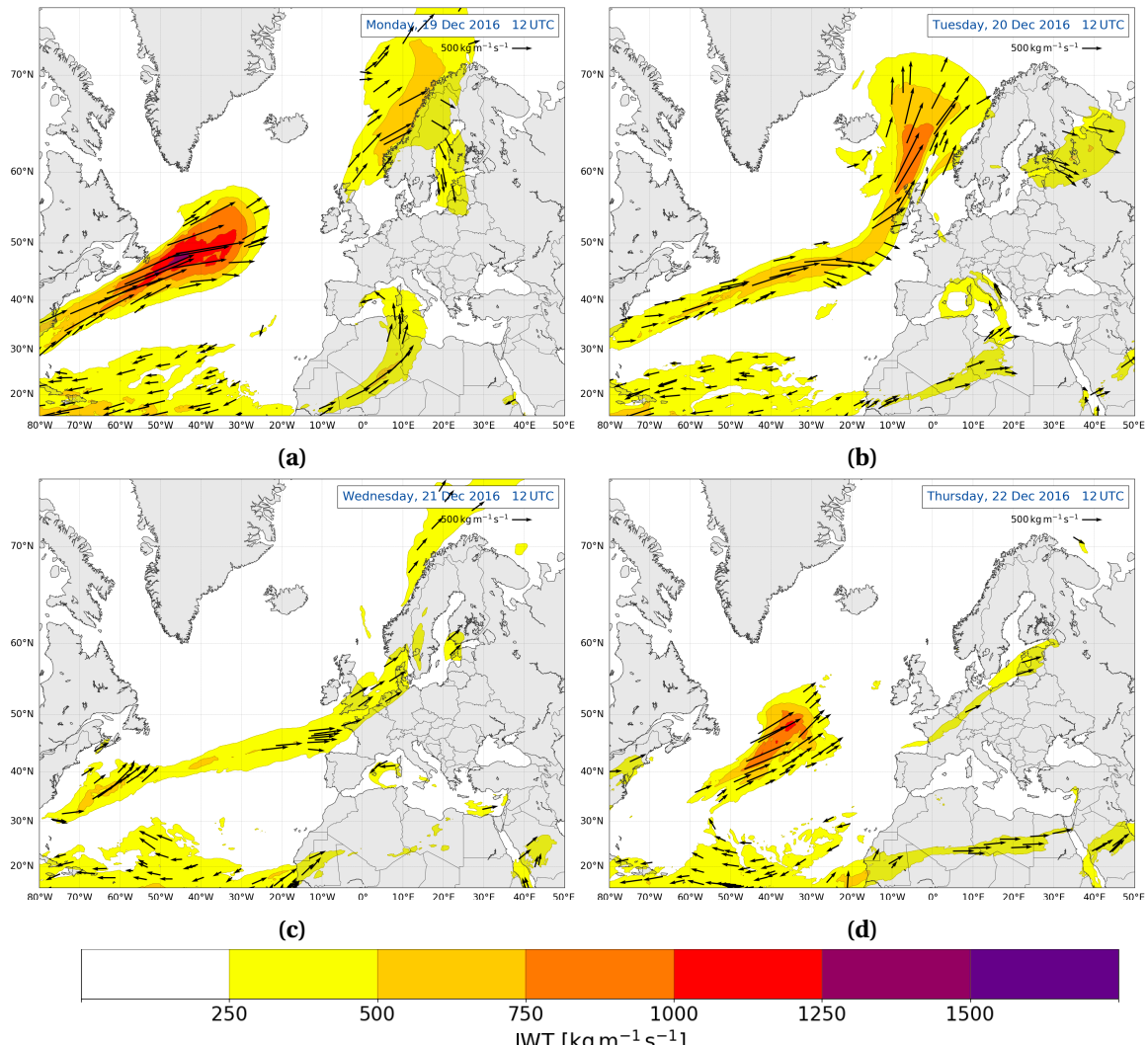
**c:** Integrated vapour transport analysis map. Integrated vapour transport, shaded according to the colour bar [ $\text{kg m}^{-1} \text{s}^{-1}$ ]. Vectors, indicating the direction and magnitude of the IVT.

**Figure 3.2.1:** ECMWF analysis on 24 December 2016 at 12 UTC. L and H indicating the surface low and high pressure, respectively.

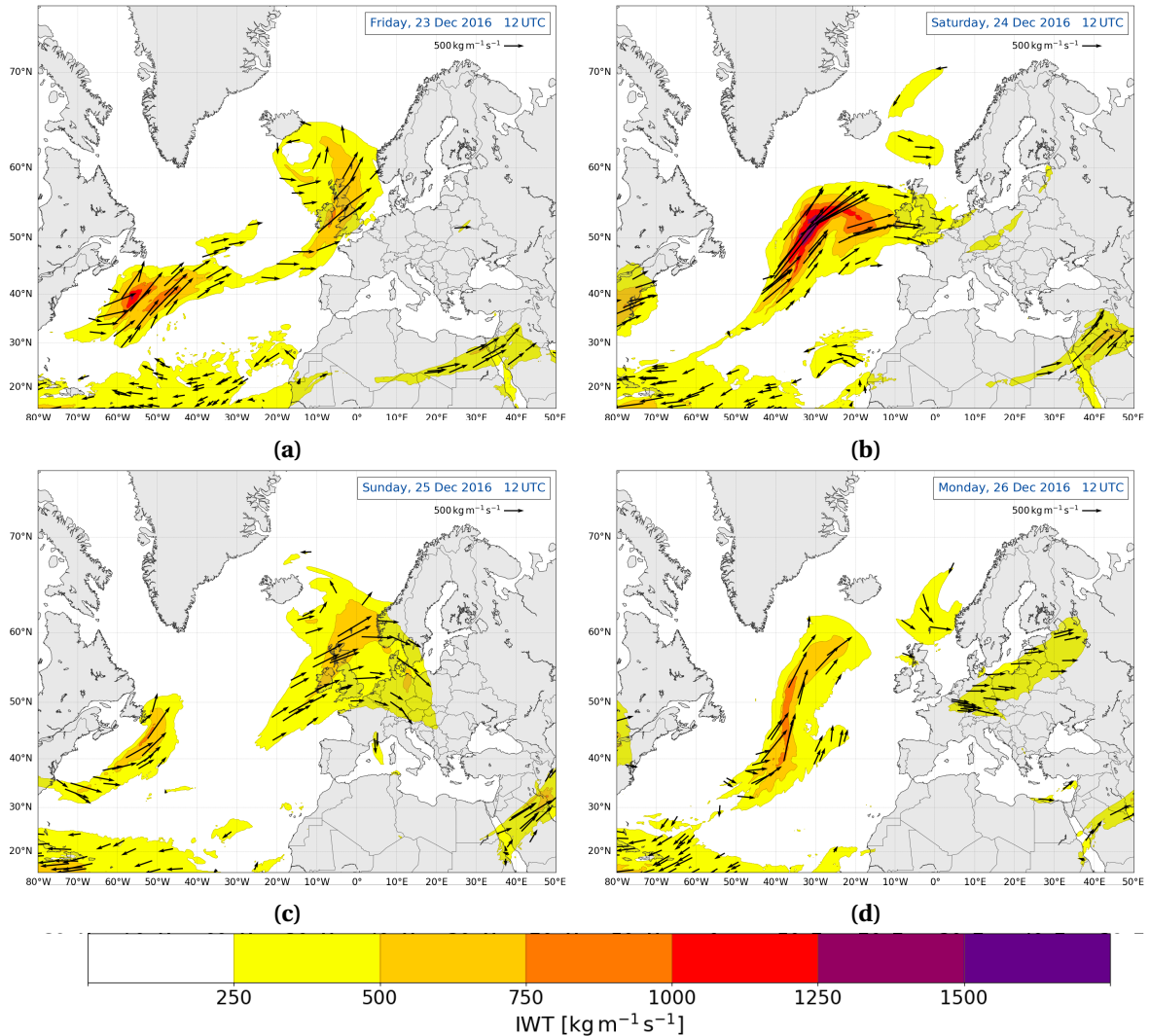
### 3.3 INTEGRATED VAPOUR TRANSPORT

Figure 3.2.0c shows coloured contours of the integrated vapour transport (IVT) in  $\text{kg m}^{-1} \text{s}^{-1}$ , where warmer colours indicate higher IVT. Stream vectors in Figure 3.2.0c indicate the direction and intensity of the IVT flow.

Analysing integrated vapour transport maps is important, since extreme precipitation events in Norway are often influenced by moist, warm air advection from the tropics [Azad and Sorteberg, 2017]. Figure 3.3.1 and 3.3.2 shows integrated vapour transport from the tropics to the midlatitudes, but it also presents that the occurrence of the atmospheric river was not the main factor which led to intense precipitation during the 2016 Christmas storm. Since it showed not to be intense it will not be further discussed.



**Figure 3.3.1:** Atmospheric river analysis map, data from ECMWF. During 19 to 22 December 2016 at 12 UTC, chronologically (a to d). IVT, shaded according to the colour bar [ $\text{kg m}^{-1} \text{s}^{-1}$ ]. Vectors, indicating the direction and magnitude of the IVT.



**Figure 3.3.2:** (As Figure 3.3.1.) During 23 to 26 December 2016 at 12 UTC, chronologically (a to d)

### 3.4 OBSERVATIONS

It is a primary goal of this work to relate the local weather observations from the WMO site at Haukeliseter to the synoptic scale structure and the additional measurements taken at Haukeliseter during the winter of 2016/2017.

Examples of the 60 min precipitation accumulation from the double fence rain gauge, 2 m air temperature, and wind observations are presented in Figure 3.4.1 to document the continuous precipitation at Haukeliseter during the extreme event. The temperature evolution will be used to investigate possible changes in the type of precipitation.

Snowfall is likely for temperatures up to  $2^\circ\text{C}$ . The intensity of the storm can be classified by the hourly averaged wind speed and direction as wind barbs in  $\text{m s}^{-1}$ . To understand which damage a storm can have, Færaas et al. [2016] released a table to associate wind strength with damage (see Table 2.8.1).

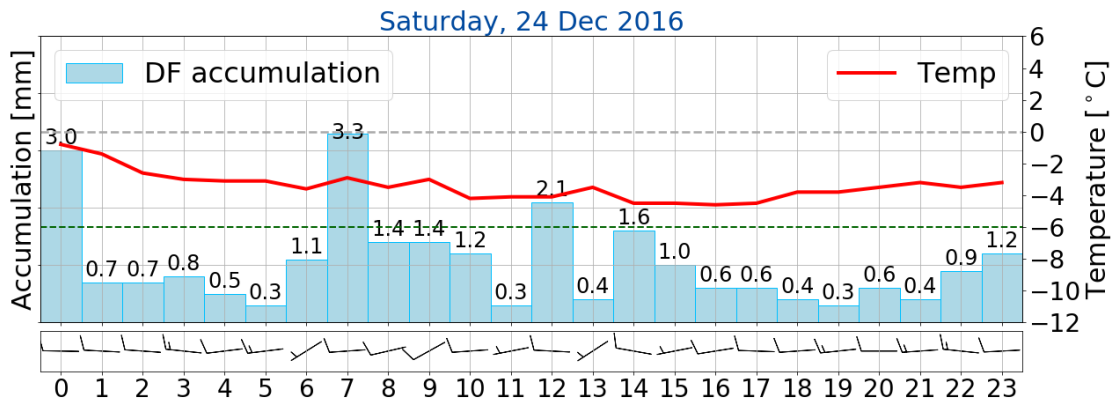


**Figure 3.4.1:** Surface precipitation, 2 m temperature and 10 m wind observation from the weather mast at Haukeliseter on 24 December 2016. 60 min total accumulation [mm] in light blue as bar, 2 m temperature (red,  $^{\circ}\text{C}$ ), and 10 min mean wind observations at 10 m, as barbs [ $\text{m s}^{-1}$ ]. Grey dashed line indicates the freezing temperature and the green dashed line the 30-year climate mean temperature of  $-6^{\circ}\text{C}$ . Hourly processed data taken from eklima [2016].

### 3.5 LARGE SCALE CIRCULATION

In the following the large scale circulation between 19 and 26 December 2016 is analysed.

In December 2016, the NAO was positive, with +0.4, and negative sea level pressure for the Iceland low [Shi et al., 2016] was monitored. Since extreme weather events are often related to positive NAO might this explain the incident of the extreme Christmas storm in 2016.

#### 19 TO 20 December 2016

A precursor to extreme storm Urd was a high-pressure system over Scandinavia and an occluded low to the proximate east of Iceland (Figure 3.5.1a, b). Over the coming 36 h a confluence of events resulted in a suppressed tropopause and cold air over Haukeliseter: a filament of a cut off low to the south and cold air advection from the north-east (Figure 3.5.1a, b).

#### 21 December 2016

Associated with the previously mentioned occluded cyclone, cold air impinges on Scandinavia on 21 December 2016 (Figure 3.5.2b, d). Moisture is transported from the low latitudes to high latitudes, influencing Norway's west coast. The westerly flow in Figure 3.5.2d is additionally conducive to orographic lifting. This is coincident with the onset of precipitation at Haukeliseter at 10 UTC on 21 December 2016 (Figure 3.5.2e). Furthermore, given the low temperatures, solid phase precipitation is observed.

Additionally, cyclogenesis is observed off the east coast of the United States (as evidenced by a trough to the northwest of low-level averaged relative vorticity).

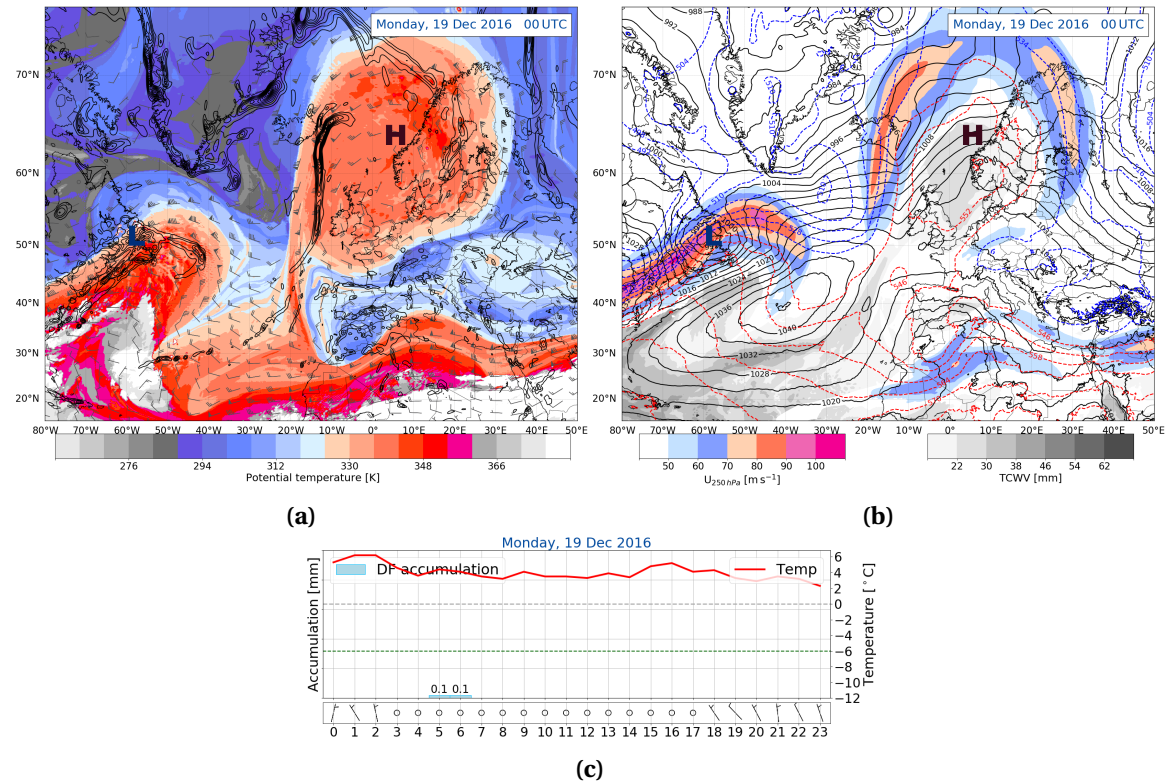


**Figure 3.5.1:** ECMWF analysis for dynamic tropopause (a) as described in Section 3.1, thickness map (b) as evaluated in Section 3.2, and local observations (c) at Haukeliseter explained in Section 3.4). Analysis is shown for 19 December 2016 at 00 UTC. Surface lows are indicated as L and surface highs as H.

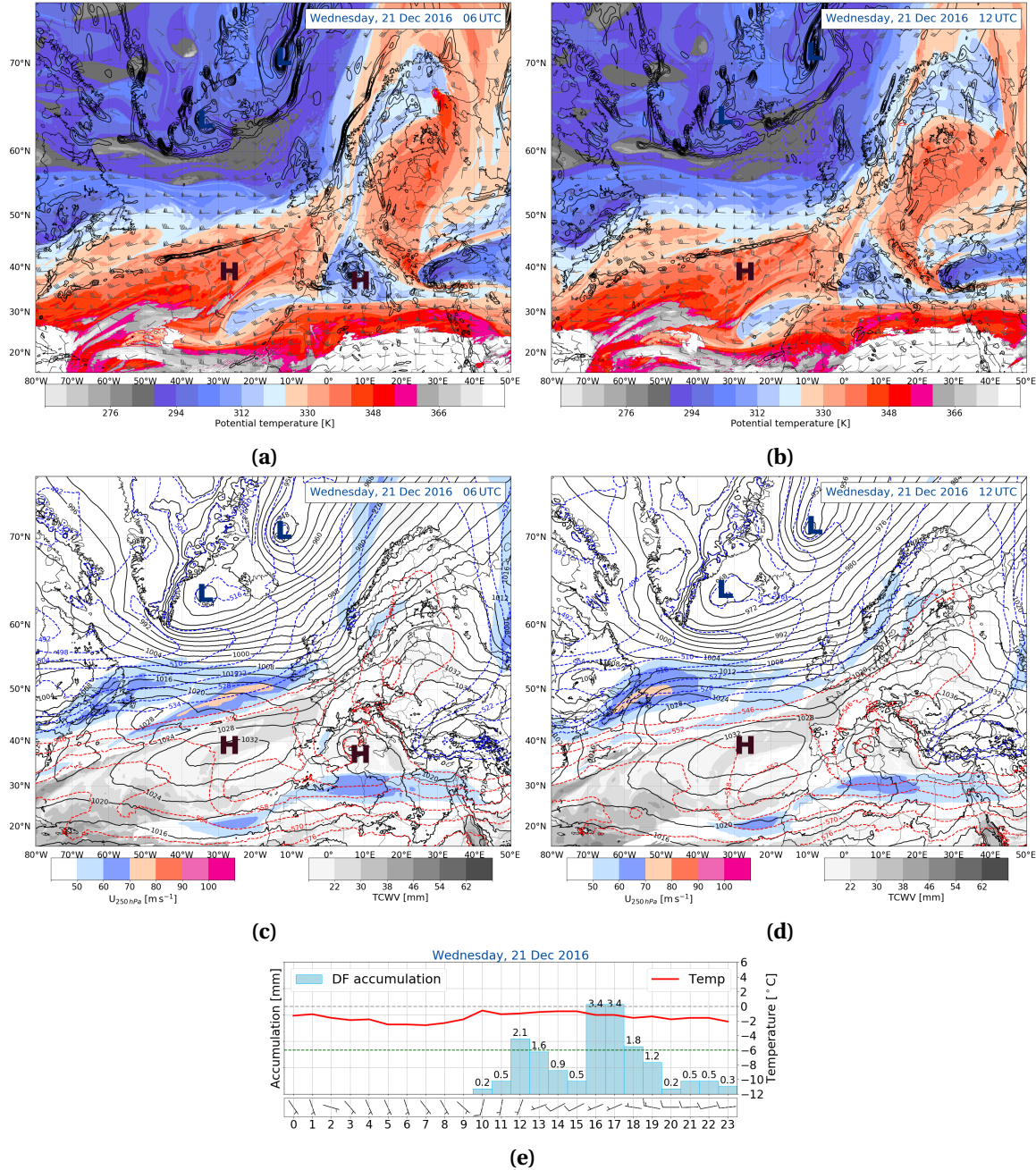


**Figure 3.5.2:** (As Figure 3.5.1.) For 21 December 2016 at 6 UTC (a, c) and at 12 UTC (b, d).

22 December 2016

Twenty-four hours later the analysis from 22 December 2016 shows cold air remaining over Scandinavia (Figure 3.5.3a, b). Continuous frozen precipitation is observed at Haukeliseter (Figure 3.5.3c). The previously mentioned cyclone is observed to intensify during this time period along the baroclinic zone. The upper-level trough to the north-east of the low-level cyclone centre represents an optimal configuration for cyclone development, since the surface low is located below the temperature gradient at the 2 PVU surface (Figure 3.5.3a, b). This is apparent in the intensification of the surface system (low-level averaged vorticity and mean sea level pressure minima) at 50° N. Also, in evidence is the diabatic ridging associated with the ascending warm conveyor belt air-stream (see warm colours in Figure 3.5.3a).

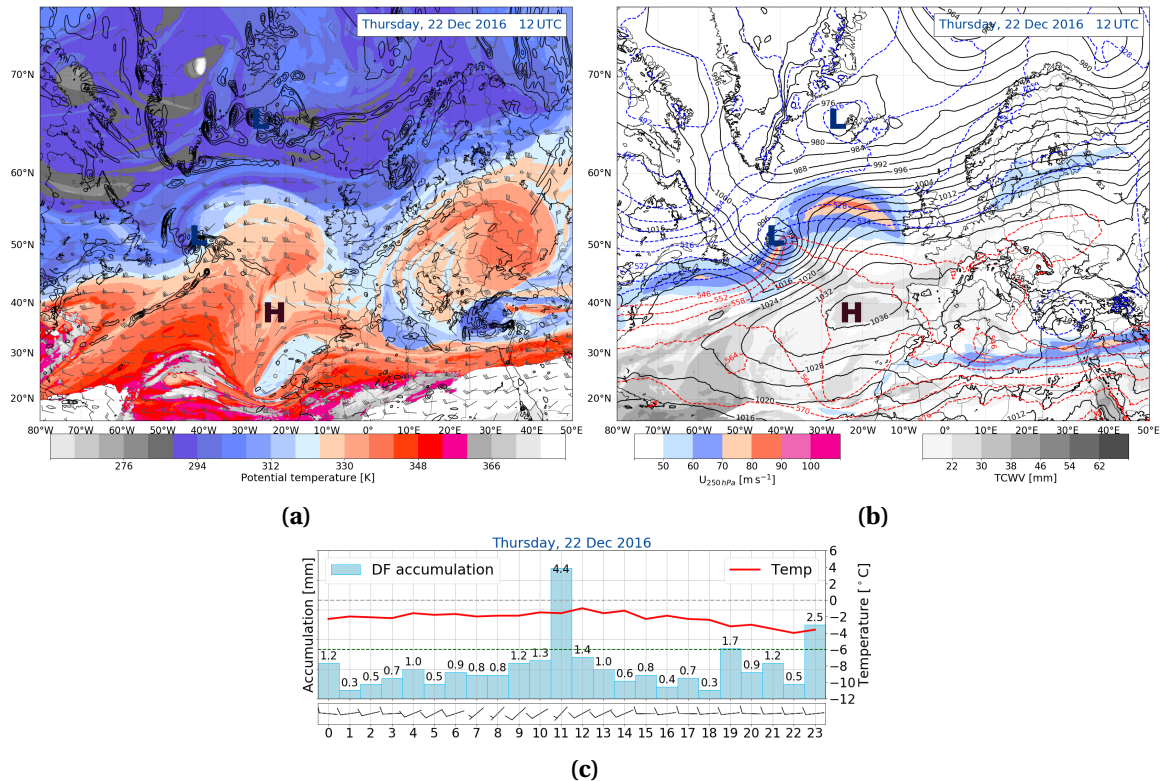


**Figure 3.5.3:** (As Figure 3.5.1.) For 22 December 2016 at 12 UTC.

23 December 2016

The west Atlantic cyclone translates along the jet stream (Figure 3.5.4c, d). The occluded front of the storm arrives roughly between 6 UTC and 12 UTC. By 12 UTC an elevated tropopause is observed in Figure 3.5.4a. The surface temperature rises (Figure 3.5.4e), and mixed phase precipitation is related to the increased temperature and moisture transport from the low latitudes Figure 3.5.4c. A cyclogenesis event occurs in the west Atlantic with a similar disposition of an upper-level trough and a low-level baroclinic zone at 40° N (Figures 3.5.4a to 3.5.4d).

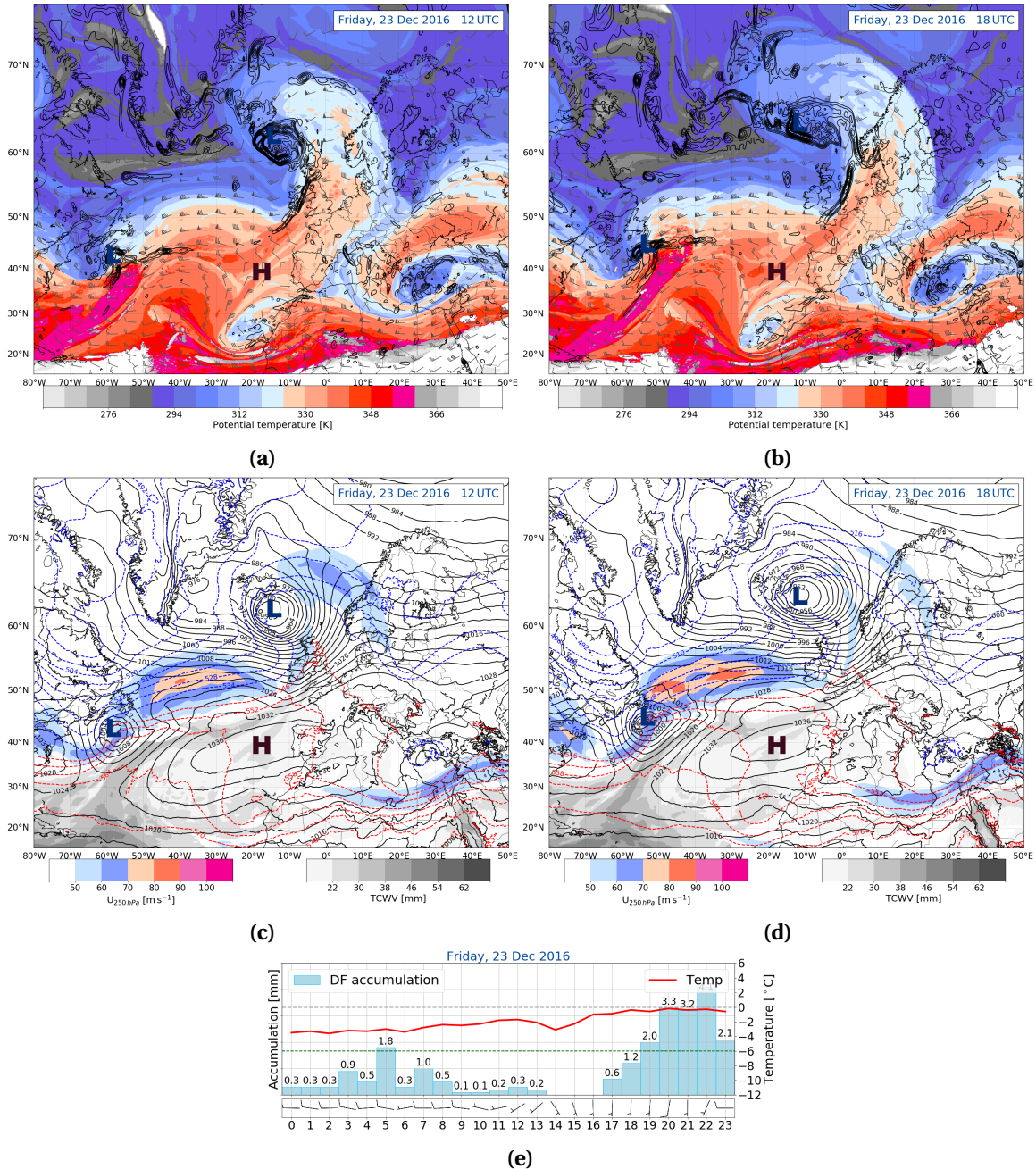


**Figure 3.5.4:** (As Figure 3.5.1.) For 23 December 2016 at 12 UTC (a, c) and at 18 UTC (b, d).

24 December 2016

After the passage of the occluded front over Norway, passes cold air into Scandinavia (Figure 3.5.5a, b). The temperature drops in Figure 3.5.5c), and solid phase precipitation resumes. The importance of moisture transport is emphasized by the integrated water vapour plot (Figure 3.3.2b). This represents a crucial component to the high precipitation amounts that were measured at the observational site. This represents a quantitative confirmation of previous climatological studies of extreme, cold-season precipitation [Azad and Sorteberg, 2017, Moore, unpublished].

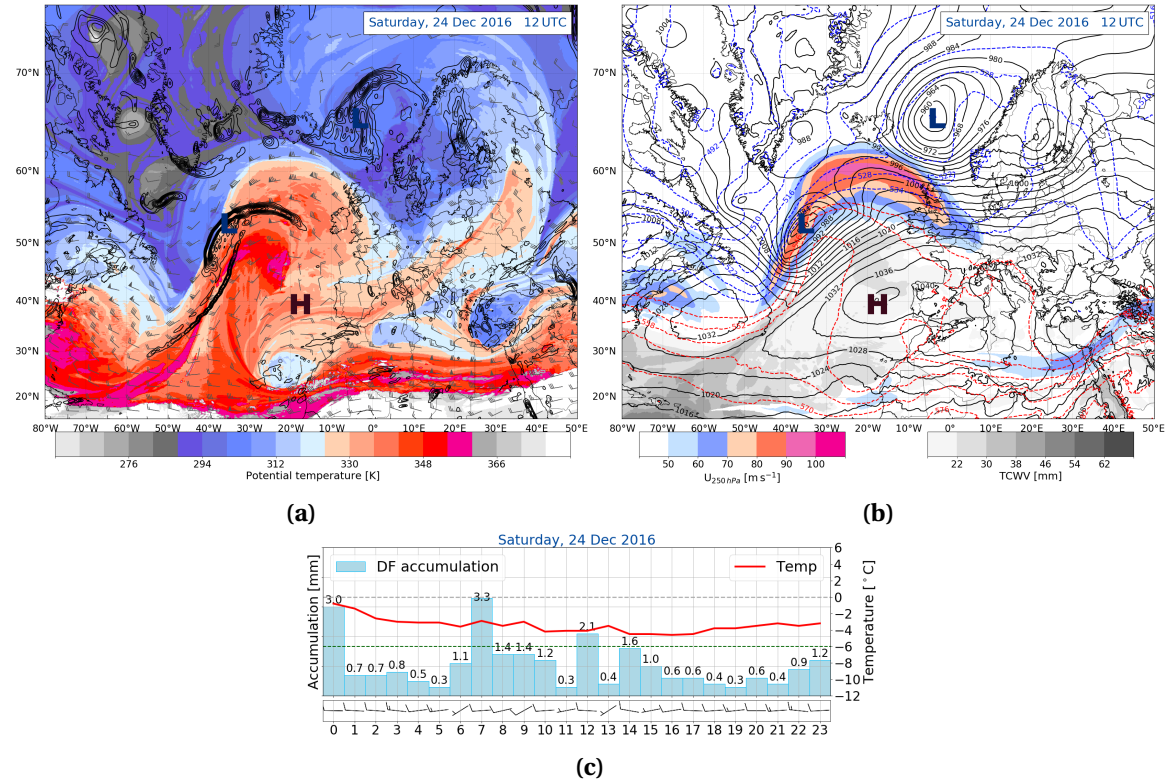


**Figure 3.5.5:** (As Figure 3.5.1.) For 24 December 2016 at 12 UTC.

25 December 2016

Twenty-four hours later the upper level ridge is more pronounced and covers large parts of Norway (Figure 3.5.6a). The cyclone south-east of Iceland has built its frontal boundaries (Figure 3.5.6c). Between 12 UTC and 18 UTC the warm sector passes through Haukeliseter (Figure 3.5.6c, d, e). Connected to the warm sector the temperature rises in Figure 3.5.6e and the precipitation becomes liquid.

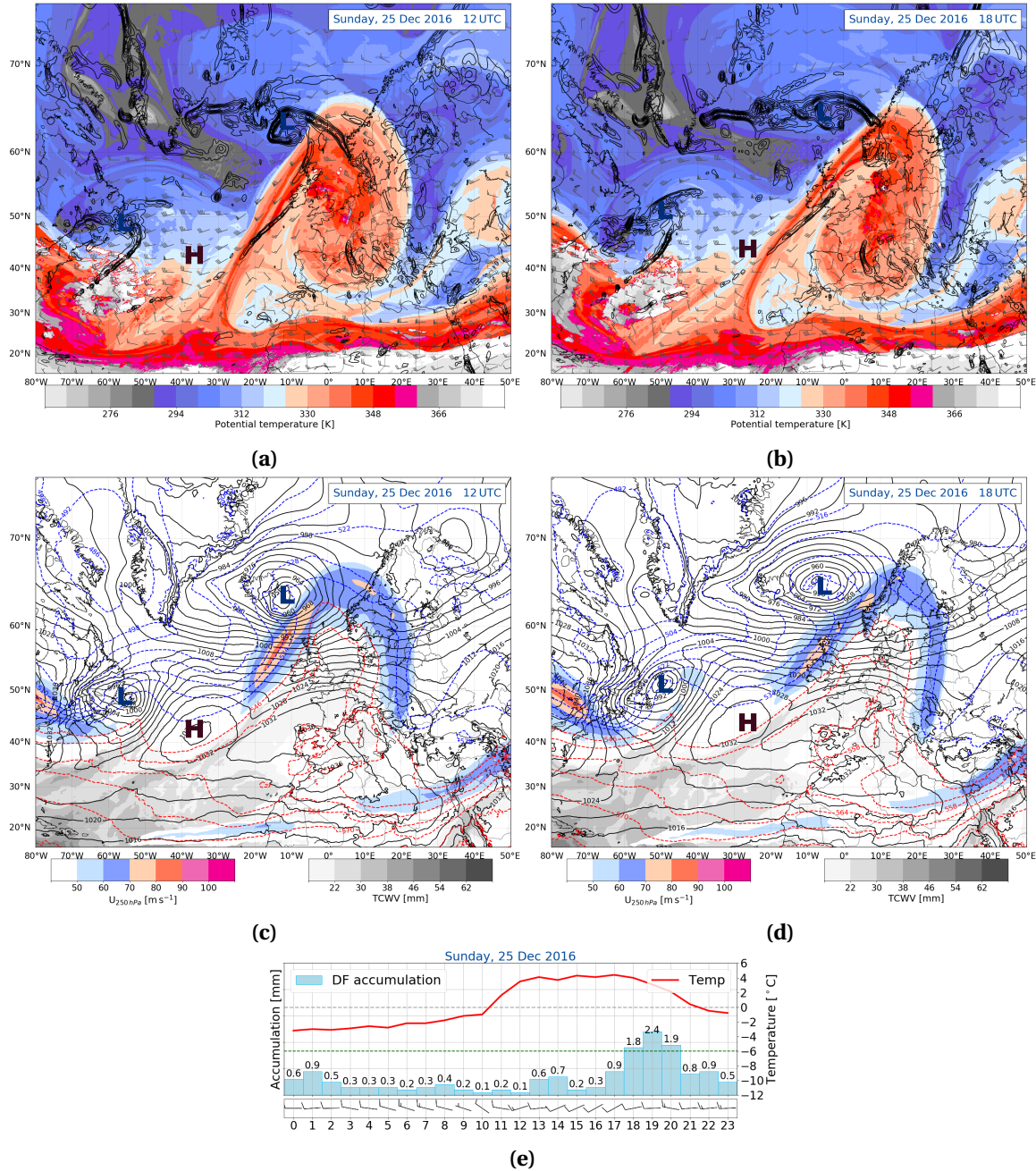


**Figure 3.5.6:** (As Figure 3.5.1.) For 25 December 2016 at 12 UTC (a, c) and at 18 UTC (b, d).

26 December 2016

Within the next twenty-four hours the cold sector comes through Haukeliseter and Norway is covered in cold air (Figure 3.5.7a, d). The surface pressure indicates the occlusion of the cyclone and therefore a weakening and dissipation by 18 UTC. A drop in temperature and a change in precipitation phase is observed at Haukeliseter (Figure 3.5.7e).

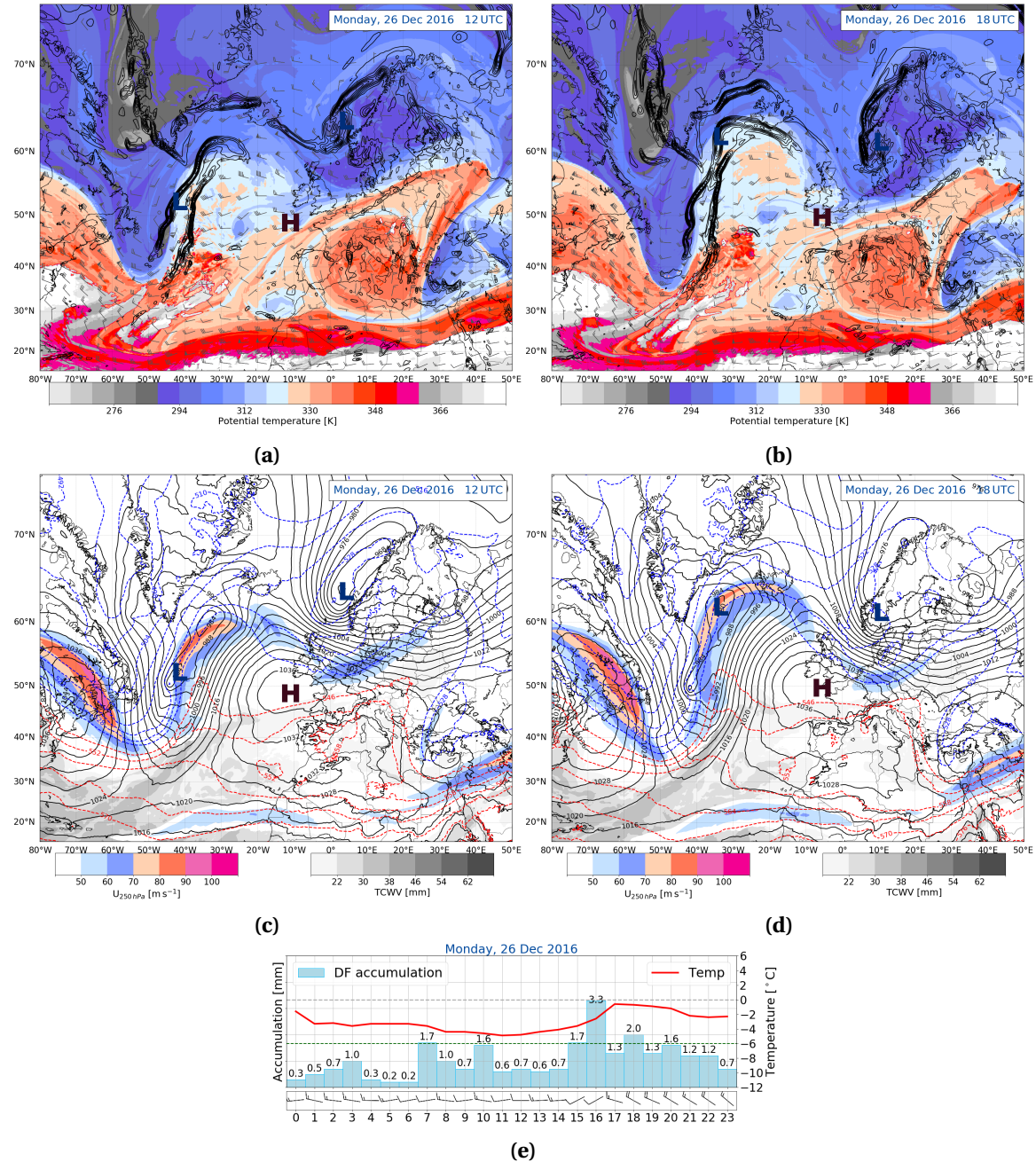


**Figure 3.5.7:** (As Figure 3.5.1.) For 26 December 2016 at 12 UTC (a, c) and at 18 UTC (b, d).



# CHAPTER 4: SNOW OBSERVATIONS AND MEPS COMPARISON

In this chapter the results of the snow surface observations, and the regional mesoscale forecast model at Haukeliseter are presented. On the basis of the methodology described in Chapter 2 it should be evaluated if the regional mesoscale forecast model MEPS predicts the same synoptic patterns as observed at the measurement site. Furthermore, snow water content forecasted by MEPS is being compared with the retrieved vertical SWC at Haukeliseter.

This study will show a comparison between observed and forecasted snow, for one particular extreme event, the 2016 Christmas storm.

## 4.1 THE CHRISTMAS STORM 2016 - METEOROLOGY

A comparison between the surface observations at Haukeliseter and the ECMWF analysis of the dynamic tropopause and geopotential thickness maps show that frontal transitions occurred on three days during the 2016 Christmas storm, 23, 25, and 26 December 2016 (Section 3.5). The frontal passages show up in the measurements and MEPS ensemble forecasts (Figures 4.1.1 to 4.1.6).

Figures 4.1.1 to 4.1.6 displays the observations and model forecast quantities for sea level pressure, 2 m air temperature, 10 m wind, and precipitation on 21 to 26 December 2016 for the Haukeliseter measurement site.

During all days the MEPS forecasts seem to predict similar sea level pressure, 2 m air temperature, and 10 m wind direction as were observed. Overestimations are simulated for wind speed (Figures 4.1.1 to 4.1.6d) and surface precipitation amount (Figures 4.1.1 to 4.1.6e).

Figures 4.1.7 to 4.1.9 presents the correlation of sea level pressure, 2m air temperature, 10m wind, and surface precipitation amount between the observations and the 48 h MEPS ensemble forecast. The relation for Haukeliseter observations and the MEPS forecast members is indicated with the regression calculated for each day. The scatter plots in Figures 4.1.7 to 4.1.9 show a good correlation for sea level pressure and 2 m air temperature. Sea level pressure has the best correlation of all variables. The MEPS forecast shows a disagreement with southerly observed winds in Figure 4.1.8a, between 21 and 23 December 2016. A good agreement is seen for wind direction in Figure 4.1.8b for 24 to 26 December 2016. Wind speed is overestimated throughout the event and will be further investigated in Section 4.2.5 (Figure 4.1.8c, d). Surface

precipitation amount agrees better between 21 to 23 December 2016 (Figure 4.1.9a) than during 24 and 26 December 2016 (Figure 4.1.9b). Figure 4.1.9a suggests a better correlation below 20 mm for 21 to 23 December 2016 than above. A detailed discussion about the precipitation overestimation at the surface is given in Section 4.2.3.

Sea level pressure and 2 m air temperature usually have a good correlation by nature. Pressure and temperature take positive and negative values and a histogram would show a normal distribution. On the other hand, wind speed and precipitation, can only have positive values. In addition, the distribution for wind and precipitation is usually skewed, since more small values are observed, predicted than high values. Furthermore, precipitation is spatially dependent. It does not rain all over Norway the same amount at the same time.

On 23 and 26 December 2016, pressure decreases and increases, as well as temperature increases, and wind changes are present. Since these changes show up in the surface observations it is assumed that frontal boundaries passed through Haukelieseter. As described in Section 3.5 the ECMWF dynamic tropopause analysis (Figure 3.5.4a) shows an elevated tropopause on 23 December 2016, than on the previous days. Warm air is advected closer to Southern Norway (Figure 3.5.4a). The low-pressure system approaches in the course of the day south-east of Iceland and hence stronger west to south-west winds are associated with the cyclone (Figure 3.5.4c). The MEPS forecast, initialised on 23 December 2016 at 0 UTC in Figure 4.1.3a simulates the sea level pressure observations and shows the decrease in pressure to 990 hPa after 12 UTC due to the passage of the occluded front. After the transition of the occlusion the pressure stays constant. Since warmer air is more advected to the north and the DT in Figure 3.5.4a shows a warm low-pressure core, an increase in temperature, from  $-3^{\circ}\text{C}$  to  $0^{\circ}\text{C}$ , is observed and predicted at the measurement site (Figure 4.1.3b). The 10 m wind observations show a change from west to south and 10 min wind of  $8 \text{ ms}^{-1}$ . The 25 December 2016 (Figure 4.1.5) shows an increase of temperature to  $+5^{\circ}\text{C}$ , between 15 UTC and 17 UTC leading to the assumption of a warm sector passage in Figure 4.1.5b. The overall weather situation, described in Section 3.5, showed that a warm front as well as cold front influenced Norway on 25 December 2016. Since pressure and wind do not indicate a change related to frontal development (Figure 4.1.5a, c, d), it is assumed that the warm air section between the warm and cold front is only shown in the surface measurements at Haukeliseter (Figure 4.1.5b).

As the cyclone moves to the north-east, further into the Norwegian Sea, a wind change is apparent in the ECMWF analysis (Figure 3.5.4c). First westerly winds and later south-westerly winds are associated with the low-pressure system. The MEPS ensemble forecasts and observations in Figure 4.1.3c and d indicate a wind change from west to south with a slight decrease in wind speed. On 23 December 2016, the evolution of the occlusion is also observed by an increase in precipitation. Before 18 UTC the surface accumulation shows light precipitation (Figure 4.1.3e). During the passage of the occlusion the observed surface accumulation increases which is associated to continuous, heavy precipitation shown in Figure 4.1.3e.

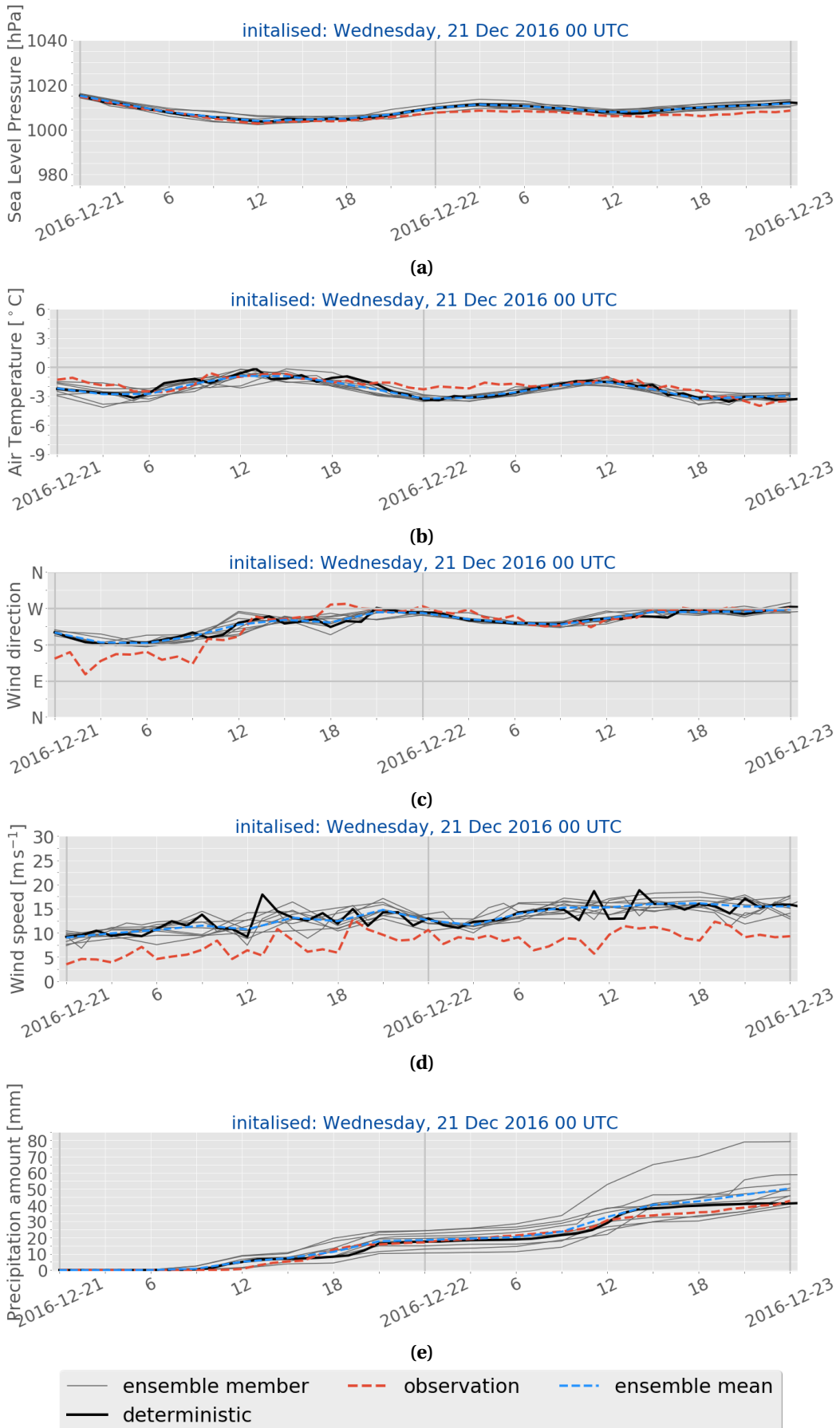


**Figure 4.1.1:** 48 h surface observations and MEPS ensemble forecasts initialised on 21 December 2016 at 0 UTC. Line representation according to the label. From top to bottom: sea level pressure, 2 m air temperature, 10 m wind direction and speed, and precipitation amount. In a Passages of low pressure (**L**) and high pressure (**H**) are marked.

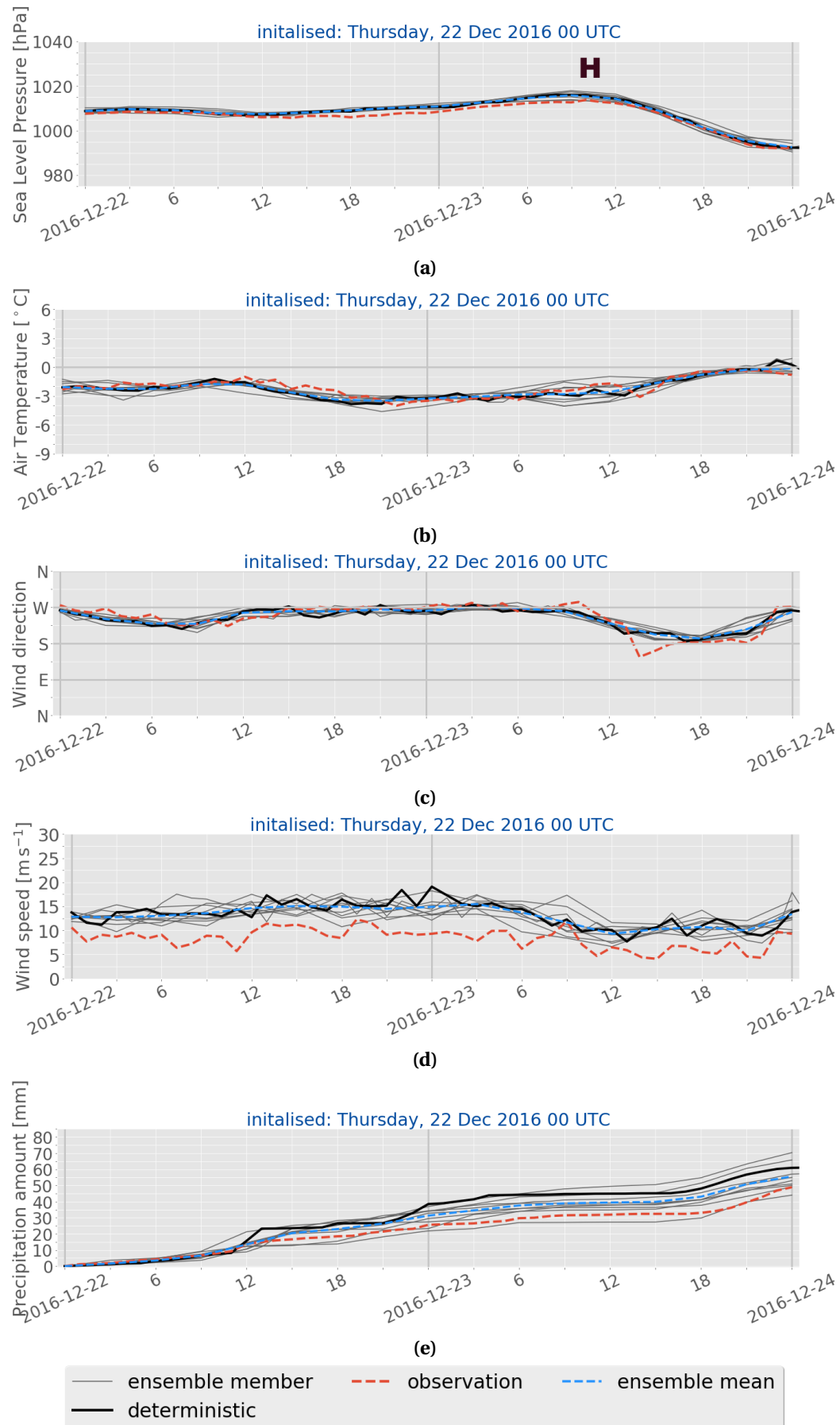


**Figure 4.1.2:** (As Figure 4.1.1.) Initialisation on 22 December 2016 at 0 UTC.

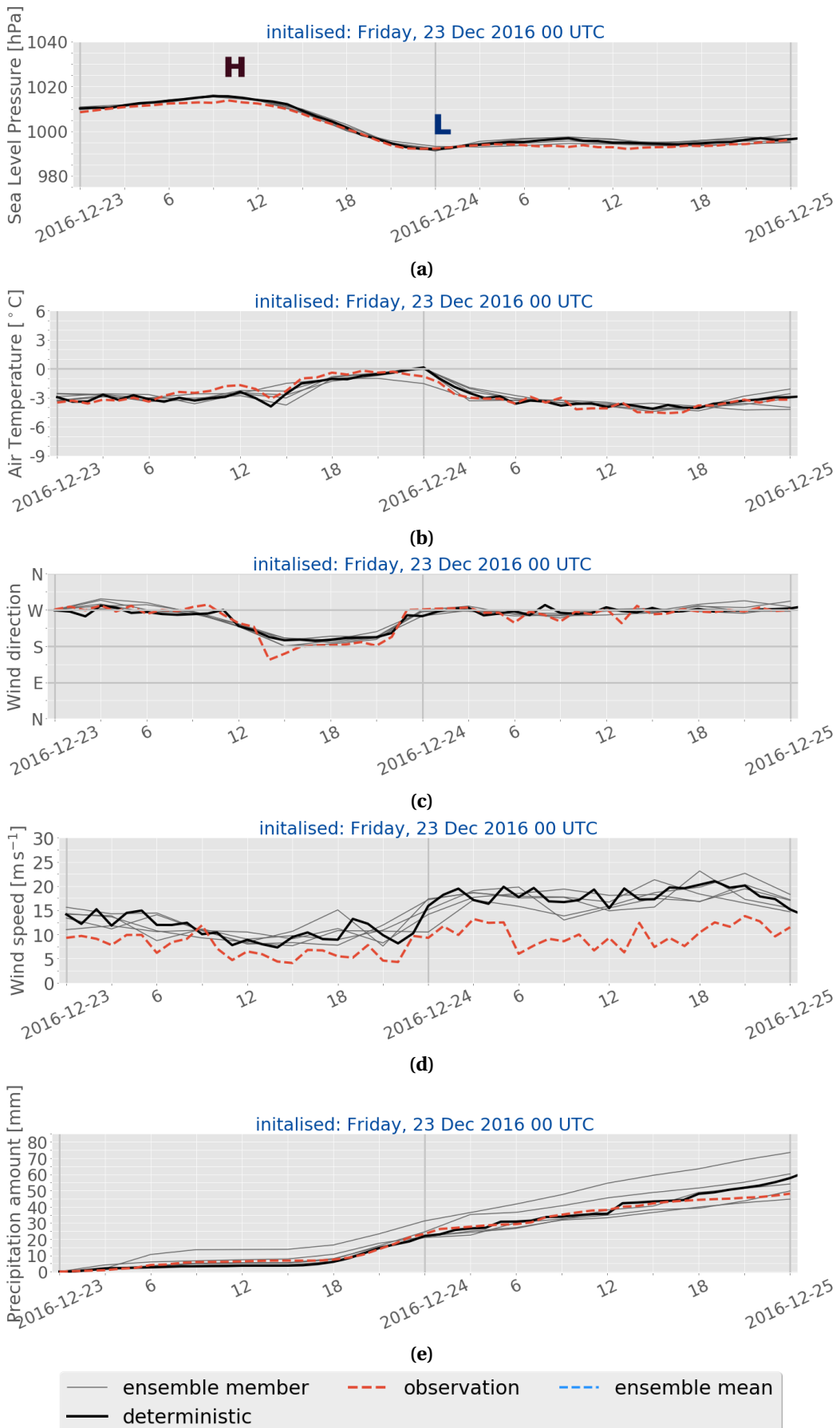


**Figure 4.1.3:** (As Figure 4.1.1.) Initialisation on 23 December 2016 at 0 UTC.

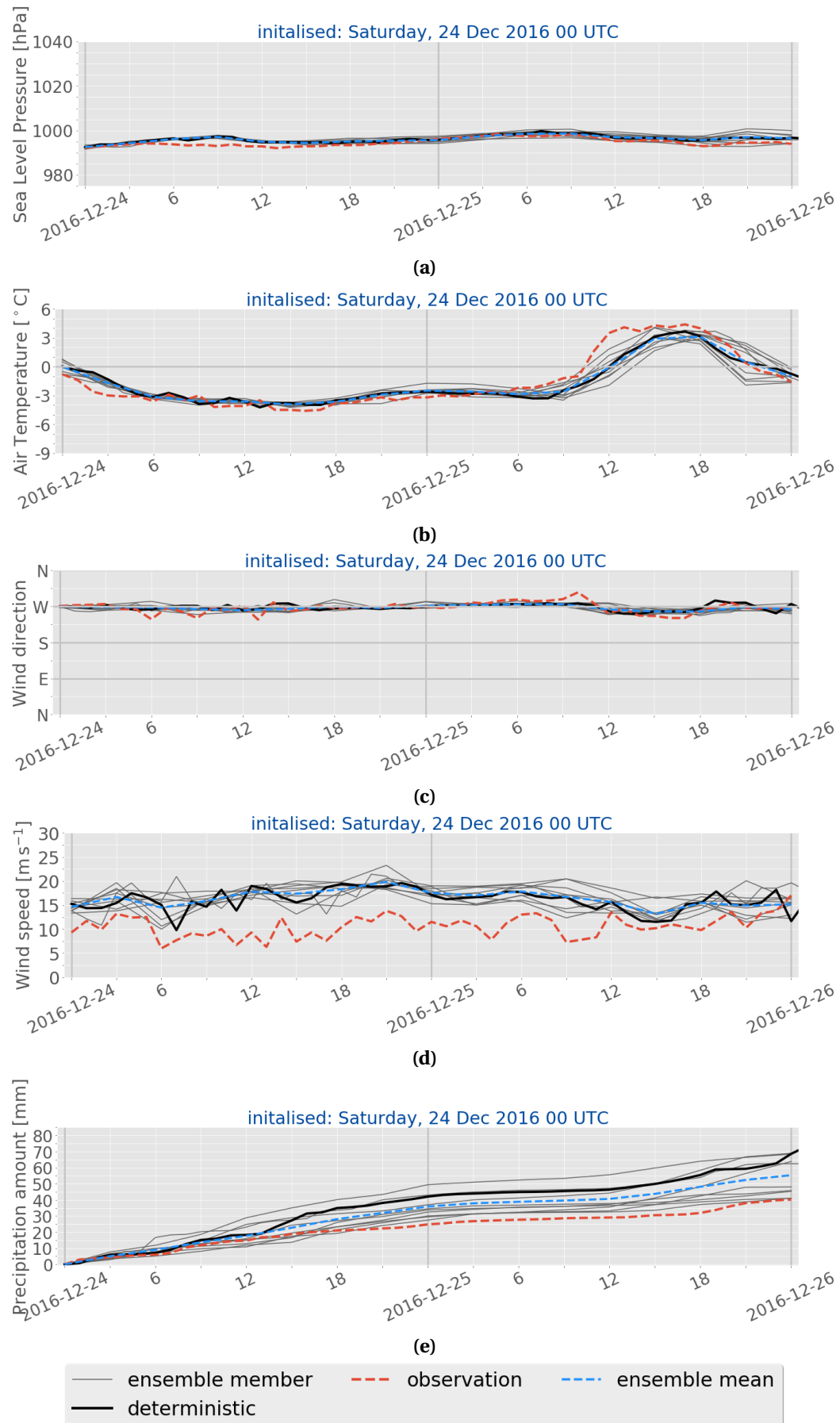


**Figure 4.1.4:** (As Figure 4.1.1.) Initialisation on 24 December 2016 at 0 UTC.

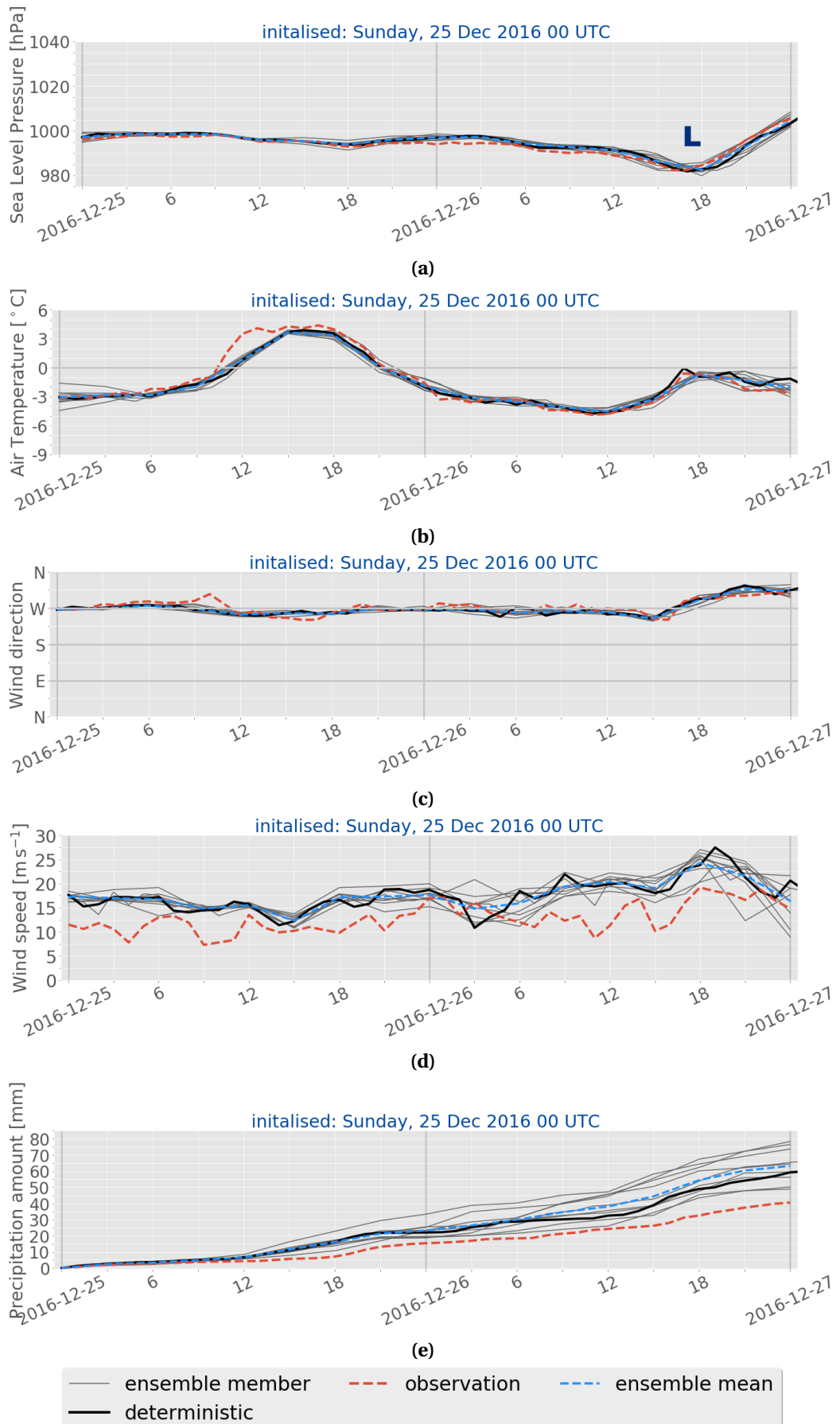


**Figure 4.1.5:** (As Figure 4.1.1.) Initialisation on 25 December 2016 at 0 UTC.

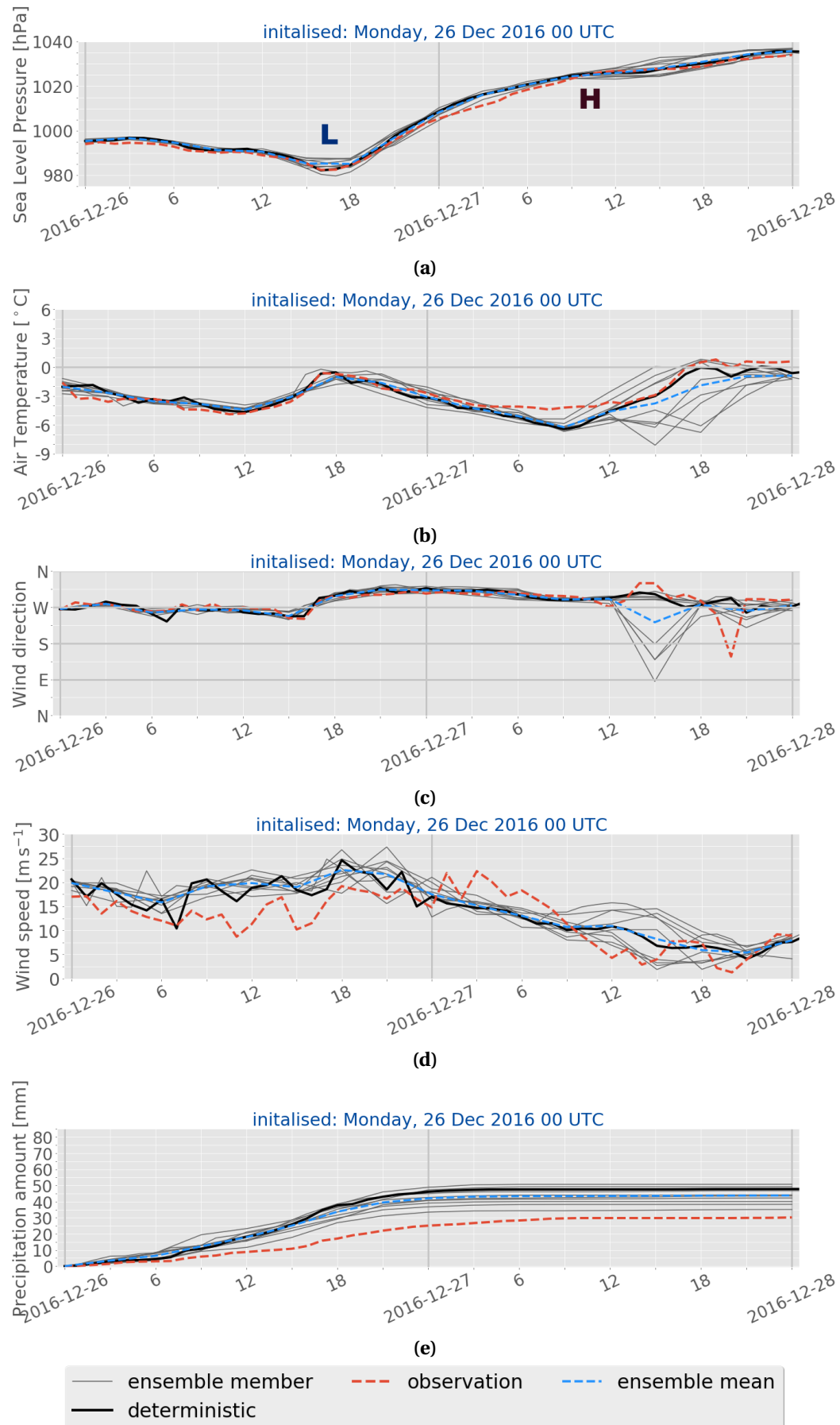


**Figure 4.1.6:** (As Figure 4.1.1.) Initialisation on 26 December 2016 at 0 UTC.

Similar patterns as on 23 December 2016 is seen for the evolution of the occluded front on 26 December 2016 in the ECMWF analysis Figure 3.5.7a and 3.5.7c. In this case the low-pressure system was located north of Møre and Romsdal in the Norwegian Sea. In the morning the cyclone is located east of Iceland and in the course of the day it moves closer to the coast of Norway (Figure 3.5.7b and 3.5.7d). Before landfall at 16 UTC, a pressure decrease occurs at Haukeliseter (Figure 4.1.6a). During the development of the occluded front, the pressure reaches its lowest point of 985 hPa (Figure 4.1.6a) and increases afterwards during the dissipation of the 2016 Christmas storm.

Since the cyclone was surrounded by colder air (south of the low-pressure system in Figure 3.5.7a), first a drop and then an increase of temperature were observed and forecasted by MEPS (Figure 4.1.6b). An indication of the occlusion evolution is also visible in the 10 m wind observations and MEPS predictions in Figure 4.1.6c and d. On 26 December 2016 at 0 UTC, the low pressure system is east of Iceland (not shown), moving closer into the Norwegian Sea by 12 UTC (Figure 3.5.7a and 3.5.7c). Surface westerly winds are associated to the cyclone in the Norwegian Sea, and impinging on the West coast of Norway Figure 3.5.7c. The 10 m wind measurement and MEPS forecast in Figure 4.1.6c and 4.1.6d, show a westerly gale of up to  $18 \text{ m s}^{-1}$  at Haukeliseter before 12 UTC. The centre of the occluded front is located over Norway at 18 UTC, and the pronounced surface pressure gradient, in Figure 3.5.7d, indicate an increase in surface wind with a north-west wind direction. During this transition of the occlusion, the wind direction changes to north-west with higher observed wind speeds up to  $20 \text{ m s}^{-1}$  (Figure 4.1.6c and 4.1.6d).

Throughout the day light to moderate precipitation is continuing until the occlusion passage is seen in Figure 4.1.6e. Heavy precipitation related to the occlusion, around 16 UTC, is followed by moderate to light precipitation on 26 December 2016.

On 23 December 2016 a cyclone is south of Iceland (Figure 3.5.4) and precipitation was associated to the transition of the occlusion. While 26 December 2016 precipitation was associated with the landfall of an occlusion. 25 December 2016 was marked by the transition of a warm sector. The ECMWF analysis shows a pronounced upper level ridge at the dynamic tropopause (Figure 3.5.6a). The cyclone core is south east of Iceland in Figure 3.5.6a with two associated frontal boundaries. While the warm front is approaching the west coast, the cold front is north-west of Great Britain. In Figure 3.5.6c, the tail of the cold front moved into lower latitudes, following the slowdown of the front, leading to a stationary frontal boundary. Furthermore, the mid-latitude jet is aligned with the surface frontal boundaries (Figure 3.5.6a), while the Haukeliseter site is located below the the midlatitudinal jet (Figure 3.5.6c).

Neither pressure nor wind observations and forecasts in Figure 4.1.5a, c, and d, indicate the evolution of any frontal boundary. The only indication of a transition could be seen in the increase and decrease of temperature afterwards at 11 UTC until 21 UTC (Figure 4.1.5b). In Figure 4.1.5c, a small wind direction change from west to north-west is observed by the wind mast at 10 UTC. This is not forecasted by MEPS, as it rather estimated strong westerly winds.

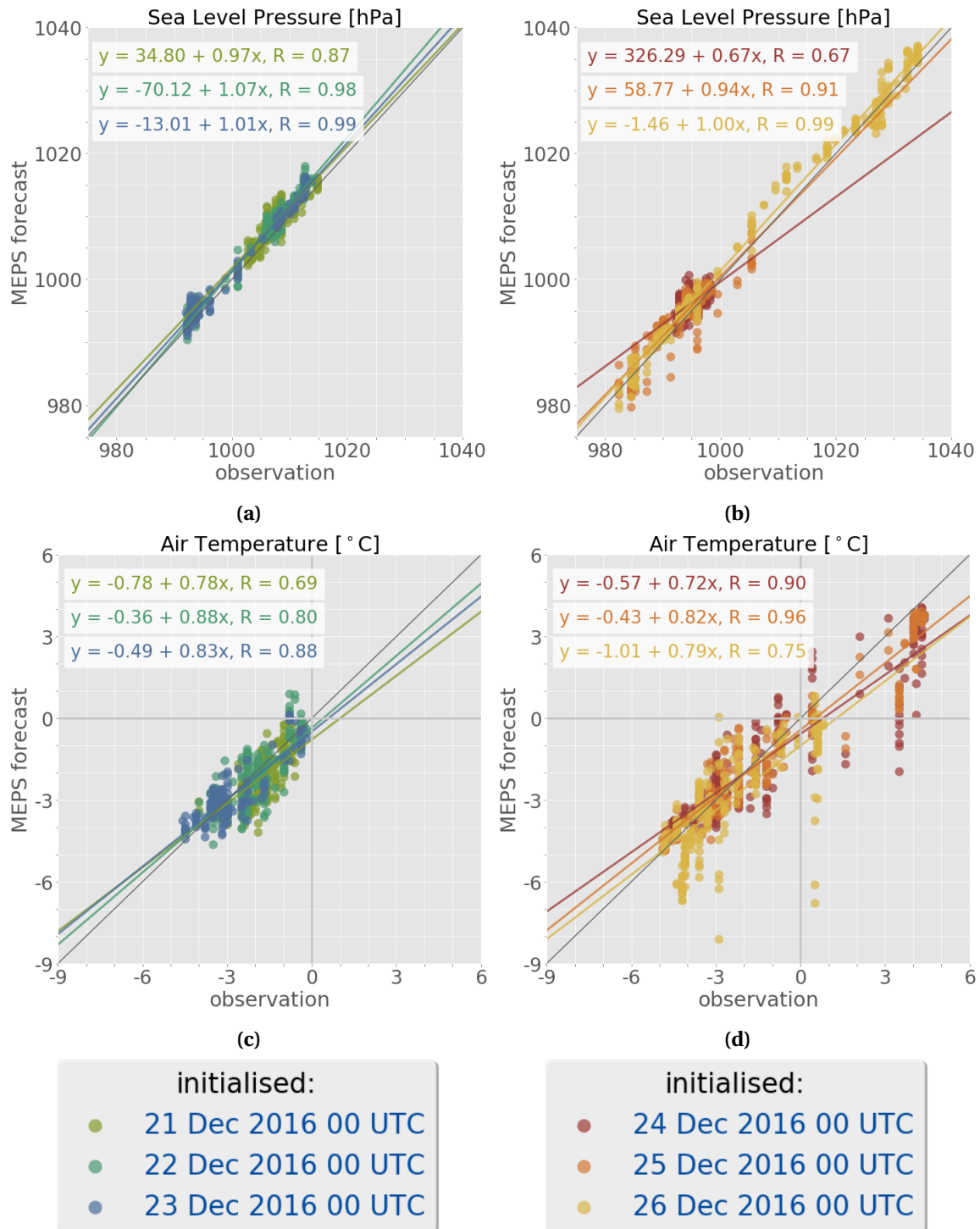


**Figure 4.1.7:** Scatter plots for sea level pressure and 2 m air temperature observations and ensemble forecasts initialised for 21 to 23 December 2016 (a, c) and for 24 to 26 December 2016 (b, to b) Meteorological observations are correlated with 48 h forecast values for each perturbed ensemble member The linear regression of all ensemble member for each individual day is presented together with the correlation coefficient  $R$ .

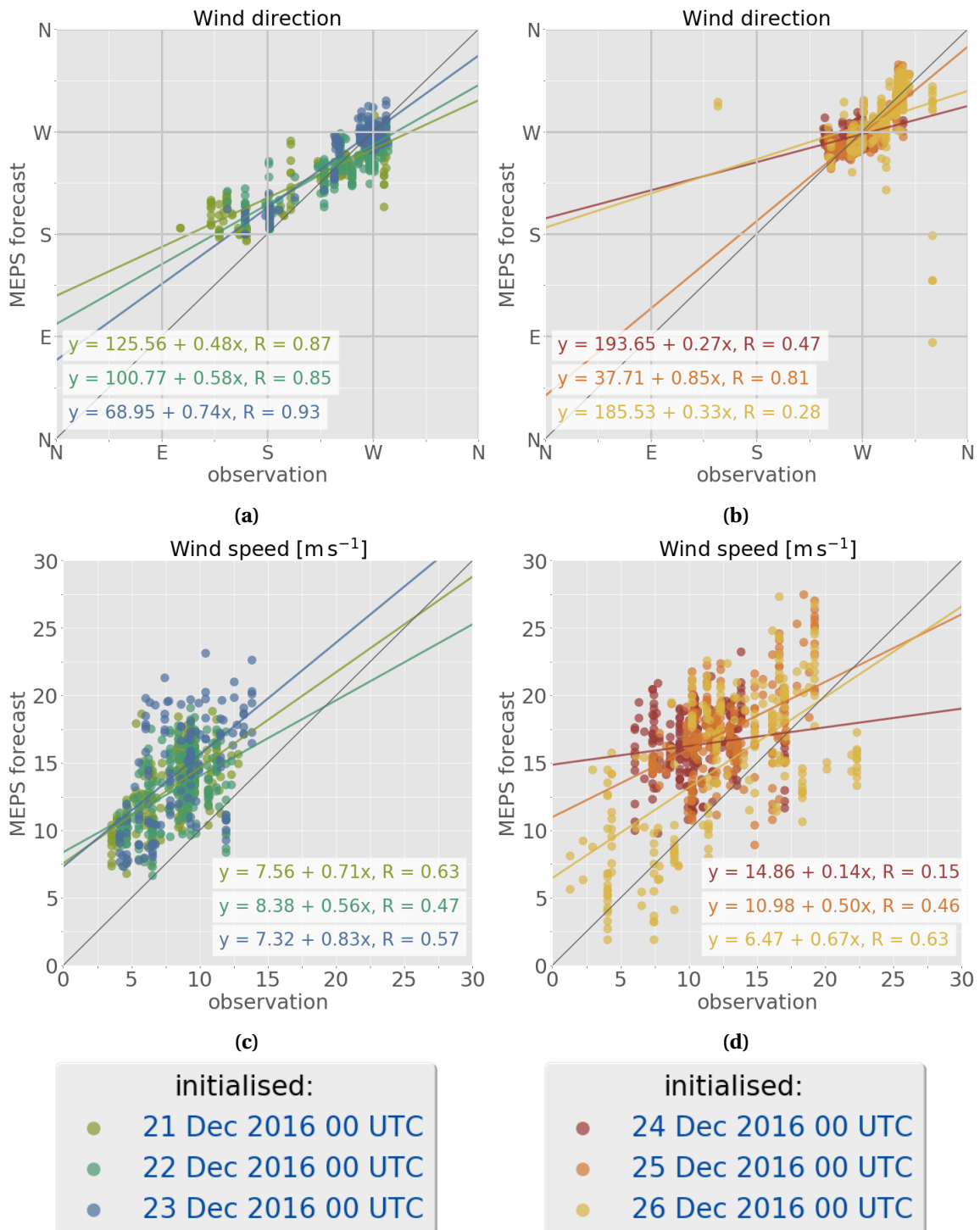


**Figure 4.1.8:** (As Figure 4.1.7.) From top to bottom: (a, b) 10 m wind direction, (a, b) 10 m wind speed.

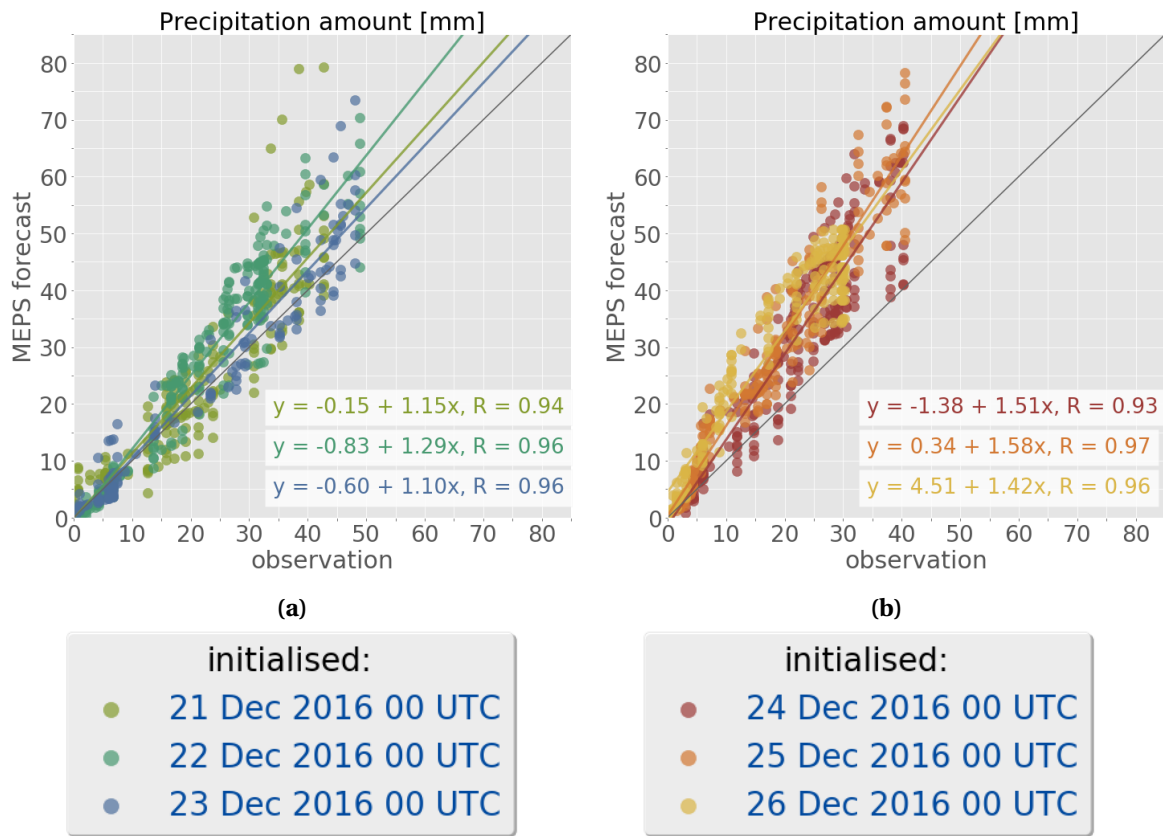


**Figure 4.1.9:** (As Figure 4.1.7.) (a, b) surface precipitation amount comparing double fence observations to 48 h MEPS forecasts.

Particle images taken by the MASC are available on 25 December 2016, during the transition of the warm sector in Figure 4.1.10. Without these images taken around 17 UTC it would only be possible to verify that liquid precipitation occurred with the optical precipitation detectors at the Haukeliseter site. Together with the increase in surface temperature (Figure 4.1.5b) it can be concluded that the warm sector of the Christmas 2016 event passed by the measurement site.

The comparison between the ECMWF analysis (Section 3.5) and the observations at the measurement site (Figures 4.1.1 to 4.1.6), allow to conclude that the ensemble member forecast system MEPS covers the prediction of large scale weather systems like occlusions and fronts, as well as liquid precipitation at the surface.

The scatter plots for observations and MEPS forecasts show good correlation for most variables (Figures 4.1.7 to 4.1.9). The best agreement for pressure is reached on 26 December 2016 (Figure 4.1.6a), when the Christmas storm hit land and dissipated after the evolution of the occlusion at 16 UTC. Dahlgren [2013] showed an improvement of sea level pressure forecast for AROME, by including large scale boundary conditions for ECMWF into the regional model. The observation-model comparison by Dahlgren [2013] showed a decrease of pressure bias with lead time after 24 h with the use of pressure mixing. Since surface pressure is in good agreement with the observations, it is assumed that the warm front did not pass through Haukeliseter on 25 December 2016 and only the warm sector associated with the 2016 Christmas storm is observed.

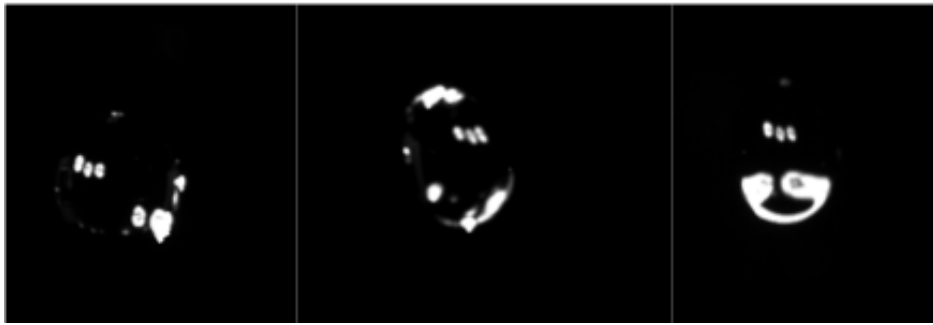


**Figure 4.1.10:** Multi-Angular Snowflake Camera images of falling water drops observed on 25 December 2016 approximately at 17 UTC from three different angles. Not all parts of the droplet are equally illuminated.

This shows a quite detailed forecast ability of MEPS, as from the ECMWF analysis, in Figure 3.5.6a, it is not quite clear if the warm front could have passed through. To be sure that the warm front did not pass through Haukeliseter, or whether it is a predictive error of MEPS, surface pressure, temperature and wind should be compared to the nearest grid point of the global forecast model ECMWF to verify this result.

Figure 4.1.7d displays a moderate correlation between observation and the 48 h MEPS ensemble member forecast system. In general, MEPS underestimates the observed 2 m air temperature, but MEPS estimated the temperature changes at the correct occurrence for 23, 25, and 26 December 2016.

This thesis uses only one extreme event during Christmas 2016 at Haukeliseter. Figure 4.1.11b shows warm and cold biases for 23 and 26 December 2016, respectively for Haukeliseter during the Christmas 2016 storm. On 25 December 2016, within the warm sector, a cold bias was observed, underestimating the temperature when compared to the observation. The forecasts for 23, 25, and 26 December 2016 show calculated mean absolute error values (Equation (2.7.5)) below 1 K in Figure 4.1.12b. In the verification report of Met-Norway MEPS deterministic forecast is verified against observations for December 2016 to February 2017 [Homleid and Tveten, 2016]. For December 2016 the 2 m air temperature had no bias within the Norwegian model domain. The Norwegian mean absolute error for 2 m air temperature was 1.6 K [Homleid and Tveten, 2016]. The mean absolute error for the Christmas 2016 storm is within the Norwegian December mean for the deterministic forecast. This does not necessarily show how well the forecast predicted the extreme event, since only one storm is studied at one site in Norway. The previous operational deterministic forecast model AROME-MetCoOp showed a cold bias of 2 m temperature for the Norwegian mean, during winter 2013 with the introduction of AROME-Norway and later AROME-MetCoOp [Müller et al., 2017]. The mean error for the Norwegian model domain of AROME-MetCoOP estimated by Müller et al. [2017] is smaller than 1.8 K for the surface 2 m air temperature in December 2014.

During the Christmas storm 2016 high wind speeds were observed at the Haukeliseter site (Figure 4.1.3d, 4.1.5d and 4.1.6d). According to Müller et al. [2017] high wind speeds are significantly better simulated for AROME-MetCoOp compared to ECMWF's forecast for the model domain. MEPS predictions of wind speed in Figure 4.1.3d, 4.1.5d, and 4.1.6d still display an

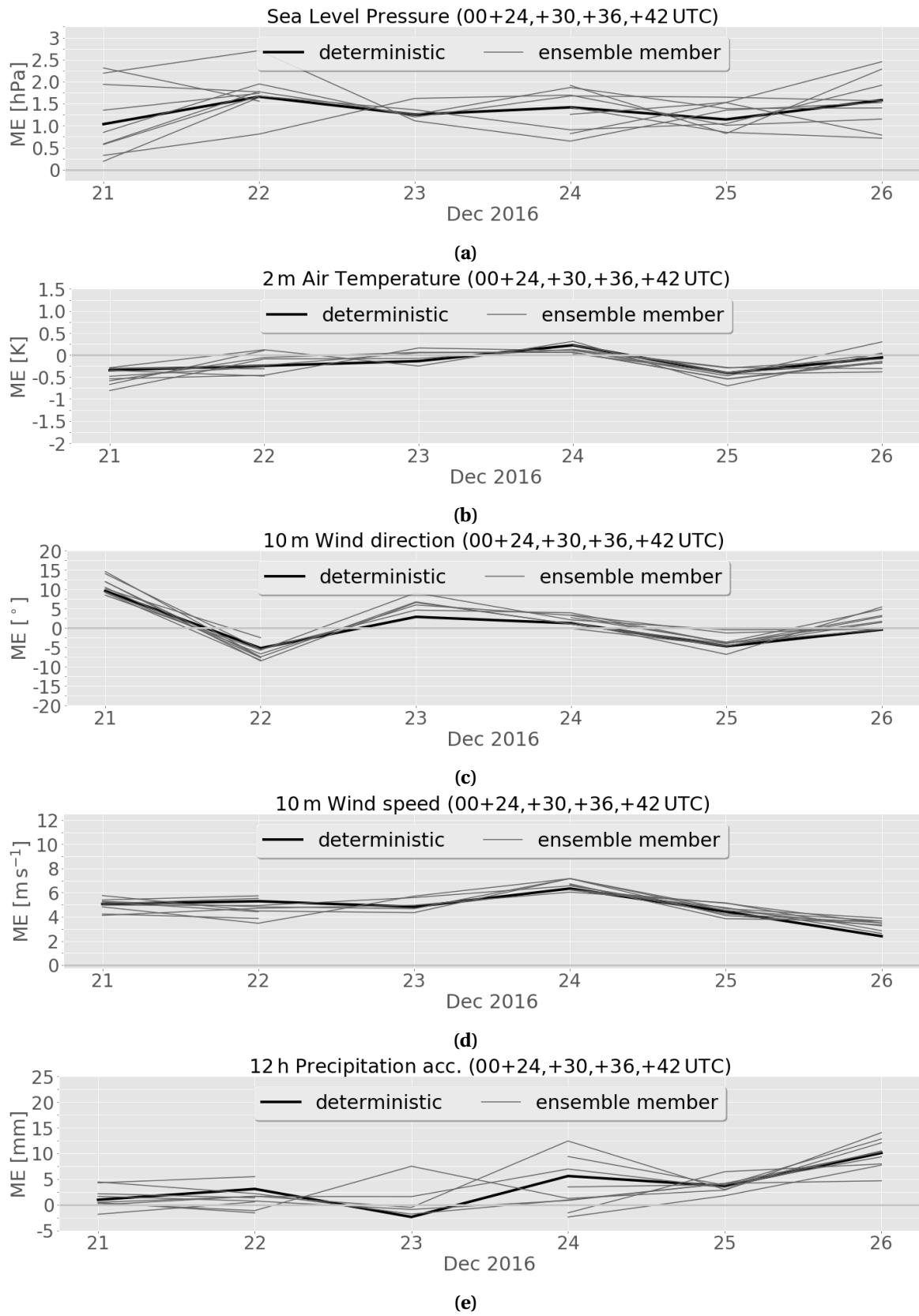


**Figure 4.1.11:** Mean error of surface variables for all ten ensemble members at Haukeliseter, initialisations at 0 UTC with lead times from 6 h to 24 h. From top to bottom, sea level pressure (a), 2 m air temperature (b), 10 m wind direction (c), 10 m wind speed (d), precipitation accumulation for 12 h surface accumulation (e).

overestimation of wind speeds throughout the event. Furthermore, the correlation of observations and wind speed in Figure 4.1.8c and d show an overestimation for stronger wind speeds on 24 to 26 December 2016 than for 21 to 23 December 2016. The mean error for wind speed during the Christmas storm is ranging from  $0 \text{ m s}^{-1}$  to  $7 \text{ m s}^{-1}$  for 48 h lead time (Figure 4.1.11d). During the extreme storm, the highest mean absolute error of  $10 \text{ m s}^{-1}$  occurs for initialisations on 24 December 2016 (Figure 4.1.12d).

The inaccuracy for wind speeds is an already known difficulty in the deterministic version of MEPS [Müller et al., 2017]. Müller et al. [2017] presented, that AROME-MetCoOp wind speed prediction generally agreed better with observations for wind speeds between  $3 \text{ m s}^{-1}$  to  $13 \text{ m s}^{-1}$  than ECMWF forecasts did, showing the advantage of a high-resolution weather model. Furthermore, with increasing wind speed the forecast accuracy for the Norwegian mean decreased with a mean absolute error below  $2 \text{ m s}^{-1}$  for 6 h to 24 h lead times, in December 2014 in AROME-MetCoOp. Müller et al. [2017] case study showed a slight underestimation of ECMWF 10 m wind compared to the Norwegian AROME-MetCoOp forecast for February 2015. On 24 December 2016, the mean absolute error is more than five times as high as the monthly averaged value for the Norwegian forecast domain ( $2 \text{ m s}^{-1}$  for 6 h to 24 h forecast time) from Müller et al. [2017]. In December 2016, the mean absolute error for the Norwegian mean of the deterministic forecast was  $2 \text{ m s}^{-1}$  [Homleid and Tveten, 2016]. The difference between the mean absolute error during the event and the monthly averages of Met-Norway, is firstly related to the comparison of a long term study of Müller et al. [2017]. Secondly to a month average mean absolute for the Norwegian model domain [Homleid and Tveten, 2016, Müller et al., 2017], and third to the location of Haukeliseter (orographic effect, Section 4.2.5).

Haukeliseter is a measurement site exposed to high wind speeds [Wolff et al., 2013, 2015]. The ensemble prediction system MEPS seems to still have issues forecasting the wind speed correctly in mountainous terrain. A detailed insight to the orographical wind influence will be discussed in Section 4.2.5.

Pressure, temperature, and wind changes for the occlusion transition on 26 December 2016 were already forecasted for initialisations on 25 December 2016 (Figure 4.1.5), only wind speed and precipitation seem not to agree with the observations at Haukeliseter. The same is true for 25 December 2016, when the warm sector passes through Haukeliseter.

Figures 4.1.1 to 4.1.6e illustrate the surface precipitation amount observed and predicted by MEPS for Haukeliseter. MEPS overestimation is shown for precipitation when the cyclone intensifies and gets closer to Norway on 24, 25 and 26 December 2016. The surface observations and MEPS predictions in Figure 4.1.9a and b show an overestimate for 24, 25 and 26 December 2016, whereas on 21, 22, and 23 December 2016 the surface accumulation is balanced for predictions up to 30 mm. Any reasons for the overestimation of precipitation accumulation on the ground will be further analysed and discussed in Section 4.2.3.

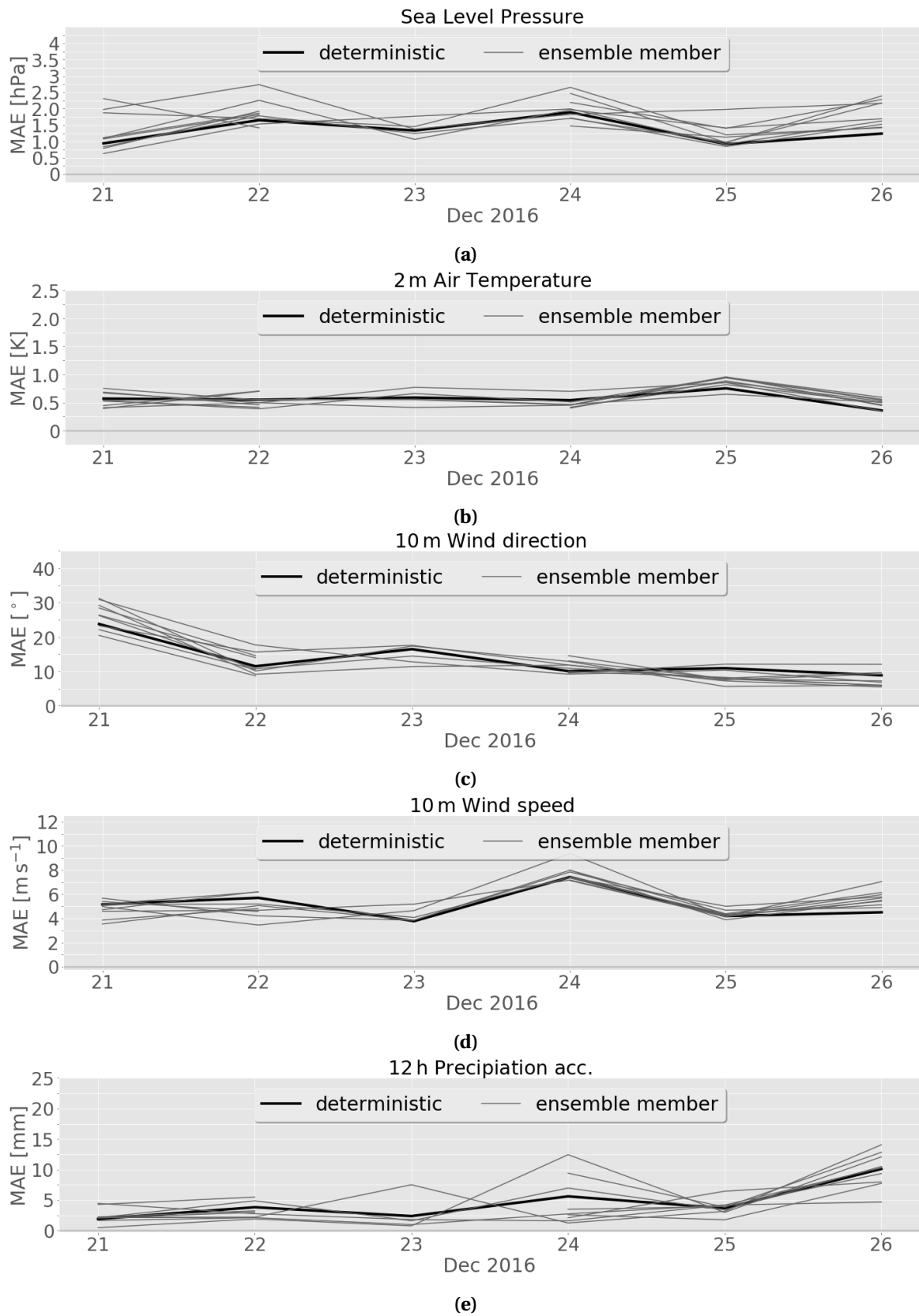


**Figure 4.1.12:** Mean absolute error (a, b, c, d, e) of surface variables for all ten ensemble members at Haukeliseter, initialisations at 0 UTC, valid for 48 h. From top to bottom, sea level pressure (a), 2 m air temperature (b), 10 m wind direction (c), 10 m wind speed (d), precipitation accumulation for 12 h surface accumulation (e).

Overall, for initialisations on 21 to 23 December 2016 (Figures 4.1.7 to 4.1.9) the forecast is best for all variables. The large-scale weather pattern seems to be more predictable as long as the weather situation is not extreme. The correlations for the forecasts between 24 and 26 December 2016 (Figures 4.1.7 to 4.1.9) suggest as MEPS may have difficulties predicting the intensification and associated pressure decrease of the Christmas 2016 storm at Haukeliseter. The prediction of pressure fits well on all days (Figure 4.1.7a, b) compared to temperature (Figure 4.1.7c, d), wind direction (Figure 4.1.8a, b), wind speed (Figure 4.1.8c, d), and precipitation (Figure 4.1.9a, b). The greatest difficulty MEPS has, is with the prediction of wind speed during the entire extreme event. The rainfall, however, fit well for 23 December 2016 (Figure 4.1.3e and 4.1.9a), but MEPS has problems predicting the accumulation of surface precipitation amount correctly for the extreme days of the 2016 Christmas storm, 24 to 26 December 2016 (Figure 4.1.5e, 4.1.6e, and 4.1.9b).

Figure 4.1.11a, b have shown good agreement of ensemble member forecasts with a small bias. It is not expected that ensemble members agree they should just give a variability around the observations, that is why ensemble member prediction exists. Based on the uncertainty in observations the solution space that is possible has to be understood (Section 2.5). The model is not adjusted to present the extreme event particularly well as it is adjusted to span the full climatological range. For large weather situations which are considered as normal the observations have to be within the spread of the ensemble members [Owens and Hewson, 2018]. Because of the nature representing the climatology, ensemble members will either over- or under-estimate the risk of anomalous or extreme weather events.

The extraction of an extreme weather event from an ensemble system is not always straightforward. For example, 30 mm precipitation during one day in December would not be extreme at the Norwegian West Coast, but would be at Haukeliseter during December.

## 4.2 SNOW

After the analysis of meteorological quantities, the snow at Haukeliseter during the Christmas storm will be investigated.

First the results from the optimal estimation retrieval scheme will be examined and compared to the observations of the double fence. After the overestimation of surface accumulation will be analysed, followed by a vertical comparison of observed estimates of snow water content and predictions. The sections finishes with the relation between wind and precipitation related to the surrounding topography at Haukeliseter.

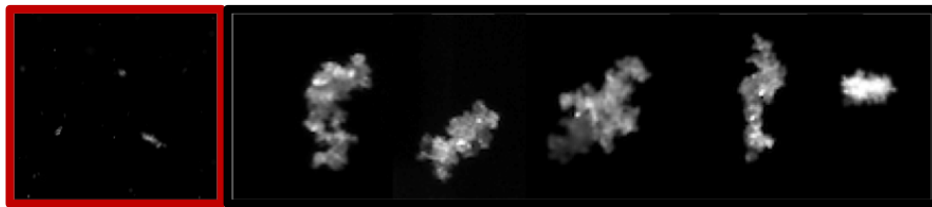


**Figure 4.2.1:** Particle images of small ground-up blowing snow (red frame) and rimed aggregates (five images to the right). Images taken at different occasions during the Christmas storm 2016 with the Multi-Angular Snowflake Camera.

#### 4.2.1 SENSITIVITY OF THE OPTIMAL ESTIMATION RETRIEVAL

The optimal estimation retrieval scheme for snow was applied to the six-day Christmas 2016 storm event. MASC images of snow particles during the event were used to guide the selection of the appropriate particle model and PSD input for the retrieval scheme. In this section, the sensitivity of retrieval results to these inputs is explored for the 22 December 2016 as an example. This day is used as an example day because it showed the smallest difference between double fence gauge and retrieved surface amount (Section 4.2.2) during the 2016 Christmas event. Such an exercise should also allow an identification of those properties that yield the best match with Met-Norway snow gauge measurements at Haukeliseter.

The majority of the MASC images from Haukeliseter contained snow particles that looked like the left image Figure 4.2.1 (red frame). Such images suggest small ground-up blowing snow particles that are consistent with the high winds observed during the event. However, a careful examination of the MASC images finds the presence of rimed aggregates such as those in the right five images (Figure 4.2.1). Pristine crystals such as plates and columns were not observed during the Christmas 2016 event. As such, the use of two different aggregate particle models developed for the CloudSat mission are further investigate (Figure 4.2.1).

Figure 4.2.2 presents hourly measured surface precipitation amounts on 22 December 2016 plotted against retrieved values for the two different aggregate assumptions. The 'B8' aggregate is a low reflectivity per unit mass aggregate that worked well for the cold, dry conditions observed at Barrow as described in Cooper et al. [2017]. The 'B6' aggregate, presented in Appendix A.1, is a high reflectivity per unit mass particle (Section 2.4.1). As such, the 'B6' aggregate would seem more physically consistent with the observed rimed particles (Figure 4.2.1, 5 aggregates to the right) and humid environment found in the coastal mountains at Haukeliseter. The presence of a water or rimed coating on the aggregates aloft would greatly enhance their effective reflectivity.

Indeed, Figure 4.2.2 suggests that the reflective 'B6' aggregate agree much better than the less reflective 'B8' aggregate with the snow gauge. During the Christmas storm 2016 the assumption of the 'B8' aggregate shows overestimation of precipitation amount at the ground compared to the double fence gauge for all six-days.

Table 4.2.1 presents the percentage differences between snow gauge and retrieved estimates found when using these particle model assumptions for 22 December 2016. Use of the 'B6' aggregate agreed within 5 % of the double fence observations (Table 4.2.1) for both 12 h and 24 h surface

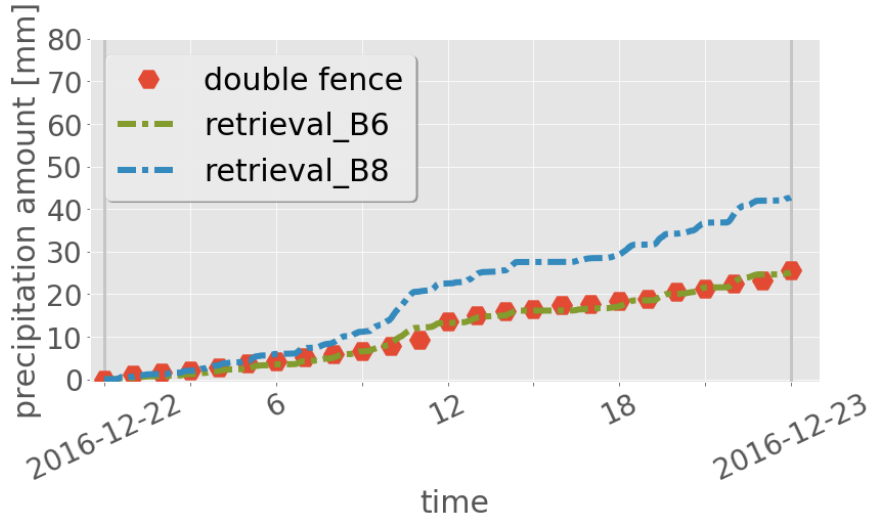


**Figure 4.2.2:** Hourly double fence surface precipitation accumulations [mm] plotted against retrieved values for 22 December 2016 for different retrieval assumptions permutations. Double fence precipitation accumulation, as red hexagons, retrieved precipitation amount for the here used study ('B6'), green, dash-dotted, and for small aggregates ('B8'), blue dashed.

accumulations. Admittedly, use of the 'B6' aggregate produced slightly too little snow amount relative to the gauges for the remaining days of the event as discussed in Section 4.2.2. The use of the 'B8' aggregate, however, overestimates accumulated snow by at least 65 % for both the 12 h and 24 h surface accumulations (Table 4.2.1). Since this aggregate had low reflectivity per unit mass, it required significantly more SWC in the forward model calculations (Section 2.4.1) to match MRR reflectivities. The retrieval therefore overestimates snowfall rate for these meteorological conditions at Haukeliseter during the Christmas 2016 storm.

The sensitivity study here has focused on MASC estimates of habit instead of particle size distribution or fall speed. The reason is that MASC and PIP primarily detected blowing snow particles at the surface that likely were much smaller than the particles that the MRR remotely sensed aloft. The use of the PSD measured by the MASC or PIP in the retrieval therefore produced much larger surface precipitation amount than those measured by the double fence snow gauges, e.g. on 22 December 2016 (Figure 4.2.2). Essentially, it takes a much greater mass of small particles than large particles to match a given reflectivity. The results during the Christmas 2016 event contrast with those found for low wind speed events at Haukeliseter where the use of MASC habit, PSD, and fall speed observations resulted in retrieved snow accumulations very close to Met-Norway double fence gauge observations. Regardless, for this high wind event, the a priori temperature PSD relationship by Wood [2011] and a climatological average fall speed of  $0.85 \text{ m s}^{-1}$  [personal communication, Schirle, 2018] were employed.

'B6' rimed aggregate assumption resulted in a better agreement than the 'B8' pristine assumption for surface accumulation during the Christmas 2016 storm. Therefore, the difference between the retrieved precipitation amount at the ground and the double fence gauge observations will be further studied in the following section.

**Table 4.2.1:** Observations by the double fence gauge (obs.) and retrieved snow amounts (ret.) for 22 December 2016 for different particle model assumptions. B6 is the rimed aggregate assumption used in this thesis (Section 2.4.1) and B8 the assumption for small particles as used in the CloudSat optimal estimation snowfall retrieval.

Particle model	12 h accumulation			24 h accumulation		
	Amount		Difference	Amount		Difference
	obs.	ret.		obs.	ret.	
	[mm]		[%]	[mm]		[%]
B6	13.6	13.2	-3.0	23.1	25.1	-2.1
B8	13.6	22.5	+65.5	23.1	42.7	+66.9

#### 4.2.2 SURFACE OBSERVATIONS

To be able to compare the vertical predicted snow water content with the retrieved snow water content a verification of the surface accumulation is made. If the retrieved surface accumulation is reliable in comparison to the double fence measurement, then the vertical measurements can be trusted.

The correlation in Figure 4.2.3a demonstrates a good agreement between the 48 h accumulation measured by the double fence and the retrieved surface accumulation. The black line in Figure 4.2.3a presents a linear correlation with a regression coefficient of  $R = 0.97$ . In general, the retrieved surface precipitation accumulation is underestimated when compared to the double fence measurements, but not to a large degree.

Figure 4.2.3b shows the difference between retrieved accumulation and observed accumulation by the double fence. For the time period 21 to 24 December 2016, Figure 4.2.3b indicates an underestimation of retrieved snow accumulation of less than  $-5$  mm for the first 24 h. Snow accumulation calculated on 23 December 2016 at 0 UTC show after 24 h an underestimation by the retrieval of up to  $-6.5$  mm. On 24 December 2016, larger underestimation after 43 h is related to the observation of liquid precipitation on 25 December 2016 between 12 UTC to 21 UTC. On 25 December 2016 no fair comparison to the double fence measurement can be performed after 12 UTC because of the neglection of liquid precipitation when temperatures exceed  $2^{\circ}\text{C}$ .

For the Christmas storm (21 to 26 December 2016) an average difference of 85.5 % is calculated for 12 h surface accumulation (Table 4.2.2). For longer, 24 h accumulation the average difference decreases to  $-4.7$  % (excluding values on 25 December 2016 after 12 UTC and on 26 December 2016 after 17 UTC because of attenuation at the MRR). The daily surface precipitation amount difference between retrieval and observation in Table 4.2.2 show almost always a well agreement to the double fence. The only well pronounced mismatch is seen on 21 December 2016, where it measures much more than the double fence gauge (+435.8 %).

Similar to this study, Cooper et al. [2017] used a CloudSat snow particle model, PSD and fall speed from MASC observations for five snow events at Barrow, Alaska. The comparison to the weather station revealed a difference between National Weather Service observations and retrieved accumulations of  $-18$  % for five snow events.

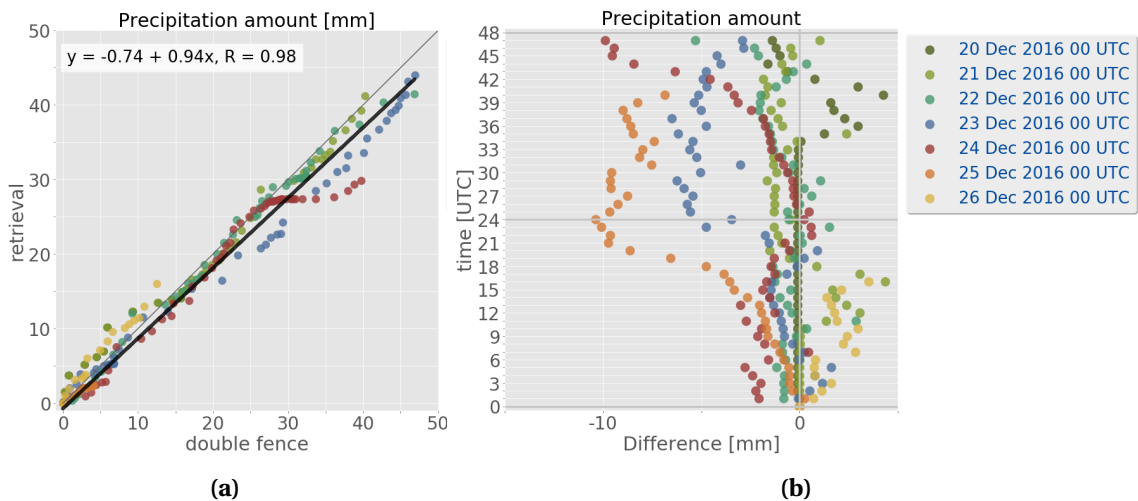


**Figure 4.2.3:** a: Surface precipitation amount comparison between the double fence observations and the retrieved surface accumulation of precipitation for 48 h. In black: the linear correlation between the double fence observations and retrieved surface snow. b: Difference between the retrieved and the observed accumulation by the double fence. The colours represent the different starting days at 0 UTC for the 48 h accumulation.

Table 4.2.2 shows the difference for each individual day and the average difference for six and four days, depending on the accumulation of 12 h or 24 h. The choice of the correct PSD model, slope parameters and fall speed in the optimal estimation snowfall retrieval, shows a good agreement with the observations at Haukeliseter for the 2016 Christmas storm in contrast to the 200 % difference when only using the CloudSat snowfall algorithm (Section 2.4). It also indicates a reduction of the non-uniqueness of snow accumulation is reduced, when using a combination of ground-based observations instead of only Ze-S relationships.

It turns out that there is no relation between high and low precipitation events since the differences vary daily. Cooper et al. [2017] also showed different combinations of PSD assumptions and snow fall speed. For Barrow, best agreements between observations and retrieved snow accumulation were found by using the CloudSat particle model, slope parameters and snowfall speeds from the MASC. In the here presented study, the best assumption for surface snow accumulation was found by using a particle model for rimed aggregates (Section 2.4 and 4.2.1) such as in Figure 4.2.1.

On 21 December 2016, the deviation is large (435.8 %). This is probably related to an observation of precipitation at the double fence, while the MRR did not observe precipitation. On 21 December 2016, observation at the double fence might be related to some particles stirred up by wind into the orifice of the gauge. Since no manual observations are done at the Haukeliseter site, is it difficult to say if blowing snow occurred or if it was snowing. This introduces additional errors on the double fence measurements. From the vertical MRR reflectivity, in Section 4.2.4, Figure 4.2.7, it can be seen, that precipitation was not observed on 21 December 2016 before 9 UTC. Even though it is assumed that the double fence is the correct measurement, there are still some uncertainties, such as under-catch during high wind speeds [Wolff, unpublished]. A better way to examine the accuracy of the retrieved surface precipitation accumulation could be to compare the results to measurements inside a bush gauge.

Wolff, [unpublished] estimates the under-catchment of double fence gauge compared to bush

**Table 4.2.2:** Comparison of observed (obs.) and retrieved (ret.) snow amounts for the Christmas storm 2016. Difference refers to the difference of the retrieved and observed snow accumulation after 12 h and 24 h. The average difference is the value over all six/four days. Excluding values after 12 UTC on 25 December 2016 and after 17 UTC on 26 December 2016.

Day in 2016	12 h accumulation			24 h accumulation			
	Amount		Difference	Average difference	Amount		Average difference
	obs.	ret.			obs.	ret.	
	[mm]	[%]	[%]	-2.1	[mm]	[%]	[%]
21 Dec	0.7	3.8	+435.8		17.1	16.6	-2.7
22 Dec	13.6	13.2	-3.0		25.6	25.1	-2.1
23 Dec	6.3	5.2	-16.8		23.3	19.8	-14.9
24 Dec	14.7	13.4	-8.6		24.8	25.0	+0.8
25 Dec	4.3	-	-		+15.4	-	-
26 Dec	8.8	10.6	+20.1		25.1	-	-

gauge measurements to 10 %, for outside winds of  $9 \text{ m s}^{-1}$  (Section 2.3.1). If the double fence gauge underestimate frozen precipitation under high wind condition, would follow that the optimal estimation retrieval results are more than 20 % too low to the true state.

During the Christmas 2016 event the average difference is low for 24 h surface accumulation (-4.7 %) in Table 4.2.2. At Barrow, Alaska, the best average difference between retrieved and observed surface accumulation was 36 % [Cooper et al., 2017]. This leads to a very good agreement between observed and retrieved snow accumulation during 21 to 24 December 2016. In Section 4.2.4, the vertical SWC will be compared to the forecasted MEPS values for the 2016 Christmas storm. Despite the under-catchment of snow in high wind speeds, the double fence measurement give trust for the retrieved profiles of snow water content. While snow water content is compared to the MEPS forecast, it should be kept in mind that retrieved snow accumulation is underestimated and therefore the vertical SWC may be too low.

#### 4.2.3 SURFACE OBSERVATION AND MEPS

Hereafter, MEPS surface precipitation prediction forecast is compared to the double fence gauge observations at Haukeliseter to see if observed surface accumulation was correctly predicted by MEPS.

Figure 4.2.4 and 4.2.5 shows surface accumulation observations at the double fence, retrieved snow accumulation, and MEPS forecast for 48 h. The blue dashed line shows the ensemble mean of all ten members. The ensemble mean of precipitation amount is calculated every three hours, due to the three hourly time resolution of most of the perturbed member (Section 2.7). When not all perturbed member forecast data was available from the Norwegian Meteorological Institute [2016], like on 23 December 2016 (Figure 4.2.4c), no ensemble mean is calculated. At the bottom of Figure 4.2.4 and 4.2.5 the associated 10 min average wind of the last hour from the 10 m weather mast at Haukeliseter is presented. This will help to see if surface precipitation observations by the double fence may be influenced by wind.

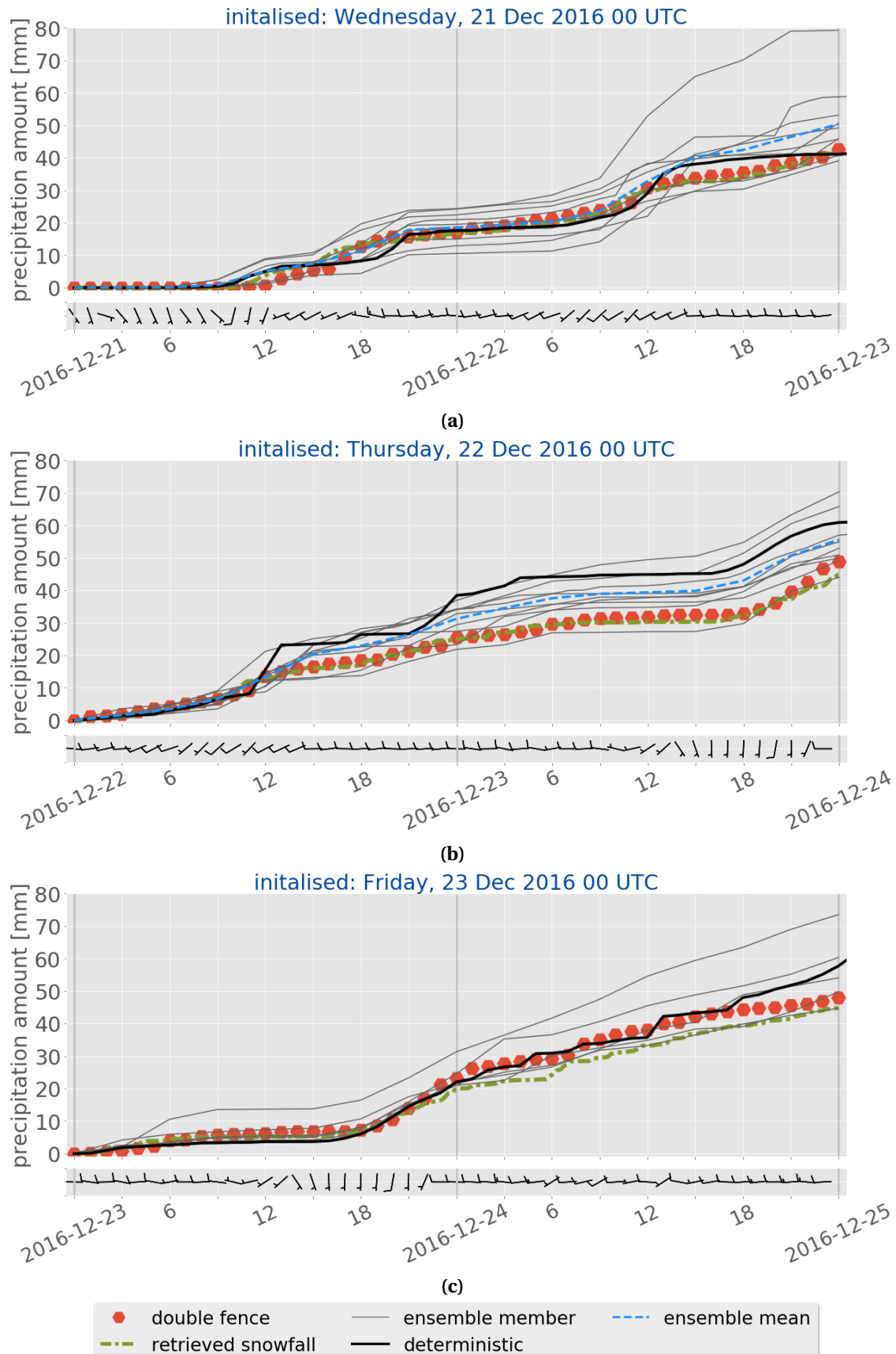


**Figure 4.2.4:** 48 h surface precipitation accumulation for 21 to 23 December 2016. Representing the values from the double fence in red, hexagons; optimal estimation retrieval output at the first noise free level in dash-dotted green; MEPS ensemble member deterministic forecast, initialised at 0 UTC in black and its nine perturbed ensemble members in grey. The ensemble mean of all ten members is shown in dashed blue. Underneath is the associated last hour 10 min average wind from the weather mast at 10 m height.

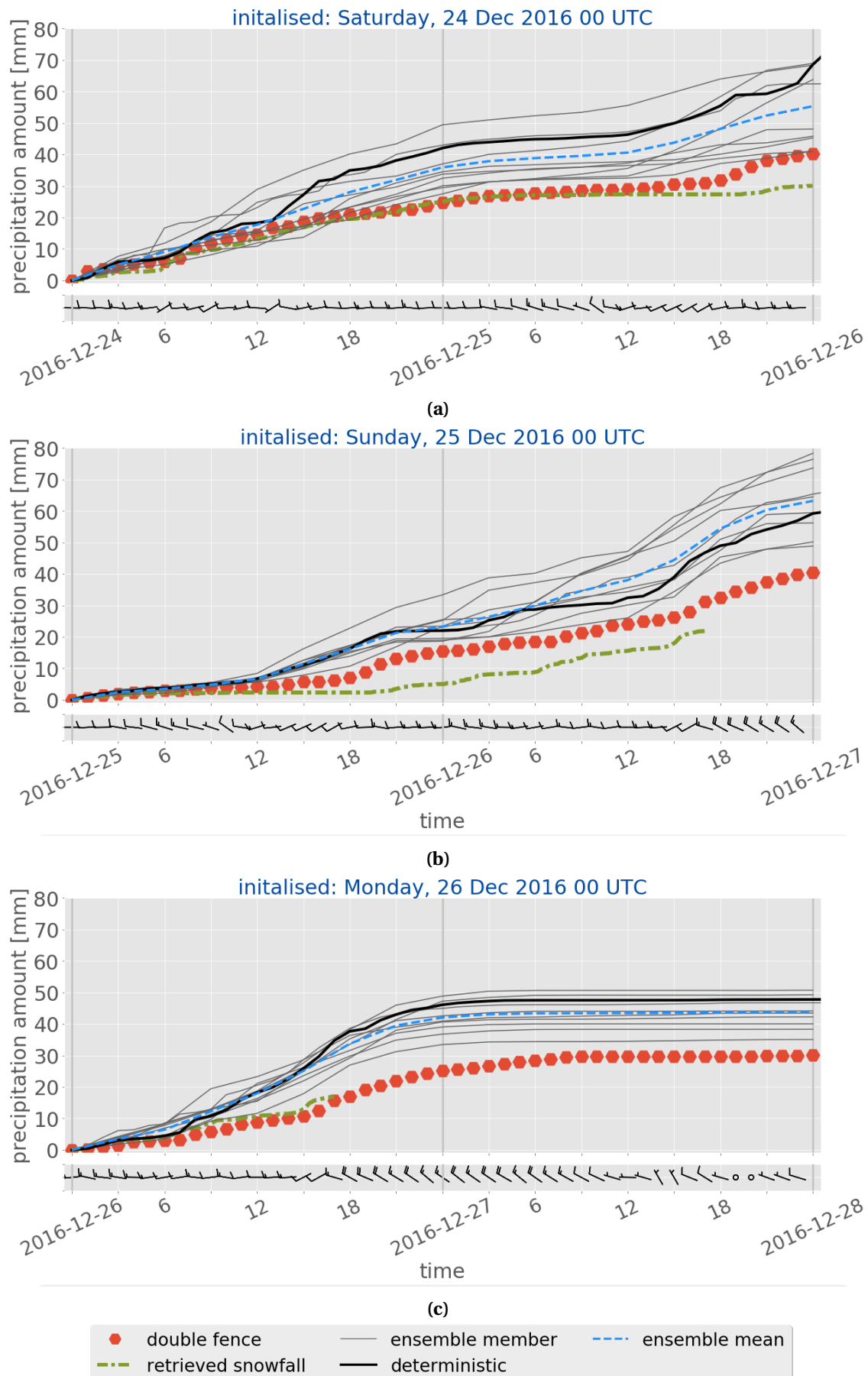


**Figure 4.2.5:** (As Figure 4.2.4.) Initialisations on 24, 25, and 26 December 2016 at 0 UTC.

MEPS surface accumulation does not account for under-catchment by too high wind speeds, and therefore are not presented in Figure 4.2.4 and 4.2.5. In general, Figures 4.2.4a to 4.2.4c show a better agreement between double fence precipitation amount observations and forecast for 48 h forecasts initialised on 21 to 23 December 2016 at 0 UTC than for initialisations on 24 to 26 December 2016. The double fence observation lie for 21, 22, and 23 December 2016 within the spread of the ensemble members (Figures 4.2.4a to 4.2.4c), covering the uncertainty within the measurements (Section 2.5). On the other hand, observations between 24 and 26 December 2016 are too low compared to the ensemble spread (Figures 4.2.5a to 4.2.5c). During 24 and 26 December 2016, the low-pressure system intensifies and gets closer to the Norwegian coast, influencing the local weather in Norway (Section 3.5). Figure 4.2.5a to c indicate a larger estimated surface precipitation amount for all ten ensemble members compared to observed values at the measurement site between 24 to 26 December 2016. Furthermore, all ensemble members seem to overestimate the surface accumulation after 18 h on 24 December 2016 and after 12 h on 25 and 26 December 2016. The correlation for precipitation between 48 h double fence observation and ensemble precipitation forecast is presented in Figure 4.1.9a and b. Showing a better agreement for 21 to 23 December 2016 than initialisation on 24 to 26 December 2016. On 21 to 23 December 2016 the slope of the regression line is relatively close to unity.

Initialisations on 24 December 2016 (Figure 4.2.5a) indicate an overestimation of the deterministic surface snow amount prediction already after 13 h forecast time. The deterministic forecast in solid black in Figure 4.2.5a is much higher and increases faster than the observations and the nine perturbed members. In Figure 4.2.5a at 16 UTC, a difference of approximately 15 mm can be seen when compared to the surface measurements. This difference remains almost constant over the forecast time.

While the cyclone propagates closer to Norway, the forecast error of the surface precipitation increases. Overestimation occurs around 12 UTC on 25 December 2016. This overestimation of the precipitation amount could be associated with the warm sector evolution at Haukeliseter (Section 4.1). Afterwards, with increasing lead time MEPS forecasts show the same simulated precipitation development as the double fence, but too high. The precipitation is light between 12 UTC and 18 UTC which shows as an almost constant surface precipitation amount. At 18 UTC the surface precipitation amount at the double fence increases and so does the MEPS forecast.

An overestimation of the surface precipitation is also simulated on 26 December 2016. While the surface analysis indicates the passage of an occlusion after 15 UTC (Figure 3.5.7a, 3.5.7c, and Section 4.1). The overestimation seems to occur after a 12 h lead time in Figure 4.2.5c. The MEPS ensemble seems to predict the timing of precipitation correctly compared to the double fence, but estimates a too high surface accumulation. Table 4.2.3 shows the difference between the observations and ensemble mean MEPS forecast for 12 h and 24 h accumulation. Generally the forecast accuracy decreases with lead time which can be seen on the larger deviation between the ensemble member after 18 h lead time (Figure 4.2.4, 4.2.5). As seen in Table 4.2.3, the average difference decreases with longer forecast time. For 21 to 26 December 2016 the deviation is +134.7 %. For longer lead times, 24 h, the average difference is reduced to +32.6 %. Due to the good forecast between 21 to 23 December 2016 ( $\leq 11\%$ ) the averaged difference is smaller.

**Table 4.2.3:** Observations (obs.) and forecasted (MEPS) surface precipitation amounts for the Christmas storm 2016. Difference refers to the percentage difference between MEPS ensemble members and the double fence observation, averaged over all ensemble member for 12 h and 24 h. The average difference is the value over all days.

Day in 2016	12 h accumulation					24 h accumulation						
	Amount		Difference	Average difference	Amount		Difference	Average difference				
	obs.	MEPS			obs.	MEPS						
	[mm]		[%]		[mm]		[%]		[%]			
21 Dec	0.7	5.1	+626.1		17.1	18.5	+8.3					
22 Dec	13.6	13.4	-1.6	+1.3	25.6	31.3	+22.2	+32.6	+10.8			
23 Dec	6.3	6.6	+4.2		23.3	23.7	+1.8					
24 Dec	14.7	17.7	+20.4		24.8	35.9	+44.8					
25 Dec	4.3	6.7	+55.1	+59.8	15.4	23.3	+50.8	+54.4				
26 Dec	8.8	17.9	+104.0		25.1	42.1	+67.5					

On 21 December 2016 very large deviation (626.1 %) is shown. AROME-MetCoOp had problems with too low precipitation. The deviation between observed and forecasted values was larger if the precipitation amount is less than 10 mm [Müller et al., 2017]. At Haukeliseter, low precipitation amount is observed (0.7 mm) on 21 December 2016. The daily percent difference show to be high for the last three days of the 2016 Christmas extreme event.

The largest overestimation of MEPS forecast for precipitation amount is seen in Table 4.2.3 on 26 December 2016 with +104 % for 12 h. This shows the highest overestimation for the three days (24 to 26 December 2016).

In Figure 4.1.11 show the ensemble member a balanced bias from 21 to 23 December 2016. The bias for 24 to 26 December 2016 is wet, also showing the overestimation of surface accumulation. In Figure 4.1.12e, the mean absolute error is less than 7 mm for 21 to 23 December 2016 and increases with intensification of the storm up to 14 mm on 26 December 2016. The mean absolute error in Figure 4.1.12e for 12 h precipitation is less than 7 mm on 25 December 2016, similar to 21 to 23 December 2016.

Since MEPS performance was better on 21 to 23 December 2016 one might assume that the double fence measurement is influenced by surface winds. A relation between high wind and double fence observation could be possible. Table 4.2.4 presents the percentage difference between the double fence and MEPS forecasts under the condition that the double fence is affected by wind with a catch-ratio less than 10 %. Here, it also shows an increase in forecast accuracy for precipitation accumulation over 24 h. The average difference is reduced by 23.5 % for 12 h accumulation. Assuming an accumulation underestimation of 10 % would lead to a reduction of overestimation to 43.8 % for 12 h during 24 to 26 December 2016 (Table 4.2.4). This shows that even with a 10 % under-catchment from the double fence gauge, MEPS would still overestimate the surface accumulation (12 h: +43.8 %; 24 h: +39 %).

On 24, 25, and 26 December 2016 winds between  $5 \text{ m s}^{-1}$  and  $20 \text{ m s}^{-1}$  were observed (Figure 4.1.3d, 4.1.5d, 4.1.6d). The accumulation after 12 h lead time in Table 4.2.4 indicate if wind may have influenced the catchment of the double fence and effect the result of overestimation. It shows,

**Table 4.2.4:** AS Table 4.2.3, adjusted just for an under-catchment of 10 % difference by the double fence gauge.

Day in 2016	12 h accumulation					24 h accumulation				
	Amount		Difference	Average difference	Amount		Difference	Average difference		
	obs.	MEPS			obs.	MEPS				
	[mm]		[%]	[%]		[mm]	[%]	[%]		
21 Dec	0.8	5.1	+553.5			19.0	18.5	-2.5		
22 Dec	15.1	13.4	-11.4			28.4	31.3	+9.9	-0.3	
23 Dec	7.0	6.6	-6.2			25.9	23.7	-8.4		+19.3
24 Dec	16.3	17.7	+8.4			27.6	35.9	+30.3		
25 Dec	4.8	6.7	+39.6			17.1	23.3	+35.8	+39.0	
26 Dec	9.8	17.9	+83.6			27.9	42.1	+50.8		

overestimation would still be present on 25 and 26 December 2016. On the other hand, overestimation would not be present for 24 December 2016 until 12 h accumulation.

Still, an simulation of too much surface accumulation is apparent for 24 h lead time. It seems even though the double fence gauge is influenced by wind, the overestimation of surface accumulation by MEPS is still present.

In order to quantify the statistical uncertainty of the ensemble members, a box-whisker plot is provided in Figure 4.2.6. The box-whisker-plots in Figure 4.2.6 show the time evolution of the distribution of the precipitation amount made of ten ensemble members up to 48 h on 24, 25, and 26 December 2016 (Figures 4.2.6a to 4.2.6c). Figure 4.2.6 provides information every 3 h, since some ensemble member do not have forecast values every hour.

All three days with overestimation seem to have different variability between the ensemble member. As expected the forecast uncertainty increases with longer forecast time for precipitation amount. Figure 4.2.6b and c show a smaller ensemble member variability on 25 and 26 December 2016 than on 24 December 2016.

Large variability is already present after 3 h prediction time in Figure 4.2.6a on 24 December 2016. The spread between the ensemble members (shown by the minimum and maximum whiskers) seems to be wide indicating a large uncertainty of the amount of surface accumulation. The ensemble mean (red line) is always higher than the median, suggesting a positively skewed distribution. This means more low surface precipitation amount is predicted than large surface precipitation amount at the surface.

After 12 h forecast time, the median is closer to the lower 25th percentile, indicating a negative skewness. Also, all upper whiskers in Figure 4.2.6a are longer than the lower ones. This shows, that more ensemble members predict high precipitation amount instead of little.

The variability in Figure 4.2.6b show no large variation between the ensemble members (narrow box-whiskers) on 25 December 2016. This day is also the forecast with the smallest wet bias of 5 mm on the three days with overestimation (Figure 4.1.11e). This may be related to the small variability between the ensemble members in Figure 4.2.6b. The variability in the forecast increases after 15 h prediction time. Median and mean agree well for the entire period of a 48 h lead time.

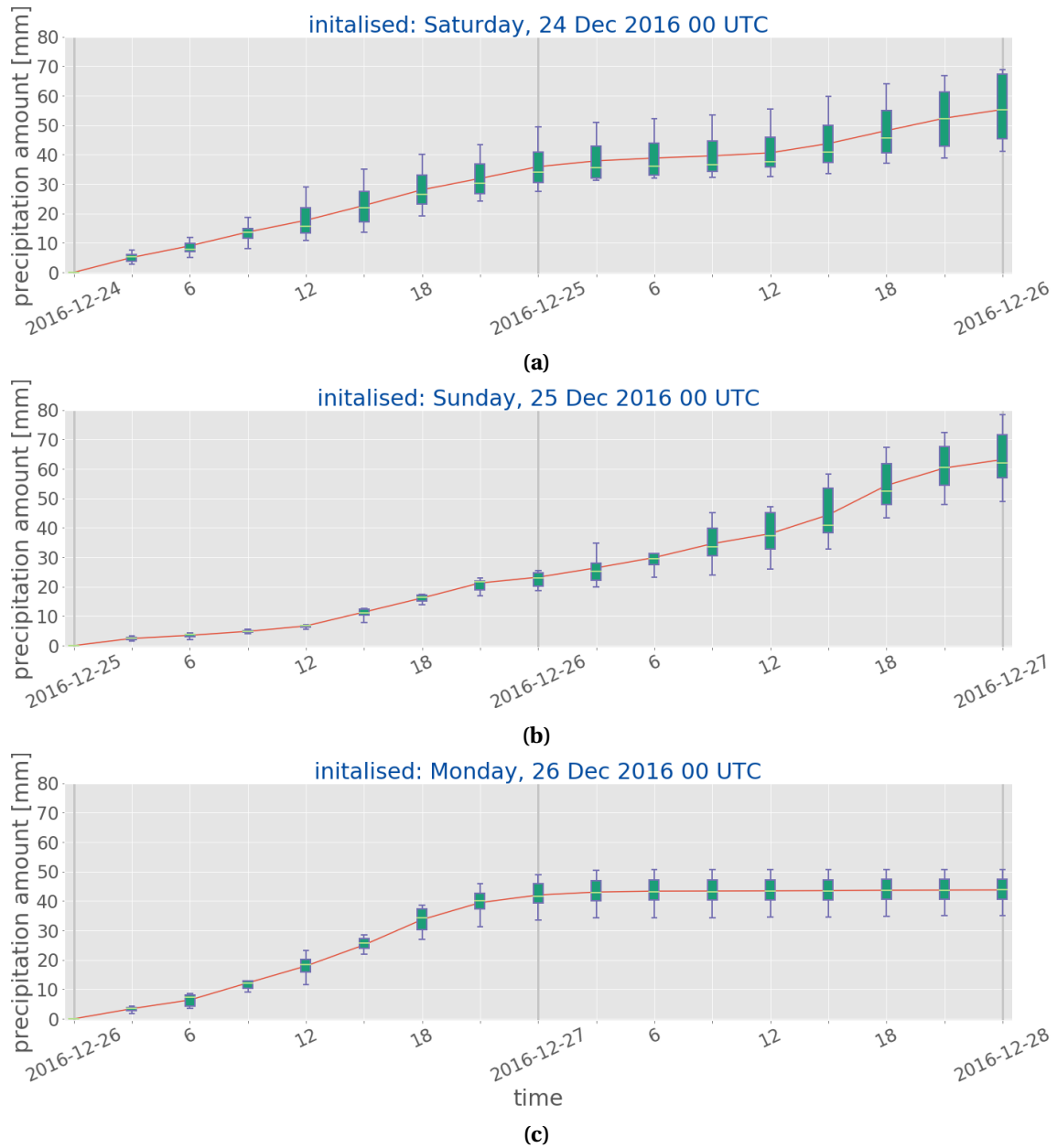


**Figure 4.2.6:** Box-whisker-plot in order to quantify the statistical uncertainty of the ten ensemble members of MEPS. The red line shows the ensemble mean of all ten members and if the distribution is skewed. The short light green, horizontal line is showing the median, the wide vertical box represent the 25th and 75th percentiles, and minimum and maximum values are indicated by the vertical lines, whiskers.

After 39 h the mean is much higher than the median in Figure 4.2.6b, indicating that more surface precipitation amount is predicted by most ensemble members. It seems, that all ten ensemble members agree well on the prediction and nevertheless MEPS overestimates the surface accumulation.

On 26 December 2016 the highest deviation to the double fence observations is estimated (Table 4.2.4). The precipitation amount forecast is overestimating at 12 UTC in Figure 4.2.5c. Figure 4.2.6c indicates increasing variability after 6 h, but the variability between the ensemble members is not as large as on 24 December 2016 after 12 h lead time. Nevertheless, agree the ensemble member the least about the precipitation amount at 12 UTC. The spread between the

ensemble members is wide showing the variability of the forecast members. As Figure 4.2.5c also shows is the double fence observation not within the spread of the ensemble member after 9 h lead time. According to Müller et al. [2017] strong precipitation events are better predicted with AROME-MetCoOp than with ECMWF. In Section 2.2 it was described, that during 21 to 27 December 2016 56.9 % of the total December 2016 accumulation of precipitation were observed. The extreme 2016 Christmas event follows to be a strong precipitation event. The overestimation at the surface could be related to the 10 % under-catchment by the double fence gauge under high wind condition. As Table 4.2.4 indicates the difference between the forecast system and the double fence observations is decreased, but still too much surface accumulation is estimated by MEPS. The difference for 12 h lead time on 25 and 26 December 2016 is however more than 40 %. Only a 10 % under-catchment by the double fence is assumed in this thesis. Wolff, [unpublished] states that estimates for higher wind speeds such observed at Haukeliseter do not exist but is hypothesized to be within 20 %. During the event the 10 m observed wind was less than  $20 \text{ m s}^{-1}$  for 10 min averaged wind speeds prior the full hour. The forecast error could be reduced because of the wind related effect of the double fence.

The uncertainty of the surface accumulation might also have been related to the fact that the large-scale situation intensified more than low pressure systems in Norway usually do.

The overestimation on 24 December 2016 can be related to the high precipitation amount in the evening of 23 December 2016. The precipitation amount associated with the transition of the occluded front on 23 December 2016, after 18 UTC, is higher than on previous days (Figure 4.2.4c and Figure 3.5.4e). During 20 to 21 December 2016, the hourly precipitation around 0 UTC is less intense than on 23 December 2016 (Figure 3.5.4e). High accumulation amount over shorter time followed and could have resulted in a larger variability of the MEPS members (Figure 4.2.6). In the analysis cycle 3 h prior the initialisation of MEPS observations are included inside the model domain [Homleid and Tveten, 2016]. Since the precipitation amount associated with the occlusion passage on 23 December 2016 was quite high, might this have led to the overestimation of surface precipitation amount. [Homleid and Tveten, 2016]

Another possibility is that MEPS might have accounted for more precipitation around 12 UTC on 24 December 2016 than was observed. This could show the large predicted precipitation amount in Figure 4.2.5a at 13 UTC.

On 25 December 2016 MEPS surface forecasts suggest that MEPS did not expect the occurrence of a warm front (Figures 4.1.5a to 4.1.5d). However, from the surface accumulation prediction it could be concluded that MEPS expected more precipitation around 12 UTC on 25 December 2016. Maybe MEPS has expected a less intense warm-front passage and therefore more precipitation. The fact that the temperature is rising and therefore the phase is changing from snow to liquid precipitation (Figure 4.1.10) may have led to MEPS expecting more liquid precipitation hence MEPS predicted more surface accumulation.

On 26 December 2016 between 15 UTC and 18 UTC, the core of the Christmas 2016 low-pressure system passes over Haukeliseter (Figures 4.1.6a to 4.1.6d). Overestimation of surface accumulation are seen after 12 UTC in Figure 4.2.5c. It is very likely that overestimation on 26 December 2016 is related to passage of the low pressure system, since ensemble prediction systems are not adjusted

to predict perfectly for extreme events.

Observations are used as initial condition in weather forecast systems, such as MEPS. As described in Section 2.5, should the observations be within the spread of the ensemble member prediction. Furthermore, the forecast members should be close together for a short time, so they may be considered *deterministic*. This is not the case for 24 to 26 December 2016 after 12 h lead time.

Uncertainties appearing already after 3 h and 6 h on 24 and 26 December 2016 could be associated with a long spin-up time of MEPS. As described in Section 2.5, MEPS precipitation has a spin-up time of 6 h and values before that should not be used as very certain [Køltzow, 2018, personal communication]. Even though this is taken into account, Figure 4.2.6 show larger variability for the ensemble members on 24 and 26 December 2016 after 6 h prediction.

As a result of poorer initial conditions the spin-up time could have been longer on 24, 25, and 26 December 2016. The spin-up time can vary due to less or also uncertain observations going into the initialisation [Warner et al., 1997]. Observations are fed into MEPS directly by using the operational global forecast model ECMWF. Less observations can be due to instrumentation failure or the data has not been transmitted in time to the forecasting system. Observations and data assimilation have errors and this can increase the initial uncertainty in a weather forecast. Boundary conditions have also uncertainties, such as insufficient details of the sub-grid scale and parametrised surface fluxes [Owens and Hewson, 2018]. The atmosphere is a chaotic system and it depends sensitive on initial conditions. Small uncertainties can to large errors [Lorenz, 1969]. Furthermore, model uncertainties such as parametrisations of physical processes and the limited model resolution exist. Because of these errors the model needs to stabilise. When the stabilised state is reached the results can be more trusted [Hollingsworth, 1979]. Longer spin-up time than the usually 6 h for precipitation can lead to larger variation from early on in Figure 4.2.6a and c than e.g. on 25 December 2016. More variability between the ensemble members does not necessarily mean that a forecast is bad, it only shows the predictability.

Since the box-whisker-plot in Figure 4.2.6b (25 December 2016) show less variability in the beginning it is assumed that spin-up time issues are less likely, but not totally excluded. It could be related to an error in the initialisation, even though it does not show within the variability at the beginning.

The overestimation of accumulated precipitation during 24 and 26 December 2016 might be related to local horizontal resolution of MEPS at Haukeliseter as well as to the complex development of the low-pressure system north-west of Norway on 24 December 2016.

Ensemble prediction systems have the advantage that they present the variability of possible observation. The studies from Buizza et al. [1999], Petroliagis et al. [1997] show that the ECMWF ensemble prediction can be extremely beneficial for evaluating the forecast skill during extreme precipitation events. The spread between the ensemble members should include the uncertainty of surface observation. This might not always be the case, especially during extreme events, if high amounts of precipitation are expected over a short time.

Another likelihood for the simulation of high precipitation amount during the intensification of the extreme event may be related to the local topography and the strong winds. Furthermore, the orographic representation in the regional model MEPS can influence the simulation. Effects of the topographical resolution on MEPS at Haukeliseter, will be further discussed in Section 4.2.5. Even though with the launch of MEPS the variation of observations is covered, the forecast system seems not to be able to represent surface precipitation amount for this particular extreme weather event.

#### 4.2.4 SNOW WATER CONTENT

Frontal passages were observed at the surface several times throughout the extreme storm in December 2016. MEPS is able to predict the large scale synoptics and related precipitation, temperature, and wind changes for initialisation more than 24 h in advance (Section 4.1). Three additional instruments were installed to measure frozen precipitation up to 3 km at Haukeliseter. This gives the opportunity to compare the forecasts with retrieved vertical snow water content (Sections 4.2.1 and 4.2.2). This study is unique because it uses state of the art vertical measurement to compare to an ensemble prediction forecast system. As far as the author is aware of there is no study about verification of MEPS for the vertical with observations.

The motivation to compare regional model forecasts with vertical snow measurements resulted from a study by Joos and Wernli [2012]. They did sensitivity studies on the microphysical scheme of COSMO (COnsortium for Small-scale MOdelling) and found that the storm development depends on the correct vertical placement of the precipitation inside a modeled storm. Vertical precipitation placement determines the vertical profile of latent heating, and hence the generation of potential vorticity which in return shows if a storm strengthens or weakens. Correct vertical precipitation observations can then help to correctly evaluate model vertical precipitation patterns.

Passages of occluded fronts and a warm sector were observed on 23, 26, and 25 December 2016. Additionally, an overestimation at the ground is shown on 24, 25, and 26 December 2016 for surface precipitation amount (Section 4.2.3, Figure 4.2.4 and 4.2.5).

Figure 4.2.7 shows the reflectivity from the MRR at Haukeliseter for these days. Likely periods of frozen precipitation are indicated with orange and red in Figure 4.2.7. On 26 December 2016 only values until 17 UTC are displayed, because of the temperature change and hence a precipitation shift led to liquid drops freezing on the MRR dish so that the signal got attenuated.

During the Christmas 2016 extreme event two precipitation patterns are seen in the vertical. First, a continuous precipitation pattern with constant precipitation over several hours. In the following it is referred to as *continuous*. The second pattern shows interchangeable high and low amounts of snow over 1 h. This will be referred to as *pulsing*.

More continuous precipitation pattern with high reflectivity values in Figure 4.2.7 indicate the transition of the occlusion on 23, 26, and the warm sector passage on 25 December 2016. The high reflectivity on 23 and 26 December 2016 shows the passage of the occlusion and the associated frozen precipitation.

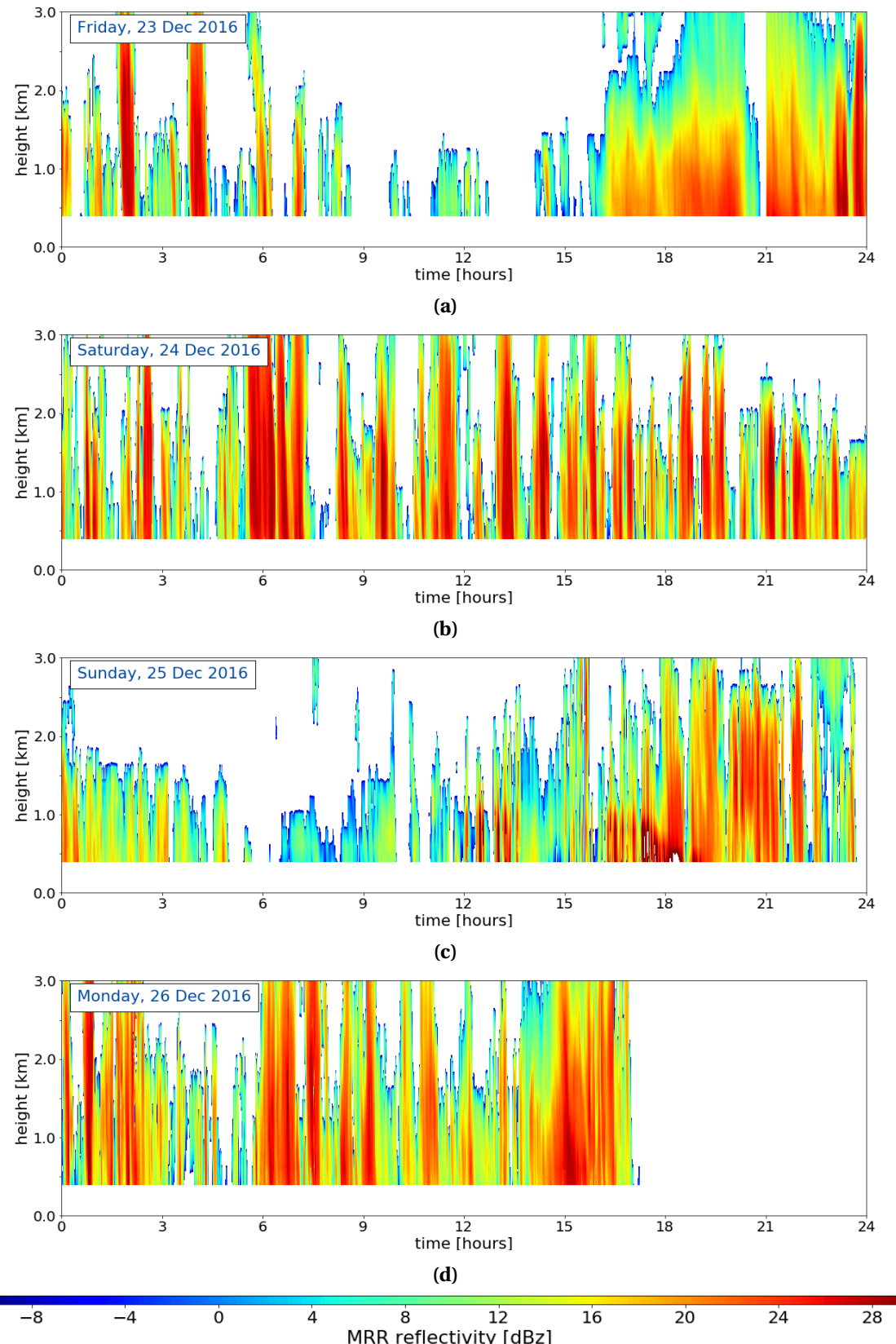


**Figure 4.2.7:** MRR reflectivity for the days with frontal passage and overestimation at the ground at Haukeliseter. dBZ reflectivity according to the colour bar, with weaker precipitation in blue and more intense precipitation in red. Presenting the reflectivity without applying the environmental masks described in Section 2.4.2. a-d 23 to 26 December 2016.

On 23 December 2016, the surface observations of sea level pressure (Figure 4.1.3a), 2 m air temperature (b), and 10 m wind (c), allow to assume that the occluded front passed through Haukeliseter between 12 UTC and 21 UTC. Figure 4.2.7a shows high observed reflectivity in the lower up to 3 km at Haukeliseter after 16 UTC. After 16 UTC, the wind is from the south, upslope (Figure 4.1.3c, Figure 2.1.1b) which led to a continuous precipitation pattern in Figure 4.2.7a. In the morning of 23 December 2016 high amount of frozen precipitation was observed at 2 UTC and 4 UTC, but with a more pulsing pattern than in the evening.

Another occlusion passed through on 26 December 2016 between 15 UTC and 21 UTC (compare surface observations Figure 4.1.6a to e). A pulsing precipitation pattern and high reflectivity in Figure 4.2.7d indicate the passage after 15 UTC. While on 23, 24, and 26 December 2016 the reflectivity did not pass values larger than 28 dBZ, Figure 4.2.7c shows high reflectivity values larger than 30 dBZ on 25 December 2016 (compare for approximation Table 2.3.1). These high reflectivity values up to 1.2 km in Figure 4.2.7c indicate the observation of possible liquid precipitation on 25 December 2016. Images from the MASC were able to verify observed liquid drops during 12 UTC to 21 UTC (Figure 4.1.10). In the observations on 25 December 2016, high temperatures (Figure 4.1.5b) are shown, between 12 UTC to 21 UTC. On 24 December 2016 short, interchangeable high and low reflectivity patterns are present in Figure 4.2.7b. Figure 4.1.4c and d indicate strong wind from the west which led to a pulsing precipitation structure in Figure 4.2.7b on 24 December 2016. The same pulsing is seen on 26 December 2016 before 12 UTC in Figure 4.2.7d. A comparison with the observed surface wind in Figure 4.1.6c and d shows also westerlies. The orographic influences on the surface wind and therefore a possible relation to the precipitation patterns will be further investigated in Section 4.2.5.

Figures 4.2.9 to 4.2.13 present the reflectivity of the MRR and the snow water content retrieved from the reflectivity as well as the 48 h forecast values. Minutely MRR reflectivity and retrieved snow water content can be seen in Figure 4.2.9a to 4.2.13a. Figure 4.2.9b to 4.2.13b show in the upper panel the hourly averaged values from the retrieved SWC and in the lower panel the ensemble mean of the instantaneous forecast values every hour over all ensemble member. Three hourly averaged retrieved values are then presented in the upper panel of Figure 4.2.9c to 4.2.13c, the lower panel are the ensemble mean forecast values every three hours.

On 23 December 2016 an occlusion passes over Haukeliseter between 16 UTC and 23 UTC. The passage of the occlusion on 23 December 2016 is already predicted for initialisations on 22 December 2016 in Figure 4.2.9b, c. With shorter lead time the snow water content for hourly and three hourly ensemble means increases in Figure 4.2.10b and c after 16 UTC on 23 December 2016. MEPS is able to estimate the snow water content for ensemble means of time resolutions 3 h in Figure 4.2.9c, 4.2.10c.

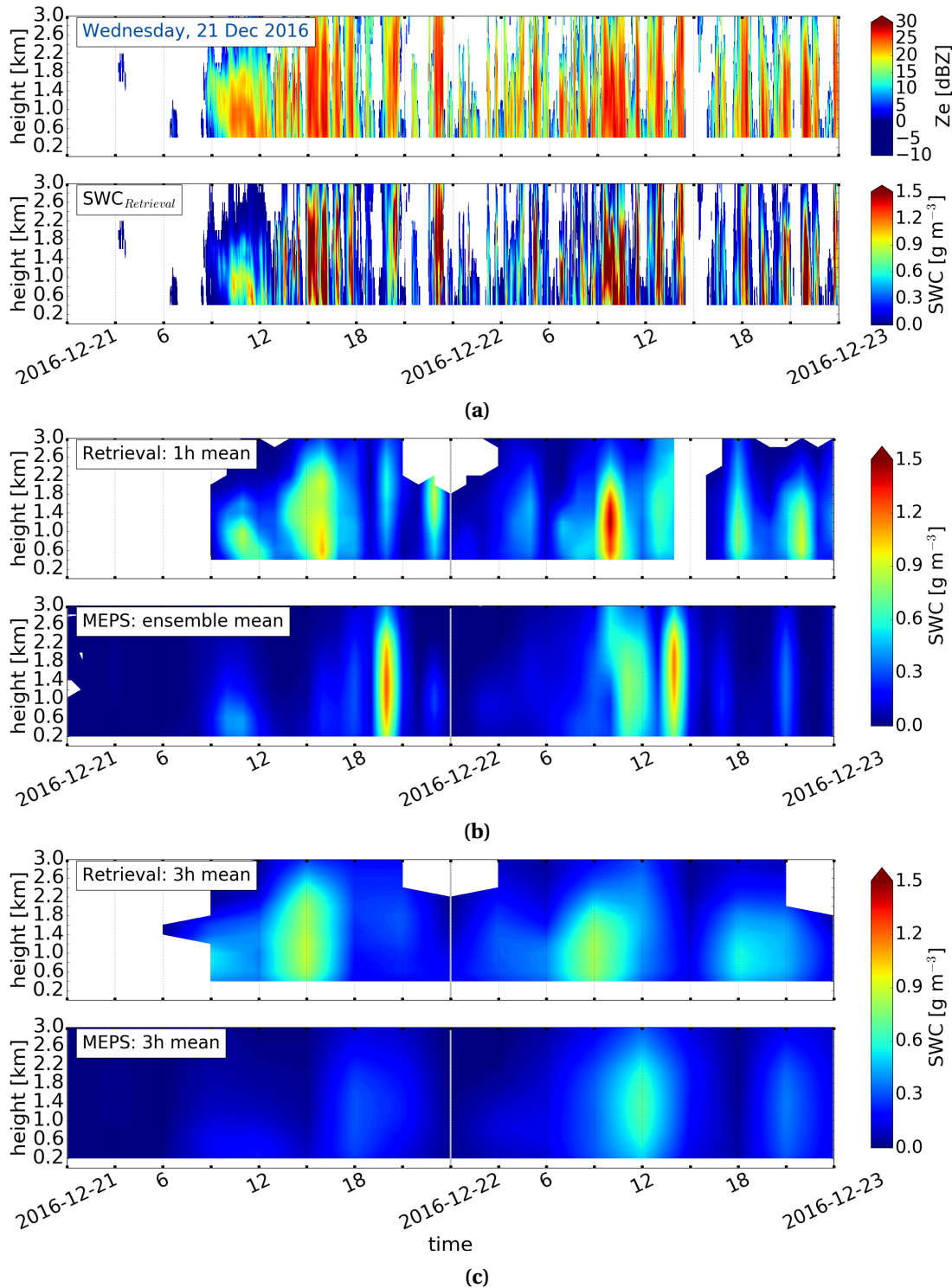


**Figure 4.2.8:** Initialisation on 21 December 2016 at 0 UTC. From top to bottom: (a) Microwave Rain Radar reflectivity [dBZ] for 48 h, minutely retrieved snow water content. (b) Hourly averaged retrieved snow water content, lower panel instantaneous hourly ensemble mean, neglecting missing values. (c) Three hourly averaged retrieved snow water content, lower panel instantaneous three hourly ensemble mean. Representation according to the colour-bar, with reflectivity ranging between  $-10 \text{ dBZ}$  and  $\geq 30 \text{ dBZ}$ , snow water content between  $0 \text{ gm}^{-3}$  and  $\geq 1.5 \text{ gm}^{-3}$ .

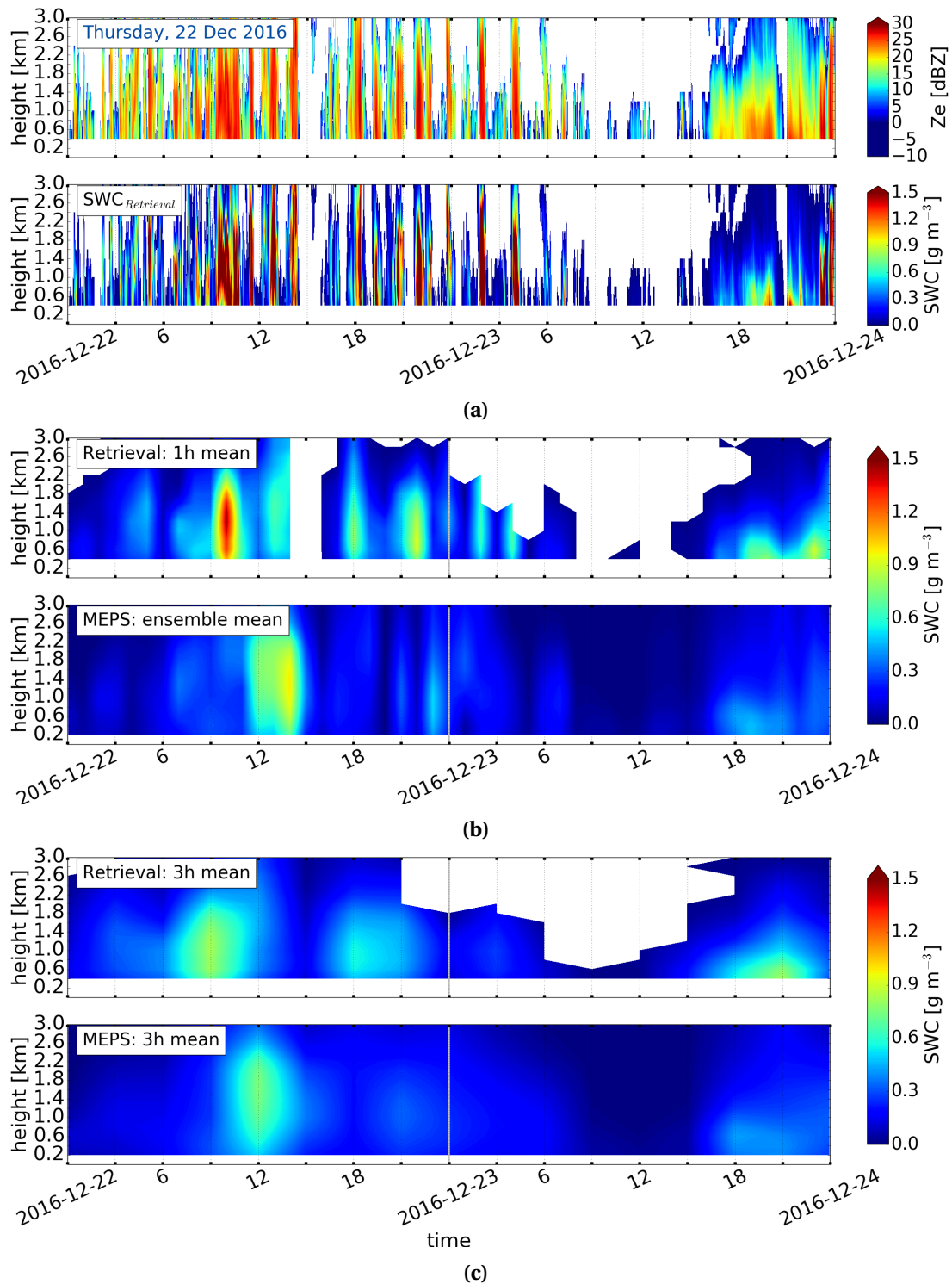


**Figure 4.2.9:** (As Figure 4.2.8.) Initialisation 22 December 2016 at 0 UTC.

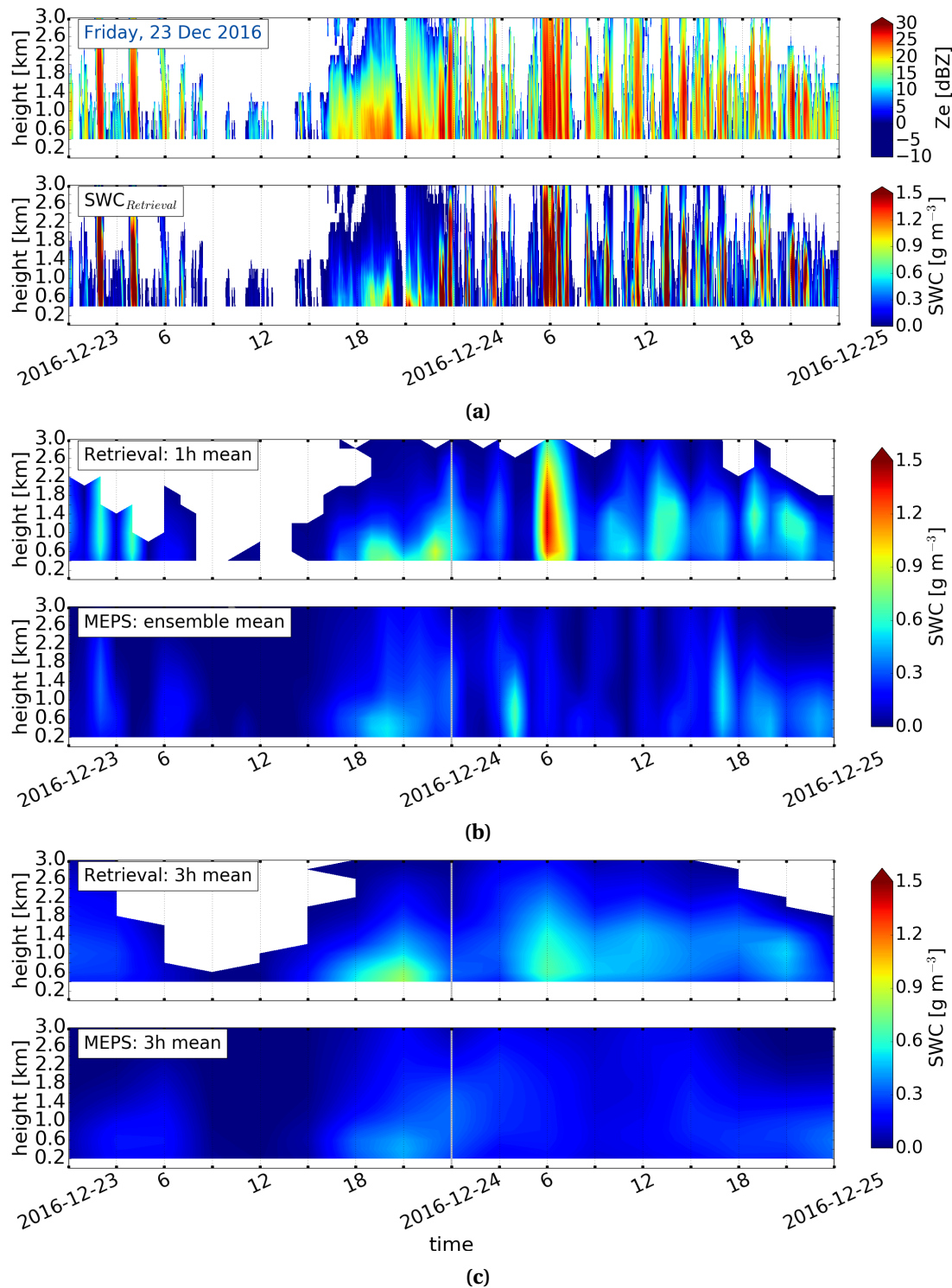


**Figure 4.2.10:** (As Figure 4.2.8.) Initialisation 23 December 2016 at 0 UTC.

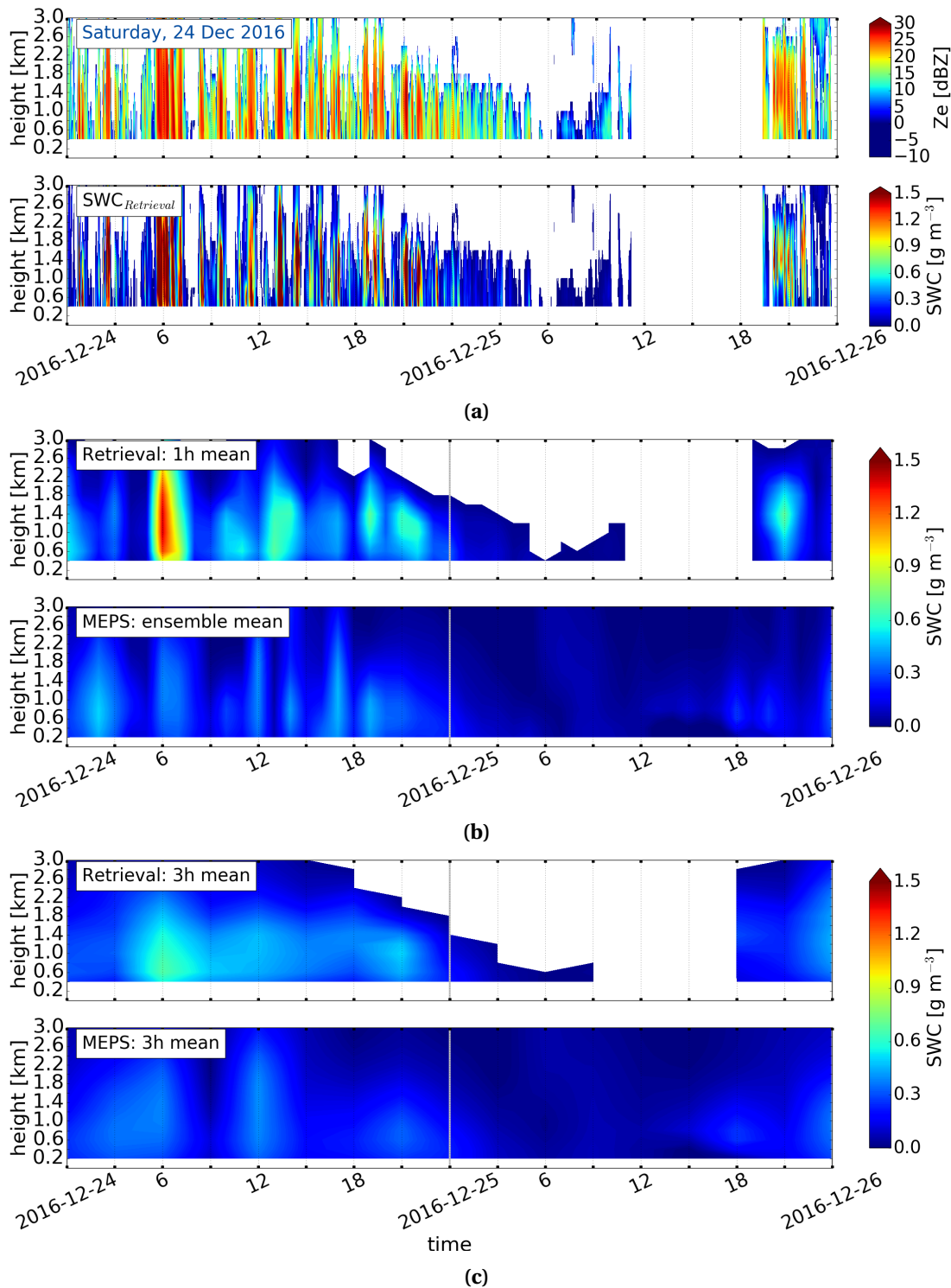


**Figure 4.2.11:** (As Figure 4.2.8.) Initialisation 24 December 2016 at 0 UTC.

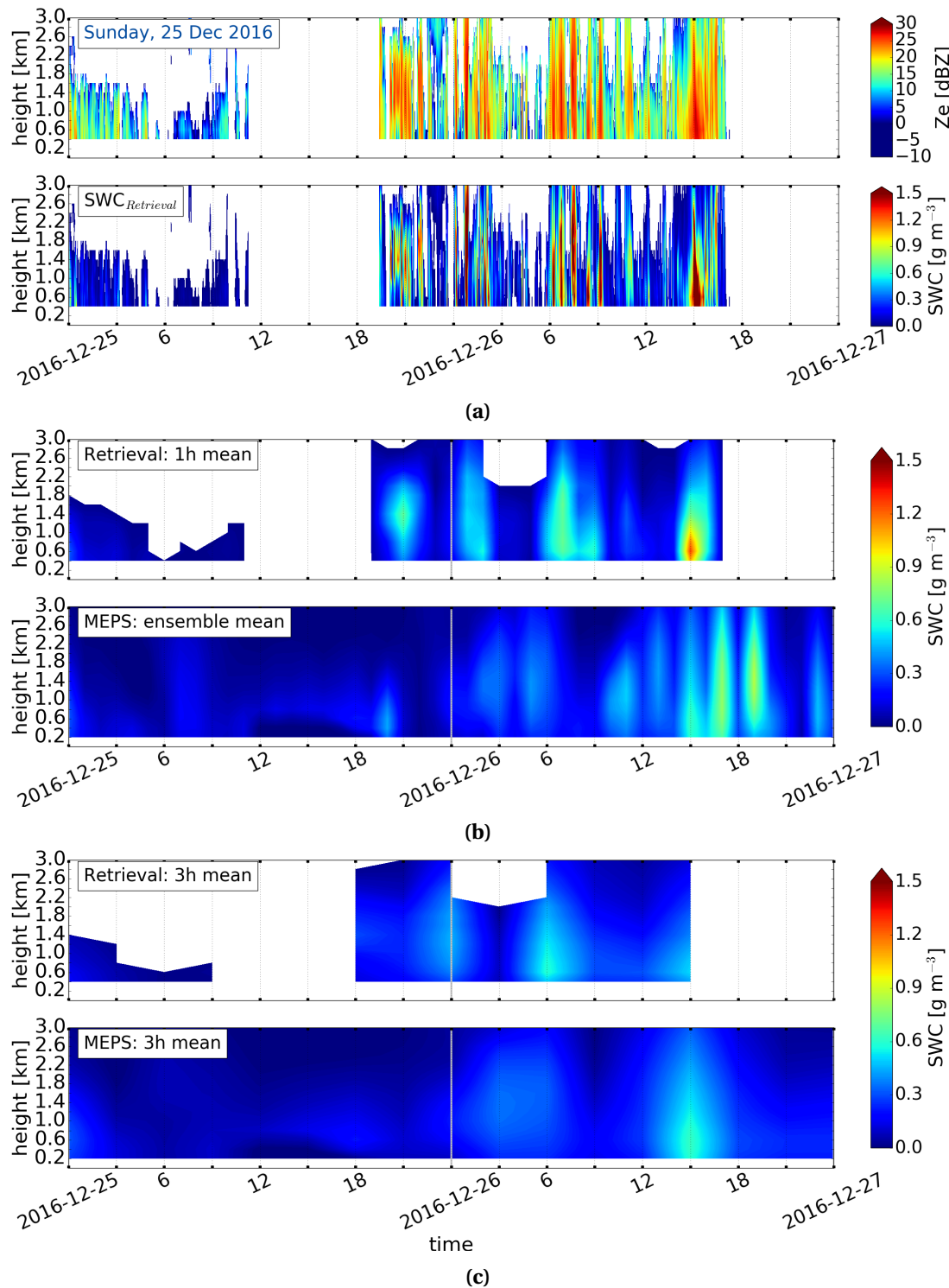


**Figure 4.2.12:** (As Figure 4.2.8.) Initialisation 25 December 2016 at 0 UTC.

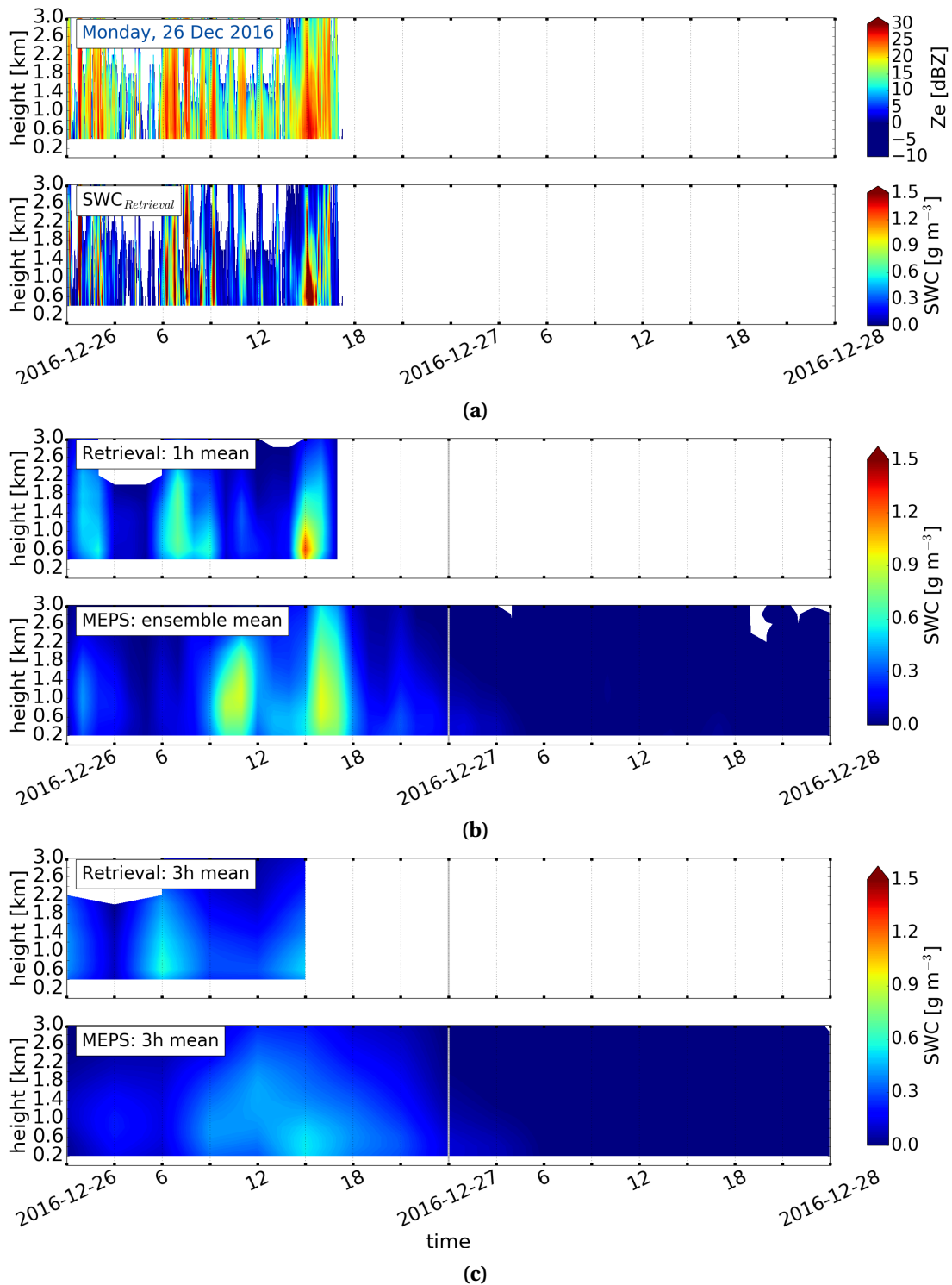


**Figure 4.2.13:** (As Figure 4.2.8.) Initialisation 26 December 2016 at 0 UTC.

On 26 December 2016, retrieved snow water content until the passage of the occlusion is observed (Figures 4.1.6a to 4.1.6e). The average of all ensemble members (Figure 4.2.13b) as well as the three-hourly instantaneous SWC (Figure 4.2.13c) predict the frontal transition between 15 UTC and 21 UTC. Initialisations already 39 h prior (25 December 2016) simulate that intense precipitation will occur over a short time (Figure 4.2.12b, c).

In general, the 25 December 2016 storm had little snow but much liquid precipitation observed between 11 UTC and 19 UTC in Figure 4.2.7c. The retrieved snow water content in Figure 4.2.11 and 4.2.12 show a gap of missing values during liquid precipitation (Section 2.4.2). The initialisations on 24 (Figure 4.2.11) and 25 December 2016 (Figure 4.2.12) show forecasted snow water content less than  $0.4 \text{ gm}^{-3}$  for 25 December 2016 while the retrieved maximum value is  $0.7 \text{ gm}^{-3}$  at 15 UTC. To see if liquid precipitation is predicted, the atmospheric cloud condensed water content and rainfall amount in model levels is summed (Figure 4.2.14). Figure 4.2.14a and b show liquid water content for initialisations on 24 December 2016 and 25 December 2016, respectively. Positive 2 m air temperatures are forecasted between 12 UTC and 21 UTC (Figure 4.1.5b). Initialisations more than 24 h prior (24 December 2016) already show the occurrence of the liquid precipitation layer (Figure 4.2.14a). Figure 4.2.14a and b also show a narrow liquid layer thickness up to 800 m for initialisations on 24 and 25 December 2016.

In Norwegian mountainous terrain this is an important forecast ability, since precipitation change can lead to an increased risk for people. The avalanche danger increases with the precipitation change especially during high wind speeds [Hansen et al., 2014]. A change from snow to liquid precipitation increases the risk of transport accident because of freezing rain. Since MEPS forecasts the liquid layer correctly in thickness and duration it seems to be a good interaction between the 2 m air temperature and the temperature in model levels. To produce the forecast analysis in MEPS, upper-air and surface assimilation is decoupled when starting from the model background (Section 2.5.2). MEPS 2 m air temperature forecasts show the increase in temperature between 12 UTC and 18 UTC on 25 December 2016 (Figure 4.1.5b). This follows, that 2 m air temperature is correctly translated to the upper model levels by applying a realistic temperature gradient, so that liquid precipitation is forecasted. The model level temperature must also reach a certain temperature threshold to forecast precipitation as liquid. This follows a high accuracy of MEPS for liquid forecast and the positive impact of using a high resolution convective scheme model. Precipitation is placement dependent. Lower horizontal resolution models, such as ECMWF, simulate for large grid cell area. This may lead that low temperature at a mountain top is predicted even though the meteorological observation in a valley observes rain, because an altitude difference of some hundred meter.

The hourly ensemble mean using all ensemble members and neglecting the missing values is not a fair comparison. Therefore, an ensemble mean is created only with the deterministic and first perturbed ensemble member. Averaging only the deterministic and first perturbed ensemble member forecast leads to little snow water content (Figure B.1.1). Figure B.1.1b, c and e, f show no occurrence of occlusion passages on 23 and 26 December 2016, respectively. Furthermore, the pulsing on 24 December 2016 is seen weaker for initialisations on 24 December 2016 (Figure B.1.1d), but not 48 h prior.

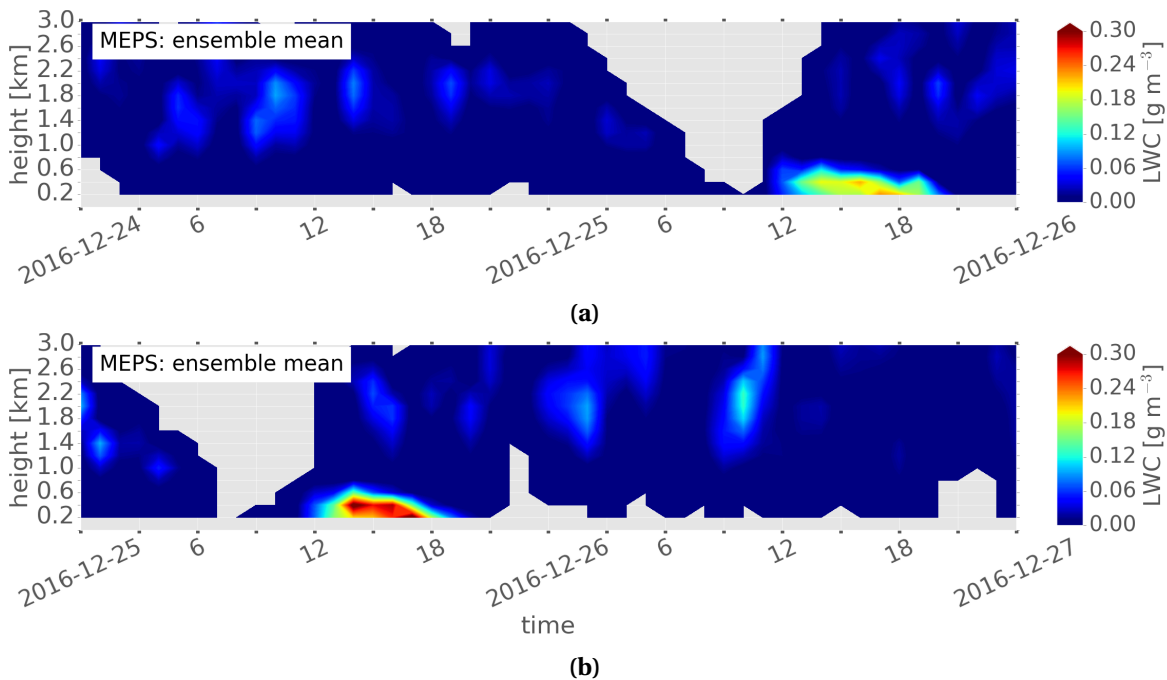


**Figure 4.2.14:** Ensemble mean 48 h MEPS forecast for liquid water content. The Liquid water content is averaged over a layer thickness of 200 m. Missing values are neglected. Liquid water content according to the colour bar. Initialised on 24 December 2016 and 25 December 2016 at 0 UTC.

A comparison with all other days show the same result, when only the deterministic forecast and first perturbed member is used Figure B.1.1.

In Figure B.2.1, a comparison with each individual ensemble member shows high instantaneous values ( $\geq 2.0 \text{ gm}^{-3}$ ), especially for the deterministic and first ensemble member. This is seen for initialisations on almost all days during the Christmas event.

Surface overestimations is seen on 24, 25, and 26 December 2016 (Section 4.2.3). Higher predicted SWC for the deterministic and first perturbed member (Figures B.2.1d to B.2.1f) might have led to an overestimation of surface accumulation seen in Figures 4.2.5a to 4.2.5c (for ensemble member zero and one).

The variation of each initialised ensemble member for snow water content is given in Figure B.2.1 for the respective day. One possibility to quantify the variability of all ensemble member during the Christmas 2016 storm, is by calculating the coefficient of variation (CV) for SWC, described in Section 2.7. Figure 4.2.15 and 4.2.16 show the coefficient of variation for SWC and gives the possibility to compare the SWC for different days with each other. The interpretation of the coefficient of variation for SWC is presented in Table 4.2.5.

The grey line in Figure 4.2.15 and 4.2.16 presents the ensemble mean of the hourly predicted SWC values. The darker the shading, the smaller the variation of the SWC relative to the mean.

MEPS data does not exist for all ten ensemble members on 23 December 2016. No coefficient of variation is calculated for this day, since only six perturbed members were available. Therefore, the initialisation on 22 December 2016 is used to validate the forecast. On 23 December 2016, two intense SWC pulses are observed in the lower troposphere at 2 UTC and 4 UTC (Figure 4.2.10a). The deterministic forecast, initialised on 22 December 2016 predicted a pulse at 1 UTC and 3 UTC,

**Table 4.2.5:** Interpretation of the coefficient of variation for SWC.

Size of CV [%]	Interpretation variability
0 to <25	negligible
25 to <50	low
50 to <75	moderate
75 to <100	high
100 to $\infty$	very high

where the first perturbed ensemble member (EM1) has a strong SWC at 3 UTC. Initialisations 24 h later show only one pulse in the deterministic forecast at 2 UTC.

The occlusion passage on 23 December 2016 is seen after 16 UTC in Figure 4.2.10. Initialisations on 22 December 2016 (Figure B.2.1b) show for each ensemble member a weak predicted snow water content for the transition of the occlusion. No MEPS forecast data was available for four perturbed ensemble for initialisations on 23 December 2016. The comparison of only six ensemble members in Figure B.2.1c, display low variability between all ensemble members during the up-slope storm. Nevertheless, for initialisations on 22 or 23 December 2016 all ten ensemble members forecast the pulsing precipitation pattern to occur after 16 UTC (Figure B.2.1b and c). For prediction initialised on 22 December 2016 the verification in Figure 4.2.15b shows little variability, below 50 %, and show a good agreement on the occurrence of frozen precipitation after 16 UTC. Before 16 UTC a pulsing precipitation pattern is observed in the lower 3 km at Haukeliseter on 26 December 2016. All ten ensemble member in Figure B.2.1e and B.2.1f predict pulsing patterns. Initialisations on either 25 or 26 December 2016 show interchangeable precipitation for the deterministic and first ensemble member similar as the retrieved snow water content (Figure 4.2.13).

The surface observations for 26 December 2016 indicate the passage of the occlusion at Haukeliseter between 15 UTC and 19 UTC (Figure 4.1.6). A larger variability between the ensemble members than for the occlusion passage on 23 December 2016 (Figure 4.2.15b) is shown for the evolution of the occlusion on 26 December 2016 in Figure 4.2.16a, b.

Initialisations on 25 December 2016 present a lower variability for the transition of the occlusion after 15 UTC on 26 December 2016 (Figure 4.2.16a) than initialisations less than 24 h prior (Figure 4.2.16b). Therefore, an increase of variability for shorter lead time is given in Figure 4.2.16b. The variation of all members for initialisations on 25 December 2016 (Figure B.2.1e) and on 26 December 2016 (B.2.1f) indicate that almost all perturbed member would have predicted the precipitation after 16 UTC on 26 December 2016, but the ensemble mean (Figure 4.2.12, 4.2.13) smears the simulated SWC out.

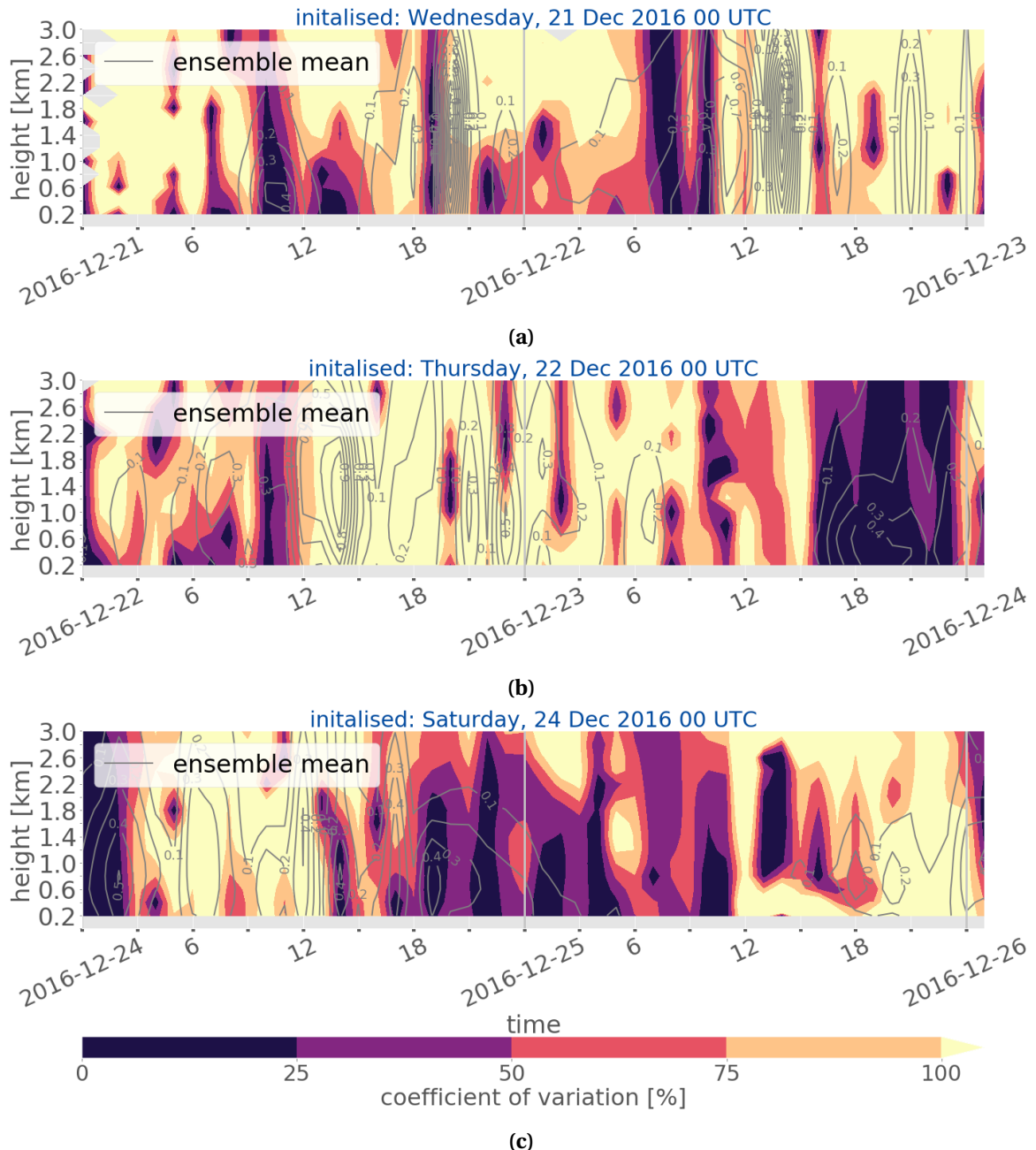


**Figure 4.2.15:** Snow water content variation of the ten ensemble members of MEPS. The lighter the colour according to the colour bar the higher the variation between the perturbed ensemble members. In grey the ensemble mean of all ten members. For initialisations on 21 December 2016.

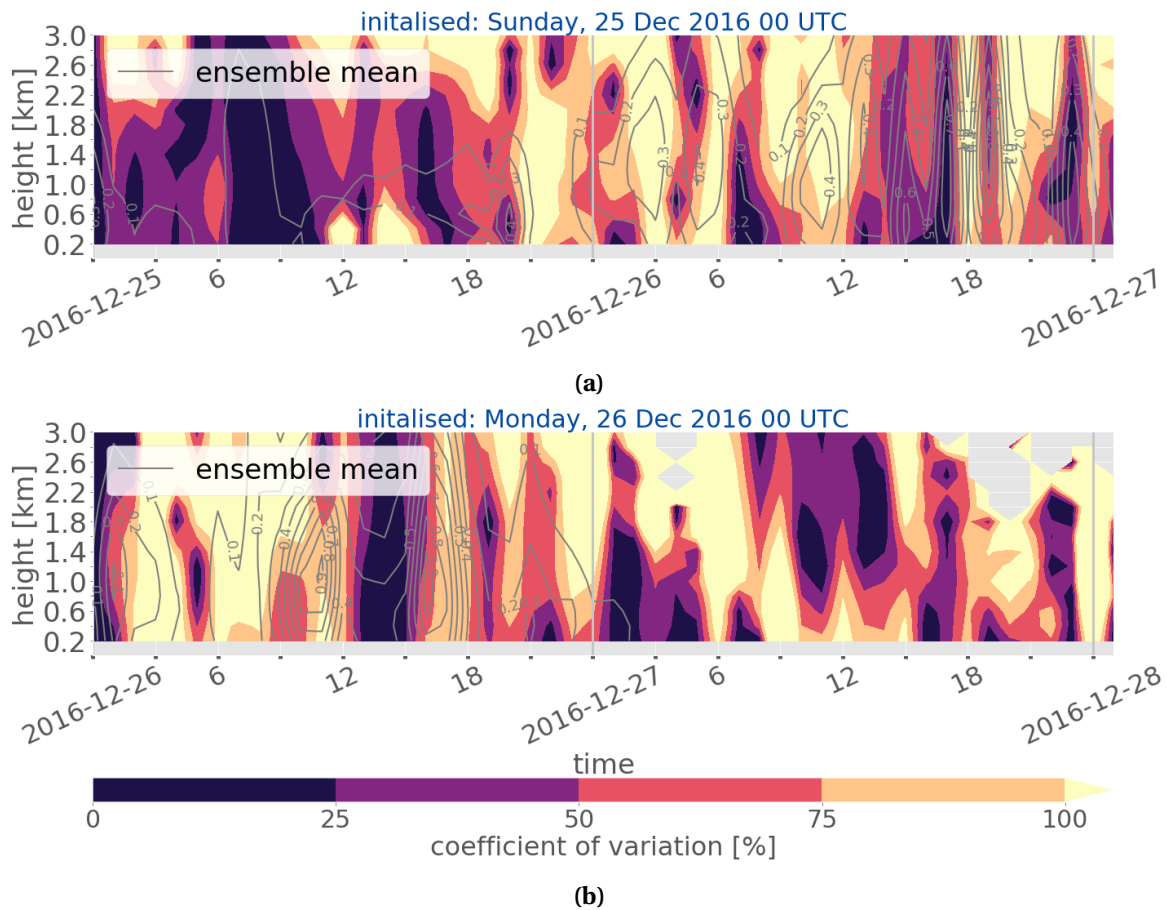


**Figure 4.2.16:** (As Figure 4.2.15.) Initialisation 21, 24, 25 and 26 December 2016.

Initialisations on 25 December 2016 (Figure 4.2.12b, c) show a pulsing precipitation pattern after the occlusion passage. The two pulses around 18 UTC (Figure 4.2.12b) are predicted with a negligible and moderate variability in Figure 4.2.16. The retrieved snow water content in Figure 4.2.13b shows a pulse at 1 UTC. Initialisation on 26 December 2016 forecast a high snow water content around 1 UTC as well. The forecasted SWC pulse at 1 UTC is related to a moderate variability of the ensemble members (Figure 4.2.16b).

Initialisations on 25 and 26 December 2016 show high forecast variability for the predicted SWC between 9 UTC and 12 UTC. The peak between 15 UTC and 18 UTC has a low to moderate variability between the members. When looking at Figure B.2.1f might this disagreement be related to the variation of the vertical predicted SWC. There seems to be no agreement between the different members about the incidence of the different SWC pulses on 26 December 2016. The high conflict for the CV before noon is most likely related to the high SWC of the deterministic SWC.

On 25 December 2016 forecasts for the warm sector passage show liquid precipitation (Figure 4.2.14). Initialisations on 24 December 2016, indicate very low forecast variability up to 0.8 km until noon, this is when liquid precipitation was forecasted by MEPS and observed (Figure 4.1.10). The depth of the liquid layer is up to 0.8 km in Figure 4.2.14a and 4.2.14b. Figure 4.2.15c and 4.2.16a show the variation for SWC on 25 December 2016. Between 12 UTC and 18 UTC the variation is large below 0.8 km. This is related to the ten ensemble members in Figure B.2.1. Each ensemble member shows between 12 UTC and 18 UTC little SWC. This little snow water content

leads to a higher coefficient of variation and displays as a high variability although all ensemble members agree on the timing of liquid precipitation. Above 0.8 km the variability for snow water content between the members is low. Initialisation on 24 December 2016 show low snow water content pulses in Figure 4.2.11b and c at 18 UTC, which had a moderate variability (Table 4.2.5, Figure 4.2.15c). Afterwards it is very high. For the initialisation on 25 December 2016 show low forecast variability until noon (Figure 4.2.16a). While liquid precipitation is predicted the variability in the lower layer of the troposphere is first very high and shortly before 18 UTC not existing. A high agreement for the SWC pulse at 20 UTC up to 0.8 km exists in Figure 4.2.16a and decreases to be moderate above. Pulsing snow water content patterns are seen for the individual ensemble member forecasts for initialisations on 24 December 2016 (Figure B.2.1d). On 24 December 2016 the observed snow water content in the lower troposphere changed between intense and less intense (Figure 4.2.11).

Comparing hourly instantaneous SWC is not a fair comparison, since there might be a time delay of half an hour about the timing of a pulse which would follow it is not seen in the hourly model forecast. Furthermore, the best agreement is reached for ensemble means of all ten ensemble member at every hour, which smear out the snow amount in the lower 3 km.

The forecasted instantaneous ensemble mean snow water content is lower ( $\leq 1.2 \text{ gm}^{-3}$ ) than the retrieved values ( $\leq 1.5 \text{ gm}^{-3}$ ) for the 2016 Christmas storm. For the first glance MEPS simulates realistic snow water content when compared to observed snow water content up to 3 km and shows similar precipitation patterns. The average of all ten ensemble members leads to a smeared out ensemble mean for hourly or three hourly instantaneous values in Figures 4.2.8 to 4.2.13. To compare if lower snow water content was predicted than retrieved from the optimal estimation retrieval the snow water path is calculated (Section 2.6.3).

Figure 4.2.17 shows the correlation between retrieved and individual ensemble member 48 h fore-

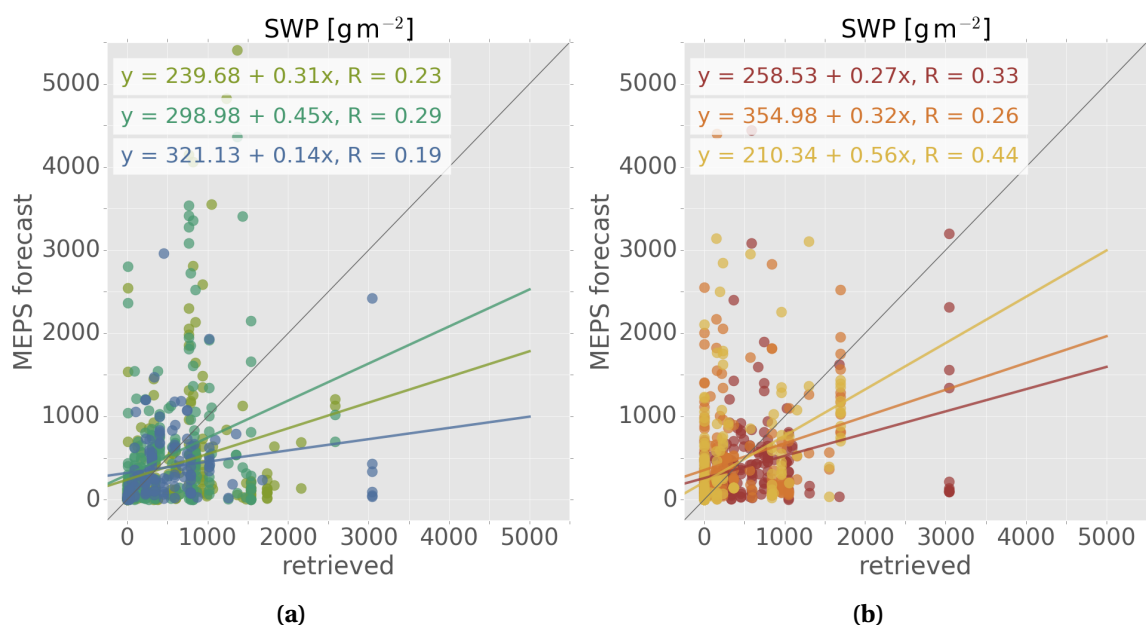


**Figure 4.2.17:** Snow water path correlation between retrieved and forecasted values for 48 h lead time and all ensemble member. Separated for 21 to 23 December 2016 (a) and 24 to 26 December 2016 (b).

casts of snow water path. The slope parameter is for the days of the Christmas storm less than  $0.6 \text{ gm}^{-2}$  indicating a weak uphill correlation between retrieved and predicted values. This shows, retrieved values are larger than the instantaneous ensemble member forecasts for snow water content.

On 24, 25, and 26 December 2016 the surface snow accumulation is overestimated by MEPS (Figures 4.2.5a to 4.2.5c). This overestimation is not seen in the vertical. It might be related to the use of hourly instantaneous values in the vertical whereas the surface precipitation amount is the accumulated total precipitation at each hour.

Furthermore, it could be related to the interaction between the vertical model forecast and the surface forecast. Also, the optimal estimation retrieval fall speed is assumed to be constant ( $0.85 \text{ m s}^{-1}$ , Section 2.4.1) whereas in MEPS the terminal speed velocity is assumed to be related to the particle diameter (Equation (2.5.6)).

One question to answer in this work is if the operational model MEPS simulates large scale weather systems correctly. As discussed here and in Section 4.1 it seems that the model is able to resolve the development of occlusions and warm fronts and its associated precipitation. Even with the intensification of the Christmas 2016 storm MEPS seems to be able to predict extreme events for precipitation such as occlusions and liquid precipitation related to warm sectors.

MEPS also distinguishes realistically between liquid and frozen precipitation in strength and timing for the lower most atmosphere in mountainous terrain in Norway like Haukeliseter. This can be a major challenge since a change in temperature and associated precipitation transformation can lead to high risk in the Norwegian mountains, especially during winter.

The here presented results are a first look, trying to compare a mesoscale ensemble member forecast system (MEPS) with vertical in-situ measurement for snow water content.

The next section will go into detail, how the local orography at Haukeliseter may influence frozen precipitation, and how MEPS's representation of the topography may affect patterns of frozen precipitation.

#### 4.2.5 DISCUSSION

The previous chapters have indicated that the regional model MEPS is able to predict larger scale phenomena. This might be related to the outer boundary condition ECMWF or the Christmas 2016 extreme event was more predictable for large scale weather systems. In general, surface parameters such as sea level pressure and temperature were predicted well in MEPS. Only wind speed and precipitation accumulation showed overestimation in MEPS predictions. Wind speed forecasts were higher than observed wind speed. Related to the representation of the orography in MEPS the general overestimation of wind speed could already be apparent in the deterministic version AROME-MetCoOp.

The Haukeliseter site is exposed to high wind speeds during the winter. The previous results in Section 4.1, 4.2.3, 4.2.4 have shown, that wind plays an important role for the precipitation catchment. Figure 4.2.18a presents the local topography around Haukeliseter. The mountain plateau is surrounded by higher mountains to the west and more open to the south east (Figure 4.2.18a). Figure 4.2.18b shows the 2.5 km grid resolution of the topography by MEPS.

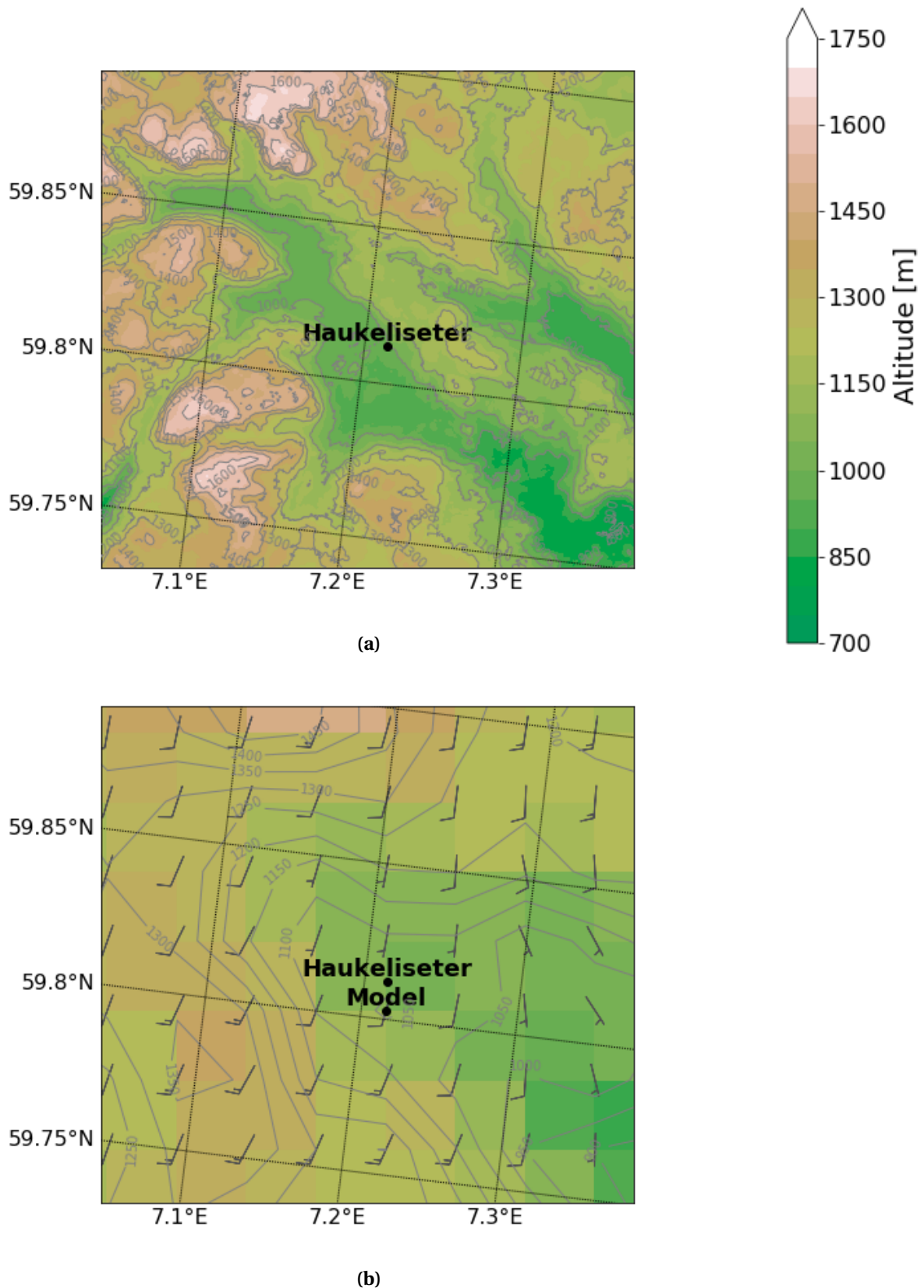


**Figure 4.2.18:** Topography around Haukeliseter. In a the DTM 10 m Terrain Model (UTM33) from Geonorge [2018]. Contours and shading according to the colour bar. b: Representation of the topography and the closest grid point to the measurement site Haukeliseter in MEPS. Contours and shading present the elevation of the grid cells. Wind barbs indicate the wind direction and speed for initialisations on 23 December 2016 at 0 UTC after 18 h lead time

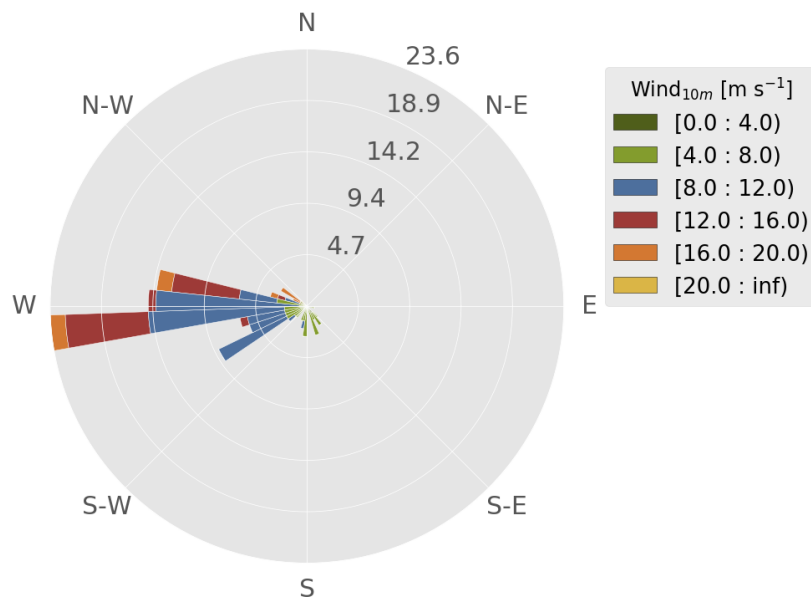


**Figure 4.2.19:** 10 min mean wind observations at 10 m at Haukeliseter during 21 and 26 December 2016. Wind speed according to the colour bar and occurrence indicated by the numbers in the wind-rose.

MEPS resolves some of the complex structure around the site, with the higher mountain to the west and the valley to the south-east (Figure 4.2.18a). Haukeliseter is at an altitude of 991 m above sea level (Section 2.1). In this thesis the closest grid point to the Haukeliseter measurement site is used, which is 59.80° N, 7.22° E (**Model** in Figure 4.2.18b). The altitude of this grid point is 1041 m above sea level.

The elevation map in Figure 4.2.18 shows, that the Haukeliseter measurement site is closer to the mountain to the west, than in reality. The valley to the south-east is shifted to north-east.

Figure 4.2.19 shows the observed 10 m wind during the 2016 Christmas storm. It shows stronger westerly winds up to  $20 \text{ m s}^{-1}$  at Haukeliseter. Measured south-easterlies reach wind speeds less than  $8 \text{ m s}^{-1}$ . Wolff et al. [2010] states that during precipitation events the westerly wind dominates.

Figure 4.1.8b shows a good correlation for west winds, but on the other side, southerly winds seem to be troublesome to predict for MEPS. Figure 4.1.8a indicates an imbalance for south-westerly winds. While south-easterly winds (along the valley) are observed at Haukeliseter MEPS predicts the 10 m wind to be south-westerly (Figure 4.2.18).

Observed south-easterly winds are channelled along the valley (Figure 4.2.18a). For large scale south-westerly flow the MEPS simulates south direction rather than south-easterly flow along the valley. As seen in Figure 4.2.18 for 23 December 2016 after 18 h lead time, the wind blows along the 7.2° E, since a higher (1500 m to 1650 m) elevation is to the west and a 1350 m high mountain to the east.

On 21 and 23 December 2016 wind directions from the south-east (Figure 4.1.1c) and south (c) were observed, respectively.

As earlier discussed in Section 4.1 and 4.2.4, the wind change is associated with the occlusion passage on 23 December 2016 (Figure 3.5.4).

The wind direction change on 21 December 2016 in Figure 4.1.1c is related to the large scale

synoptic flow but is not associated to a frontal boundary (Figure 3.5.2). A comparison with the available large scale weather analysis map from ECMWF (Section 3.5), shows that the large scale surface wind is from the south-west at 6 UTC on 21 December 2016 (Figure 3.5.2c) and has changed to west at 12 UTC (Figure 3.5.2d). The observations at the Haukeliseter site show between 6 UTC and 12 UTC wind from south-east, while the predicted MEPS wind direction is from south in Figure 4.1.1c.

The forecast model seems to forecast the wind direction overall well, only on 21 December 2016 before 10 UTC a south-west instead of a south-east wind is predicted by MEPS (Figure 4.1.1c). It displays even if the large scale wind is from the south-west (Figure 3.5.2d) the local wind is rather from the south or south-east (Figure 4.1.1c). This small scale effect is most likely associated to the topography around Haukeliseter (Figure 4.2.18).

The orography influences the vertical precipitation pattern. A continuous structure is seen when the wind is south-easterly (up-slope) e.g. on 21 between 9 UTC and 12 UTC (Figure 4.2.8) or 23 December 2016 after 15 UTC (Figure 4.2.10). Westerlies produce disturbed, pulsing patterns with change between intense and less intense snow water content e.g. 24 December 2016 (Figure 4.2.11). As the precipitation profiles in Figures 4.2.8 to 4.2.13a show, are westerlies associated with high snow water content. In comparison continuous precipitation patterns related to south-easterlies have less intense snow water content.

The ensemble variability in Figure 4.2.15 and Figure 4.2.16 shows that the ensemble members are divided between the existence of the exact precipitation pulsing. The variability between the ensemble members for snow water content is smaller ( $\leq 25\%$ ) for precipitation related to south-easterly winds (Figure 4.2.15 and 4.2.16).

The local wind direction influenced the precipitation pattern in the vertical on 21 and 23 December 2016. On both days, weak, south-easterly wind is observed and predicted and led to a continuous precipitation pattern between 9 UTC and 12 UTC on 21 (Figure 4.2.8) and after 15 UTC on 23 December 2016 (Figure 4.2.10). The precipitation is not as intense than for more turbulent precipitation structure e.g. after 15 UTC on 21 December 2016 (Figure 4.2.8a). As Figures 4.2.8 to 4.2.10 indicates the model is able to cover almost the exact timing of the up-slope storm pattern on 21 and 23 December 2016. The variability of each ensemble member initialised on 21 December 2016 is presented in Figure B.2.1a. It shows that almost all ensemble members agree on the occurrence of the storm pattern during 9 UTC to 12 UTC. The same is valid for the initialisations on 22 and 23 December 2016 for the occlusion passage after 15 UTC.

Both days (21 and 23 December 2016) show a moderate precipitation with not as intense snow water content than for precipitation patterns associated with westerlies such as on 24 December 2016 (Figure 4.2.11). High wind speeds from the west and therefore over high mountains (1500 m) followed a pulsing storm pattern with alternating high and low SWC (e.g. 22 and 24 December 2016, Figure 4.2.9 and 4.2.11). MEPS is able to forecast the pulsing pattern for initialisations longer than 24 h prior. This effect might be related to mountain lee wave breaking and result into a turbulent precipitation pattern with pulses of 30 min intense precipitation. More precipitation events need to be studied to understand this effect around the Haukeliseter site. MEPS does not cover all pulses related to west wind during the course of a day. This is related to the short occurrence of the pulses

as well as to the time resolution of MEPS. Since the prediction values exist only every hour the model might miss some of the intense, 30 min precipitation.

As Figure 4.1.8c, d present the correlation between observation and forecasts is low for high wind

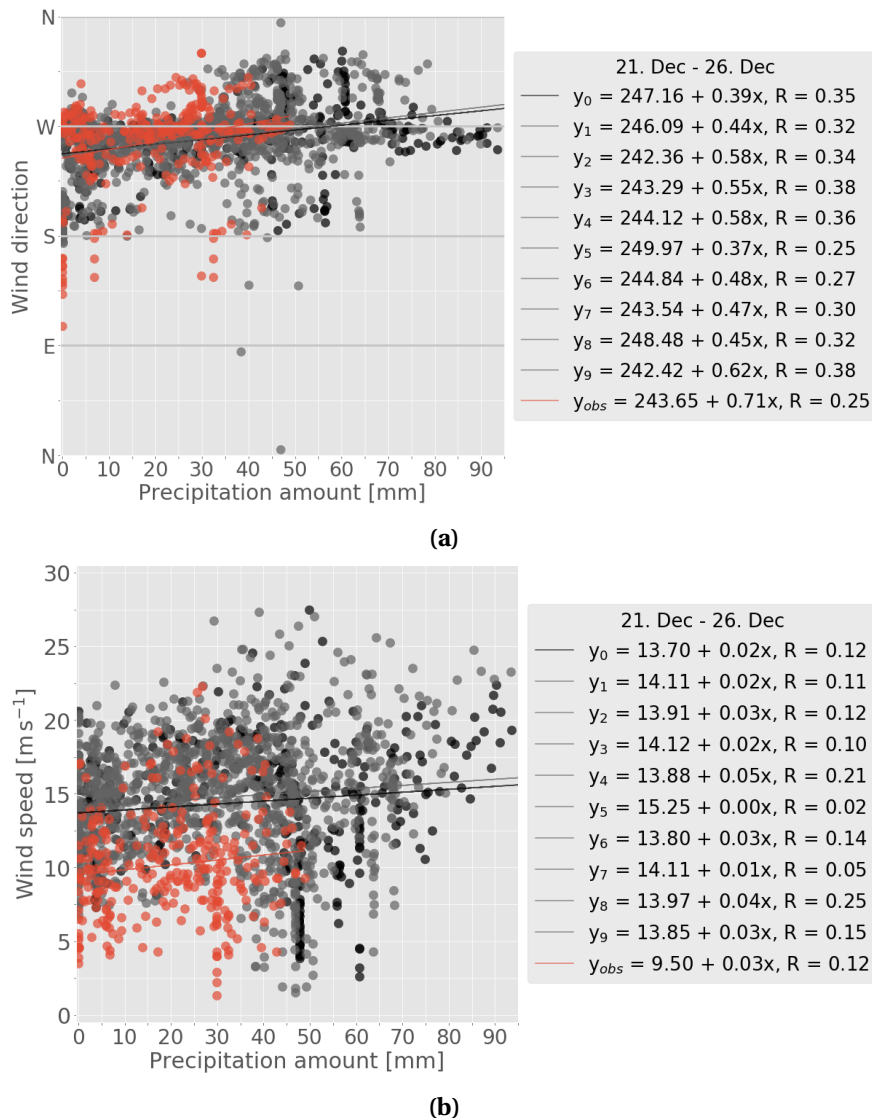


**Figure 4.2.20:** Correlation between surface precipitation amount accumulated over 48 h and a, 10 m wind direction, and b, 10 m wind speed. Red indicating the observations by the double fence and weather mast. Black, the deterministic MEPS forecast and grey, the perturbed ensemble member. The regression line for each correlation and its associated regression coefficient.

speeds. Figure 4.2.20 shows the relation of precipitation amount to wind direction (4.2.20a) and wind speed (4.2.20b). While the wind direction of MEPS has a good agreement, at least for west wind, the wind speed shows larger values over all days (Figure 4.2.20). Müller et al. [2017] already mentioned the bias of too strong wind speed prediction in AROME-MetCoOp.

The surface precipitation amount show 48 h accumulation only up to 50 mm, whereas the model predicts higher surface precipitation amount. The regression between precipitation amount and wind direction shows to be almost the same for observations and MEPS simulations. Weaker 10 m wind speeds are observed than predicted.

High wind speeds might be related to the higher model grid point (1041 m above sea level) than the

Haukeliseter measurement site (991 m above sea level). A difference of 50 m in altitude may lead to the simulation of too high wind speeds. As earlier discussed is the double fence affected by wind (Section 4.2.3). Section 4.2.3 describes the overestimation of surface snow accumulation during the intensification of the extreme storm. MEPS forecast in Figures 4.2.5a to 4.2.5c show more ground accumulation than observed for 24 to 26 December 2016. Aim of this thesis is to analyse if the wind might have had an influence on the surface measurement of the double fence, which could not be shown, even if 10 % under-catch by the double fence gauge is assumed (Table 4.2.4).

During 24 to 26 December 2016 the wind is constantly from the west with higher wind speeds observed (Figure 4.1.4, 4.1.6) than during 21 to 23 December 2016 (Figure 4.1.1, 4.1.3). Figure 4.1.8a and b indicate a better correlation for the observed and forecasted wind directions when precipitation overestimation occurred (24 to 26 December 2016). During 24 and 26 December 2016, observed wind speeds were higher, up to  $20 \text{ m s}^{-1}$ , than on the previous days.

A comparison of the hourly values of MEPS (Figure B.2.1), show neither on 24, 25, and 26 December 2016 high snow amounts up to 3 km compared to the estimated SWC (Figures 4.2.11 to 4.2.13). Figure B.2.1 shows values of very high instantaneous snow water content for individual ensemble members, but no prominent sign of overestimation when the surface simulated too much surface precipitation amount.

The complex terrain and its representation in MEPS might have led to the overestimation of surface precipitation amount between 24 and 26 December 2016. Since the measurement site is closer to the mountain to the west, more precipitation is simulated for the leeward side.

One outcome of the presented study is that MEPS is able to resolve the local topography and predicts the wind direction almost correctly. It did not cover the south-east wind direction on 21 December 2016 (Figure 4.1.1c), which must be related to the local topography.

True prediction of 10 m wind direction (Figures 4.1.1 to 4.1.6c) leads to the correct estimation of frozen precipitation patterns, such as up-slope (south-easterlies) on 21 (Figure 4.2.8) and 23 December 2016 (4.2.10) and pulsing on 22, 24, 25, and 26 December 2016 (westerlies, Figure 4.2.8, 4.2.9, and 4.2.11 to 4.2.13).

This study presents only a first look for a comparison between observations up to 3 km of precipitation to MEPS forecast for an extreme event.

The local effect of pulsing patterns related to westerlies should be examined. To understand if e.g. mountain lee wave breaking occurs at the mountain to the west or if it is an effect of local surface fronts.

The deterministic forecast could be perturbed in another way. Different perturbations might lead to a better correlation between 10 m wind and precipitation amount observation and MEPS forecast at the surface. The choice of using the closest grid point to Haukeliseter might not have been the best approach and must be investigated further.

As Müller et al. [2017] pointed out, higher wind speeds are in general better forecasted in AROME-MetCoOp than in ECMWF. The improved representation of surface parameters, 24 h prior, in the fine-scale model MEPS is important when warnings are send out by the meteorological services for extreme weather events. This is an advantage for fine-scale forecast models, especially in Norway, where the topography changes from sea to mountainous terrain on small spatial scale.



## CHAPTER 5: SUMMARY AND OUTLOOK

In this thesis, a case study of an extreme event occurring on 21 to 26 December 2016 was studied. The Christmas storm in 2016, affected large parts of Eastern, Southern, and Western Norway. The Meteorological Cooperation on Operational Numerical Weather Prediction (MetCoOp) Ensemble Prediction system (MEPS) became operational from November 2016 when it substituted the Météo-France Applications of Research to Operations at MEscale (AROME)-MetCoOp system at the Norwegian Meteorological Institute. The meteorological measurement site Haukeliseter (991 m above sea level) was equipped additionally with instruments such as a Micro Rain Radar (MRR), Particle Imaging Package (PIP), and Multi-Angular Snowfall Camera (MASC), during winter 2016/2017. Since MEPS has just become operational, a unique opportunity was given comparing observations from the World Meteorological Organization station Haukeliseter, and the Norwegian weather forecast model.

The 2016 Christmas storm was analysed with the help of ECMWF analysis from the surface to the dynamic tropopause level. Meteorological parameters were evaluated to prove if consistent large-scale phenomena were observed and predicted by MEPS. A sensitivity study of retrieved surface snow accumulation for different a-priori assumptions was implemented. Snow comparison between double fence gauge observations, retrieved profiles of snow water content, and MEPS forecasts were carried out for the World Meteorological Organization measurement site Haukeliseter. Furthermore, a comparison between and MEPS forecast was carried out.

During 21 to 26 December 2016 a low-pressure system developed east of Iceland propagating poleward, followed by a second low-pressure system, which evolved in the western Atlantic, moving eastward. Temperature changes related to a low and high tropopause, occlusions, and warm sector passages led to precipitation changes at Haukeliseter. Within the warm sector passage liquid precipitation was observed at Haukeliseter, followed by a landfall of the Christmas storm on 26 December 2016 and dissipation afterwards.

The regional forecast model MEPS is capable of predicting sea level pressure, 2 m air temperature, and 10 m wind changes associated to frontal passages and occlusions during the Christmas 2016 storm at Haukeliseter. Transitions of the occlusions and the warm sector were predicted 24 h and 48 h in advance for this particular case. However, MEPS simulated too high wind speed (mean absolute error up to  $10 \text{ m s}^{-1}$ ) and surface precipitation amount (mean absolute error up to 15 mm).

According to literature the double fence gauge instrument is one of the best surface measurements for snow and taken as reference norm for precipitation observations. A state of the art optimal estimation snowfall retrieval using a-priori guess from MRR, PIP, and MASC, allowed to compare

surface observations to vertically retrieved snow amounts.

In the sensitivity study assumptions of a particle model for rimed aggregates ('B6'), climatological particle size distributions (PSD) and fall speeds followed the best estimate for surface snowfall accumulation compared to the use of a less reflective CloudSat aggregate model ('B8') at Haukeliseter. The results revealed a 70 % bias for CloudSat aggregate particle model and particle size distribution compared to double fence gauge measurements on 22 December 2016.

Using particle model assumptions for rimed aggregates led to small differences between observed and estimated snow ( $\leq -5\%$ ) and show the importance to choose a priori assumptions correctly to achieve reasonable surface estimates of precipitation amount at the ground. The small deviation gives confidence to trust the vertical estimated snow water content.

The average difference between observations and forecasted precipitation amount at the surface decreased with increasing lead time (12 h: +135 %, 24 h: +33 %) for 21 to 26 December 2016. However, inspecting the temporal evolution in detail revealed that the average difference for 12 h and 24 h accumulation was less than +11 % for 21 to 23 December 2016 and +60 % for 24 to 26 December 2016. Additionally, taking the 10 % negative bias of the double fence measurements due to wind effects into account, reduces the forecasted surface snow error to +40 %.

On 25 December 2016, MASC images allowed to verify the presence of liquid precipitation during the passage of a warm sector at Haukeliseter. MEPS was able to simulate the timing of liquid precipitation 24 h and 48 h in advance. Comparison between MRR reflectivity profiles and modelled liquid water content showed the accurate simulation of liquid precipitation, both in time and thickness layer, in the lower most atmosphere.

More variability ( $\geq 50\%$ ) between the ensemble members for the short, pulsed than for continuous precipitation patterns. Less variability ( $\leq 25\%$ ) of snow water content between the ensemble members was simulated for the continues precipitation associated with south-easterlies for initialisations 24 h and 48 h prior, in contrast MEPS ensemble members agreed about the appearance of pulsing snowfall patterns related to westerlies, but not the timing. The coefficient of variation showed more variability ( $\geq 50\%$ ) between the ensemble members for the short, pulsed than for continuous precipitation pattern. The larger variability of the ensemble members for the pulsing storm patterns is likely related to the temporal resolution of MEPS ensemble forecast data and the short appearance of the pulses of around 30 min.

The hourly averaged estimated snow water content from MRR profiles is larger ( $\leq 1.5 \text{ gm}^{-3}$ ) than the ensemble mean of instantaneous MEPS forecasts ( $\leq 1.2 \text{ gm}^{-3}$ ). In contrast the deterministic and first ensemble member with 1 h resolution predicted higher snow water content ( $\geq 2.0 \text{ gm}^{-3}$ ) compared to the retrieved values ( $\leq 1.5 \text{ gm}^{-3}$ ) during the 2016 Christmas storm, showing the importance of high temporal resolution.

Finally, topographic influence on wind and precipitation next to the impact of horizontal resolution of MEPS were discussed. Although MEPS has a high horizontal resolution of 2.5 km, the representation of the topography in Norway might still be an issue. MEPS resolves some of the major orographic patterns at the Haukeliseter station, such as high mountains to the west and the south-east. The one and three hourly ensemble mean forecast of snow water

content displayed the ability to predict more continuous, up-slope snow storm patterns related to occlusion passages as well as pulsing precipitation associated to strong westerlies. Additionally the forecasts of westerlies during 24 and 26 December 2016 showed a good correlation with observations. In contrast, observed south-easterly winds were predicted as south-westerly wind on 21 and 23 December 2016.

The here presented results are a first case study for one winter storm at a Norwegian station in the mountain. Further studies have to be carried out to verify the results.

## 5.1 OUTLOOK

Only a few studies have addressed similar approaches like this study here by comparing snow observations with weather forecast models.

First and foremost, it is important to investigate more extreme storm events during winter at Haukeliseter, whether the deviations between observed and retrieved surface snow accumulation stay small. Furthermore, these results should be verified different stations in Norway with similar polar tundra climate, to investigate if the a-priori assumptions can be generalised for a similar local climate.

It is important to have correct measurements such as the double fence gauge or the radar-particle size distribution retrieval approach. The double fence gauge observations should be investigated further to understand the wind related under-catchment of surface precipitation. Correct measurements will help to improve initial conditions for weather forecast models. Furthermore, accurate observations will help to get a better understanding of snowfall.

Even though MEPS performed well in the vertical by simulating the wind to the storm structure correctly, it will be interesting to investigate the presented results with a higher time resolution to resolve the short pulses. This will help to investigate the simulation of high snow amount at the surface and the relationship between the surface and vertical forecast column.

Sensitivity studies for the outer boundary model could help to understand the influence of European Centre for Medium-Range Weather Forecasts (ECMWF) analysis input data on the MEPS predictions. An initialisation with and without all available observations inside ECMWF will help to investigate the boundary and initial state influence on the wind and precipitation predictions in MEPS.

Finally, more case studies will also help to get a better estimate about the performance of MEPS for snow prediction during winter storm events. The mean absolute error for the 12 h accumulation of precipitation revealed large variability depending on the initialisation time of MEPS and the state of the cyclone.

---

## LIST OF ABBREVIATIONS

<b>ACC</b>	Accretion
<b>AGG</b>	Aggregation
<b>AR</b>	Atmospheric River
<b>AROME</b>	Applications of Research to Operations at Mesoscale
<b>AUT</b>	Autoconversion
<b>BER</b>	Bergeron-Findeisen process
<b>C3VP</b>	Canadian CloudSat-CALIPSO Validation Project
<b>CFR</b>	Contact Freezing of Raindrops
<b>CPR</b>	Cloud Profiling Radar
<b>CV</b>	Coefficient of Variation
<b>CVM</b>	Conversion-melting
<b>DDA</b>	Discrete Dipole Approximation
<b>DEP</b>	Deposition
<b>DRY</b>	Dry processes
<b>DT</b>	Dynamic Tropopause
<b>ECMWF</b>	European Centre for Medium-Range Weather Forecasts
<b>EPS</b>	Ensemble Prediction System
<b>FMI</b>	Finnish Meteorological Institute
<b>HEN</b>	Heterogeneous Nucleation
<b>HON</b>	Homogeneous Nucleation
<b>IVT</b>	Integrated Vapour Transport
<b>LWC</b>	Liquid Water Content

<b>MASC</b>	Multi-Angular Snowfall Camera
<b>MEPS</b>	MetCoOp Ensemble Prediction System
<b>Meso-NH</b>	Mesoscale Non-Hydrostatic model
<b>Met-Norway</b>	Norwegian Meteorological Institute
<b>MetCoOp</b>	Meteorological Co-operation on Operational NWP
<b>MLT</b>	Melting
<b>MRR</b>	Micro Rain Radar
<b>MSLP</b>	Mean Sea Level Pressure
<b>NSF</b>	National Science Foundation
<b>NWP</b>	Numerical Weather Prediction
<b>PIP</b>	Precipitation Imaging Package
<b>PSD</b>	Particle Size distribution
<b>RIM</b>	Riming
<b>SMHI</b>	Swedish Meteorological and Hydrological Institute
<b>SWC</b>	Snow Water Content
<b>SWP</b>	Snow Water Path
<b>WCB</b>	Warm Conveyor Belt
<b>WET</b>	Wet processes
<b>WMO</b>	World Meteorological Organization

## REFERENCES

- Azad, R. and Sorteberg, A. Extreme daily precipitation in coastal western Norway and the link to atmospheric rivers. *Journal of Geophysical Research: Atmospheres*, 122(4):2080–2095, January 2017. ISSN 2169-8996. doi: 10.1002/2016JD025615. URL <https://agupubs.onlinelibrary.wiley.com/doi/abs/10.1002/2016JD025615>.
- Barnett, T. P., Adam, J. C., and Lettenmaier, D. P. Potential impacts of a warming climate on water availability in snow-dominated regions. *Nature*, 438(7066):303–309, November 2005. ISSN 1476-4687. doi: 10.1038/nature04141. URL <https://www.nature.com/articles/nature04141>.
- Buizza, R., Hollingsworth, A., Lalaurette, F., and Ghelli, A. Probabilistic Predictions of Precipitation Using the ECMWF Ensemble Prediction System. *Wea. Forecasting*, 14(2):168–189, April 1999. ISSN 0882-8156. doi: 10.1175/1520-0434(1999)014<0168:PPOPUT>2.0.CO;2. URL <https://journals.ametsoc.org/doi/full/10.1175/1520-0434%281999%29014%3C0168%3APP0PUT%3E2.0.CO%3B2>.
- Caniaux, G., Redelsperger, J.-L., and Lafore, J.-P. A Numerical Study of the Stratiform Region of a Fast-Moving Squall Line. Part I: General Description and Water and Heat Budgets. *J. Atmos. Sci.*, 51(14):2046–2074, July 1994. ISSN 0022-4928. doi: 10.1175/1520-0469(1994)051<2046:ANSOTS>2.0.CO;2. URL [https://journals.ametsoc.org/doi/abs/10.1175/1520-0469\(1994\)051%3C2046:ANSOTS%3E2.0.CO;2](https://journals.ametsoc.org/doi/abs/10.1175/1520-0469(1994)051%3C2046:ANSOTS%3E2.0.CO;2).
- Christensen, M. W., Behrangi, A., L'ecuyer, T. S., Wood, N. B., Lebsack, M. D., and Stephens, G. L. Arctic Observation and Reanalysis Integrated System: A New Data Product for Validation and Climate Study. *Bull. Amer. Meteor. Soc.*, 97(6):907–916, January 2016. ISSN 0003-0007. doi: 10.1175/BAMS-D-14-00273.1. URL <https://journals.ametsoc.org/doi/10.1175/BAMS-D-14-00273.1>.
- Cooper, S. J., Wood, N. B., and L'Ecuyer, T. S. A variational technique to estimate snowfall rate from coincident radar, snowflake, and fall-speed observations. *Atmos. Meas. Tech.*, 10(7):2557–2571, July 2017. ISSN 1867-8548. doi: 10.5194/amt-10-2557-2017. URL <https://www.atmos-meas-tech.net/10/2557/2017/>.
- Dahlgren, P. A Comparison Of Two Large Scale Blending Methods. page 16, 2013. URL <http://metcoop.org/memo/2013/02-2013-METCOOP-MEMO.PDF>.
- Dando, P. Introducing the octahedral reduced Gaussian grid, June 2016. URL <https://software.ecmwf.int/wiki/display/FCST/Gaussian+grids>.
- Doviak, R. J. and Zrnic, D. S. *Doppler Radar and Weather Observations*. Courier Corporation, 1993. ISBN 978-0-486-45060-5. Google-Books-ID: [ispLkPX9n2UC](#).
- eklma. Norwegian Meteorological Institute, 2016. URL <http://sharki.oslo.dnmi.no/>

- portal/page?\_pageid=73,39035,73\_39049&\_dad=portal&\_schema=PORTAL. Last visited on 12/02/2018.
- Færaas, A., Rommetveit, A., Duesund, J., and Senel, E. Urd har nådd orkan styrke flytter seg mot østlandet, December 2016. URL [http://www.yr.no/artikkel/\\_urd\\_-har-nadd-orkan-styrke\\_-\\_flytter-seg-mot-ostlandet-1.13292245](http://www.yr.no/artikkel/_urd_-har-nadd-orkan-styrke_-_flytter-seg-mot-ostlandet-1.13292245). Last visited on 04/02/2018.
- Farestveit, E. 80.000 mista radioen under ekstremæret, December 2016. URL <https://www.nrk.no/hordaland/80.000-mista-radioen-under-ekstremveret-1.13294980>. Last visited on 21/02/2018.
- Field, C. B., Barros, V. R., Dokken, D. J., Mach, K. J., Mastrandrea, M. D., Bilir, T. E., Chatterjee, M., Ebi, K. L., Estrada, Y. O., Genova, R. C., Girma, B., Kissel, E. S., Levy, A. N., MacCracken, S., Mastrandrea, P. R., and White, L. L. Summary for policymakers. In: Climate Change 2014: Impacts, Adaptation, and Vulnerability. Part A: Global and Sectoral Aspects. Contribution of Working Group II to the Fifth Assessment Report of the Intergovernmental Panel on Climate Change. Cambridge: Cambridge University Press, page 34, 2014.
- Foote, G. B. and Du Toit, P. S. Terminal Velocity of Raindrops Aloft. *J. Appl. Meteor.*, 8(2):249–253, April 1969. ISSN 0021-8952. doi: 10.1175/1520-0450(1969)008<0249:TVORA>2.0.CO;2. URL <https://journals.ametsoc.org/doi/10.1175/1520-0450%281969%29008%3C0249%3ATVORA%3E2.0.CO%3B2>.
- Garrett, T. J., Fallgatter, C., Shkurko, K., and Howlett, D. Fall speed measurement and high-resolution multi-angle photography of hydrometeors in free fall. *Atmos. Meas. Tech.*, 5(11):2625–2633, November 2012. ISSN 1867-8548. doi: 10.5194/amt-5-2625-2012. URL <https://www.atmos-meas-tech.net/5/2625/2012/>.
- Geonor Inc. T-200b All Weather Precipitation – Rain Gauge, 2015. URL <http://geonor.com/live/products/weather-instruments/t-200b-weather-precipitation-rain-gauge/>.
- Geonorge. DTM 10 Terrengmodell (UTM33) - Kartverket - Kartkatalogen, May 2018. URL <https://kartkatalog.geonorge.no/metadata/uuid/dddbb667-1303-4ac5-8640-7ec04c0e3918>.
- Goodison, B. E., Louie, P. Y. T., and Yang, D. WMO Solid Precipitation Measurement Intercomparison: Final Report. Instruments and Observing Methods Rep. 67, WMO/TD-No. 872,. World Meteorological Organization, Geneva, Switzerland, page 318, 1998.
- Gowan, T. M., Steenburgh, W. J., and Schwartz, C. S. Validation of Mountain Precipitation Forecasts from the Convection-Permitting NCAR Ensemble and Operational Forecast Systems over the Western United States. *Wea. Forecasting*, 33(3):739–765, June 2018. ISSN 0882-8156, 1520-0434. doi: 10.1175/WAF-D-17-0144.1. URL <http://journals.ametsoc.org/doi/10.1175/WAF-D-17-0144.1>.
- Hansen, B. B., Isaksen, K., Benestad, R. E., Kohler, J., Pedersen, Ø. Ø., Loe, L. E., Coulson, S. J., Larsen, J. O., and Varpe, Ø. Warmer and wetter winters: characteristics and implications of an extreme weather event in the High Arctic. *Environ. Res. Lett.*, 9(11):114021, 2014. ISSN 1748-9326. doi: 10.1088/1748-9326/9/11/114021. URL <http://stacks.iop.org/1748-9326/9/i=11/a=114021>.
- Hollingsworth, A. An experiment in monte carlo forecasting. In *Workshop on Stochastic Dynamic Forecasting, 17-19 October 1979*, pages 65–85, Shinfield Park, Reading, 1979. ECMWF, ECMWF.

- Homleid, M. and Tveter, F. T. Verification of operational weather prediction models september to november 2015. *METInfo Rep.*, 16:2016, 2016. URL [https://www.met.no/publikasjoner/met-info/met-info-2016/\\_attachment/download/b0463915-cba0-42ac-8539-4233ae2bf01c:3d71565a27f88085373199a33ab8569151c144e9/MET-info-22-2016.pdf](https://www.met.no/publikasjoner/met-info/met-info-2016/_attachment/download/b0463915-cba0-42ac-8539-4233ae2bf01c:3d71565a27f88085373199a33ab8569151c144e9/MET-info-22-2016.pdf).
- Hudak, D., Barker, H., Rodriguez, P., and Donovan, D. The Canadian CloudSat Validation Project. *4th ERAD*, September 2006. URL <http://www.crahi.upc.edu/ERAD2006/proceedingsMask/00165.pdf>. Barcelona, Spain.
- Hurrell, J. W. Decadal Trends in the North Atlantic Oscillation: Regional Temperatures and Precipitation. *Science*, 269(5224):676–679, August 1995. ISSN 0036-8075, 1095-9203. doi: 10.1126/science.269.5224.676. URL <http://science.sciencemag.org/content/269/5224/676>.
- Joos, H. and Wernli, H. Influence of microphysical processes on the potential vorticity development in a warm conveyor belt: a case-study with the limited-area model COSMO. *Q. J. Royal Meteorol. Soc.*, 138(663):407–418, January 2012. ISSN 00359009. doi: 10.1002/qj.934. URL <http://doi.wiley.com/10.1002/qj.934>.
- Kalnay, E. *Atmospheric modeling, data assimilation and predictability*. Cambridge University Press, Cambridge, 2003. ISBN 978-0-521-79179-3.
- Kartverket. Norgeskart, November 2018. URL [http://www.norgeskart.no/?\\_ga=2.7509489.291164698.1524482471-1352211079.1517515119#!?project=se eiendom&layers=1002,1015&zoom=4&lat=7197864.00&lon=396722.00](http://www.norgeskart.no/?_ga=2.7509489.291164698.1524482471-1352211079.1517515119#!?project=se eiendom&layers=1002,1015&zoom=4&lat=7197864.00&lon=396722.00).
- Kochendorfer, J., Nitu, R., Wolff, M., Mekis, E., Rasmussen, R., Baker, B., Earle, M. E., Reverdin, A., Wong, K., Smith, C. D., Yang, D., Roulet, Y.-A., Buisan, S., Laine, T., Lee, G., Aceituno, J. L. C., Alastraú, J., Isaksen, K., Meyers, T., Brækkan, R., Landolt, S., Jachcik, A., and Poikonen, A. Analysis of single-Alter-shielded and unshielded measurements of mixed and solid precipitation from WMO-SPICE. *Hydrol. Earth Syst. Sci.*, 21(7):3525–3542, July 2017. ISSN 1607-7938. doi: 10.5194/hess-21-3525-2017. URL <https://www.hydrol-earth-syst-sci.net/21/3525/2017/>.
- Køltzow, M. A. Ø. Spin-up time of MEPS. Private Communication, 2018.
- Kulie, M. S. and Bennartz, R. Utilizing Spaceborne Radars to Retrieve Dry Snowfall. *J. Appl. Meteor. Climatol.*, 48(12):2564–2580, January 2009. ISSN 1558-8424. doi: 10.1175/2009JAMC2193.1. URL <http://journals.ametsoc.org/doi/abs/10.1175/2009JAMC2193.1>.
- Kulie, M. S., Milani, L., Wood, N. B., Tushaus, S. A., Bennartz, R., and L'Ecuyer, T. S. A Shallow Cumuliform Snowfall Census Using Spaceborne Radar. *J. Hydrometeor.*, 17(4):1261–1279, February 2016. ISSN 1525-755X. doi: 10.1175/JHM-D-15-0123.1. URL <https://journals.ametsoc.org/doi/abs/10.1175/JHM-D-15-0123.1>.
- Køltzow, M. A. MetCoOp EPS - A convection permitting ensemble prediction system, October 2017.
- L'Ecuyer, T. S. AOS 441 - Satellite and Radar Meteorology. Last visited on 15/10/2017, January 2017. URL <https://lecuyer.aos.wisc.edu/aos441>.
- Liu G. Deriving snow cloud characteristics from CloudSat observations. *J. Geophys. Res. Atmos.*, 113(D8), September 2008. ISSN 0148-0227. doi: 10.1029/2007JD009766. URL <https://agupubs.onlinelibrary.wiley.com/doi/abs/10.1029/2007JD009766>.

- Lorenz, E. N. Atmospheric Predictability as Revealed by Naturally Occurring Analogues. *J. Atmos. Sci.*, 26(4):636–646, July 1969. ISSN 0022-4928. doi: 10.1175/1520-0469(1969)26<636:APARBN>2.0.CO;2. URL <https://journals.ametsoc.org/doi/abs/10.1175/1520-0469%281969%2926%3C636%3AAPARBN%3E2.0.CO%3B2>.
- Markowski, P. and Richardson, Y. *Mesoscale Meteorology in Midlatitudes*. John Wiley & Sons, September 2011. ISBN 978-1-119-96667-8. Google-Books-ID: MDeYosfLLEYC.
- Martin, J. E. *Mid-Latitude Atmospheric Dynamics: A First Course*. Wiley, May 2006. ISBN 978-0-470-86466-1.
- McCumber, M., Tao, W.-K., Simpson, J., Penc, R., and Soong, S.-T. Comparison of Ice-Phase Microphysical Parameterization Schemes Using Numerical Simulations of Tropical Convection. *J. Appl. Meteor.*, 30(7):985–1004, July 1991. ISSN 0894-8763. doi: 10.1175/1520-0450-30.7.985. URL <https://journals.ametsoc.org/doi/abs/10.1175/1520-0450-30.7.985>.
- Meehl, G. A., Karl, T., Easterling, D. R., Changnon, S., Pielke, R., Changnon, D., Evans, J., Groisman, P. Y., Knutson, T. R., Kunkel, K. E., Mearns, L. O., Parmesan, C., Pulwarty, R., Root, T., Sylves, R. T., Whetton, P., and Zwiers, F. An Introduction to Trends in Extreme Weather and Climate Events: Observations, Socioeconomic Impacts, Terrestrial Ecological Impacts, and Model Projections. *Bull. Amer. Meteor. Soc.*, 81(3):413–416, March 2000. ISSN 0003-0007. doi: 10.1175/1520-0477(2000)081<0413:AITTIE>2.3.CO;2. URL [https://journals.ametsoc.org/doi/abs/10.1175/1520-0477\(2000\)081%3C0413:AITTIE%3E2.3.CO;2](https://journals.ametsoc.org/doi/abs/10.1175/1520-0477(2000)081%3C0413:AITTIE%3E2.3.CO;2).
- MetCoOp Wiki. Description of MEPS, December 2017. URL <https://metcoop.smhi.se/dokuwiki/nwp/metcoop/>. Last visited on 26/12/2017.
- METEK, M. M. G. Micro Rain Radar MRR-2, October 2010. URL <http://metek.de/wp-content/uploads/2014/05/Metek-Micro-Rain-Radar-MRR-2-Datasheet.pdf>.
- Meteo France. The Meso-NH Atmospheric Simulation System: Scientific Documentation, Part III: Physics, January 2009.
- Meteorologene. "Her kommer #Urd! Selve Lavtrykksenteret treffer Møre og Romsdal, men den sterkeste vinden kommer sør for Stad. #SørNorge" 26 December 2016, 9:34am, 2016. URL <https://twitter.com/Meteorologene>. Last visited on 21/02/2018.
- Moore, R. Large-scale dynamics inducing atmospheric rivers and extreme precipitation over norway. unpublished.
- Müller, M., Homleid, M., Ivarsson, K.-I., Køltzow, M. A. Ø., Lindskog, M., Midtbø, K. H., Andrae, U., Aspelien, T., Berggren, L., Bjørge, D., Dahlgren, P., Kristiansen, J., Randriamampianina, R., Ridal, M., and Vignes, O. AROME-MetCoOp: A Nordic Convective-Scale Operational Weather Prediction Model. *Wea. Forecasting*, 32(2):609–627, January 2017. ISSN 0882-8156. doi: 10.1175/WAF-D-16-0099.1. URL [http://journals.ametsoc.org/doi/abs/10.1175/WAF-D-16-0099.1](https://journals.ametsoc.org/doi/abs/10.1175/WAF-D-16-0099.1).
- Newman, A. J., Kucera, P. A., and Bliven, L. F. Presenting the Snowflake Video Imager (SVI). *J. Atmos. Oceanic Technol.*, 26(2):167–179, February 2009. ISSN 0739-0572. doi: 10.1175/2008JTE-CHA1148.1. URL <https://journals.ametsoc.org/doi/abs/10.1175/2008JTECHA1148.1>.
- Nielsen-Gammon, J. W. A Visualization of the Global Dynamic Tropopause. *Bull. Amer. Meteor. Soc.*, 82(6):1151–1168, June 2001. ISSN 0003-0007. doi: 10.1175/1520-0477(2001)082<1151:AVOTGD>2.3.CO;2. URL [https://journals.ametsoc.org/doi/abs/10.1175/1520-0477\(2001\)082%3C1151:AVOTGD%3E2.3.CO;2](https://journals.ametsoc.org/doi/abs/10.1175/1520-0477(2001)082%3C1151:AVOTGD%3E2.3.CO;2).

- Nitu, R. and Wong, K. CIMO survey on national summaries of methods and instruments for solid precipitation measurement at automatic weather stations,. Technical Report 102, World Meteorological Organization,, Geneva, Switzerland, 2010.
- NOAA. ETOPO1 Global Relief, 2017. URL <https://www.ngdc.noaa.gov/mgg/global/global.html>.
- Noh, Y.-J., Liu, G., Seo, E.-K., Wang, J. R., and Aonashi, K. Development of a snowfall retrieval algorithm at high microwave frequencies. *J. Geophys. Res.*, 111(D22), November 2006. ISSN 2156-2202. doi: 10.1029/2005JD006826. URL <https://agupubs.onlinelibrary.wiley.com/doi/abs/10.1029/2005JD006826>.
- Norin, L., Devasthale, A., L'Ecuyer, T. S., Wood, N. B., and Smalley, M. Intercomparison of snowfall estimates derived from the CloudSat Cloud Profiling Radar and the ground-based weather radar network over Sweden. *Atmos. Meas. Tech.*, 8(12):5009–5021, December 2015. ISSN 1867-8548. doi: 10.5194/amt-8-5009-2015. URL <https://www.atmos-meas-tech.net/8/5009/2015/>.
- Norwegian Meteorological Institute. MET Norway Thredds Service, 2016. URL <http://thredds.met.no/thredds/catalog/meps25epsarchive/catalog.html>. Last visited on 27/01/2018.
- Olsen, A.-M. and Granerød, M. Ekstremværrapport. Hendelse: Urd 26. desember met.info. no. 18/2017 ISSN X METEOROLOGI Bergen, - PDF, September 2017. URL <http://docplayer.me/48734203-Ekstremvaerrapport-hendelse-urd-26-desember-met-info-no-18-2017-issn-x-meteorologi-bergen.html>. Last visited on 11/10/2017.
- Owens, R. G. and Hewson, T. D. ECMWF Forecast User Guide. 2018. doi: 10.21957/m1cs7h.
- Palerme, C., Kay, J. E., Genthon, C., L'Ecuyer, T., Wood, N. B., and Claud, C. How much snow falls on the Antarctic ice sheet? *The Cryosphere*, 8(4):1577–1587, August 2014. ISSN 1994-0424. doi: 10.5194/tc-8-1577-2014. URL <https://www.the-cryosphere.net/8/1577/2014/>.
- Palerme, C., Genthon, C., Claud, C., Kay, J. E., Wood, N. B., and L'Ecuyer, T. Evaluation of current and projected Antarctic precipitation in CMIP5 models. *Clim. Dyn.*, 48(1-2):225–239, January 2017. ISSN 0930-7575, 1432-0894. doi: 10.1007/s00382-016-3071-1. URL <https://link.springer.com/article/10.1007/s00382-016-3071-1>.
- Pedersen, K. and Rommetveit, A. Hva er et ekstremvær?, November 2013. URL [http://www.yr.no/artikkel/hva-er-et-ekstremvaer\\_-1.7890946](http://www.yr.no/artikkel/hva-er-et-ekstremvaer_-1.7890946). Last visited on 04/02/2018.
- Peel, M. C., Finlayson, B. L., and McMahon, T. A. Updated world map of the Köppen-Geiger climate classification. *Hydrology and Earth System Sciences Discussions*, 4(2):439–473, March 2007. URL <https://hal.archives-ouvertes.fr/hal-00298818>.
- Petroliagis, T., Buizza, R., Lanzinger, A., and Palmer, T. N. Potential use of the ECMWF Ensemble Prediction System in cases of extreme weather events. *Meteorological Applications*, 4(1):69–84, March 1997. ISSN 1469-8080, 1350-4827. URL <https://www.cambridge.org/core/journals/meteorological-applications/article/potential-use-of-the-ecmwf-ensemble-prediction-system-in-cases-of-extreme-weather-events/C63050704CB35CD43BC4E5998A390DDC>.
- Pinty, J.-P. and Jabouille, P. A mixed-phased cloud parameterization for use in a mesoscale non-hydrostatic model: Simulations of a squall line and of orographic precipitation. pages 217–220. Amer. Meteor. Soc., 1998.

- Rinehart, R. E. *Radar for Meteorologists: Or You, Too, Can be a Radar Meteorologist*. Rinehart Publications, 2010. ISBN 978-0-9658002-3-5. Google-Books-ID: VqatcQAACAAJ.
- Rutz, J. J., Steenburgh, W. J., and Ralph, F. M. Climatological Characteristics of Atmospheric Rivers and Their Inland Penetration over the Western United States. *Mon. Wea. Rev.*, 142(2):905–921, January 2014. ISSN 0027-0644. doi: 10.1175/MWR-D-13-00168.1. URL <http://journals.ametsoc.org/doi/abs/10.1175/MWR-D-13-00168.1>.
- Ruud, S., Carr Ekroll, H., Bakke Foss, A., Torgersen, H. O., and Annar Holm, P. To tonn tungt skilt blåste ned da ekstremværet traff Oslo og Østlandet i natt, December 2016. URL <https://www.aftenposten.no/article/ap-2z6wy.html>. Last visited on 21/02/2018.
- Schirle, C. Characterization of snowfall at high latitudes using an optimal estimation-based retrieval algorithm. Private Communication, 2018.
- Seity, Y., Brousseau, P., Malardel, S., Hello, G., Bénard, P., Bouttier, F., Lac, C., and Masson, V. The AROME-France Convective-Scale Operational Model. *Mon. Wea. Rev.*, 139(3):976–991, October 2010. ISSN 0027-0644. doi: 10.1175/2010MWR3425.1. URL <https://journals.ametsoc.org/doi/abs/10.1175/2010MWR3425.1>.
- Shi, W., L'Heureux, M., and Halpert, M. Climate Diagnostics Bulletin - December 2016, Near Real-Time Ocean/Atmosphere: Monitoring, Assessments, and Prediction. Technical report, Climate Prediction Center, 2016. URL [http://origin.cpc.ncep.noaa.gov/products/CDB/CDB\\_Archive\\_pdf/PDF/CDB.dec2016\\_color.pdf](http://origin.cpc.ncep.noaa.gov/products/CDB/CDB_Archive_pdf/PDF/CDB.dec2016_color.pdf).
- Simmons, A. J. and Burridge, D. M. An Energy and Angular-Momentum Conserving Vertical Finite-Difference Scheme and Hybrid Vertical Coordinates. *Mon. Wea. Rev.*, 109(4):758–766, April 1981. ISSN 0027-0644. doi: 10.1175/1520-0493(1981)109<0758:AEAAMC>2.0.CO;2. URL <https://journals.ametsoc.org/doi/10.1175/1520-0493%281981%29109%3C0758%3AAEAAMC%3E2.0.CO%3B2>.
- Skofronick-Jackson, G. M., Kim, M.-J., Weinman, J. A., and Chang, D.-E. A physical model to determine snowfall over land by microwave radiometry. *IEEE Geosci. Remote Sens. Lett.*, 42(5): 1047–1058, May 2004. ISSN 0196-2892. doi: 10.1109/TGRS.2004.825585.
- Stephens, G. L. *Remote Sensing of the Lower Atmosphere: An Introduction*. Oxford University Press, 1994. ISBN 978-0-19-508188-6. Google-Books-ID: 2FcRAQAAIAAJ.
- Stocker, T. F., Qin, D., Plattner, G.-K., Tignor, M. M. B., Allen, S. K., Boschung, J., Nauels, A., Xia, Y., Bex, V., and Midgley, P. M. Working Group I Contribution to the Fifth Assessment Report of the Intergovernmental Panel on Climate Change. *Cambridge: Cambridge University Press*, page 14, 2013.
- Sun, J. Convective-scale assimilation of radar data: progress and challenges. *Quarterly Journal of the Royal Meteorological Society*, 131(613):3439–3463, 2005. ISSN 1477-870X. doi: 10.1256/qj.05.149. URL <https://rmets.onlinelibrary.wiley.com/doi/abs/10.1256/qj.05.149>.
- Uvo, C. B. Analysis and regionalization of northern European winter precipitation based on its relationship with the North Atlantic oscillation. *International Journal of Climatology*, 23(10):1185–1194, July 2003. ISSN 1097-0088. doi: 10.1002/joc.930. URL <https://rmets.onlinelibrary.wiley.com/doi/abs/10.1002/joc.930>.
- Warner, T. T., Peterson, R. A., and Treadon, R. E. A Tutorial on Lateral Boundary Conditions as a Basic and Potentially Serious Limitation to Regional Numerical Weather Prediction. *Bull.*

- Amer. Meteor. Soc.*, 78(11):2599–2618, November 1997. ISSN 0003-0007. doi: 10.1175/1520-0477(1997)078<2599:ATOLBC>2.0.CO;2. URL [https://journals.ametsoc.org/doi/abs/10.1175/1520-0477\(1997\)078%3C2599:ATOLBC%3E2.0.CO%3B2](https://journals.ametsoc.org/doi/abs/10.1175/1520-0477(1997)078%3C2599:ATOLBC%3E2.0.CO%3B2).
- Wolff, M. A. WMO Solid Precipitation Intercomparison Experiment (WMO-SPICE), Ch. 4.2.4 Precipitation measurements in areas with high winds and/or complex terrain. unpublished.
- Wolff, M. A., Brækkan, R., Isaksen, K., and Ruud, E. A new testsite for wind correction of precipitation measurements at a mountain plateau in southern Norway. In *Proceedings of WMO Technical Conference on Meteorological and Environmental Instruments and Methods of Observation (TECO–2010). Instruments and Observing Methods Report*, 2010.
- Wolff, M. A., Isaksen, K., Braekkan, R., Alfnæs, E., Petersen-Øverleir, A., and Ruud, E. Measurements of wind-induced loss of solid precipitation: description of a Norwegian field study. *Hydrol. Res.*, 44(1):35–43, February 2013. ISSN 0029-1277, 2224-7955. doi: 10.2166/nh.2012.166. URL <http://hr.iwaponline.com/content/44/1/35>.
- Wolff, M. A., Isaksen, K., Petersen-Øverleir, A., Ødemark, K., Reitan, T., and Brækkan, R. Derivation of a new continuous adjustment function for correcting wind-induced loss of solid precipitation: results of a Norwegian field study. *Hydrol. Earth Syst. Sci.*, 19(2):951–967, February 2015. ISSN 1607-7938. doi: 10.5194/hess-19-951-2015. URL <https://www.hydrol-earth-syst-sci.net/19/951/2015/>.
- Wood, N. B. *Estimation of snow microphysical properties with application to millimeter-wavelength radar retrievals for snowfall rate*. Ph.D., Colorado State University, 2011. URL [https://dspace.library.colostate.edu/bitstream/handle/10217/48170/Wood\\_colostate\\_0053A\\_10476.pdf?sequence=1&isAllowed=y](https://dspace.library.colostate.edu/bitstream/handle/10217/48170/Wood_colostate_0053A_10476.pdf?sequence=1&isAllowed=y).
- Wood, N. B., L'Ecuyer, T. S., Vane, D. G., Stephens, G. L., and Partain, P. Level 2c snow profile process description and interface control document. Technical Report, 2013. URL [http://www.cloudsat.cira.colostate.edu/sites/default/files/products/files/2C-SNOW-PROFILE\\_PDICD.P\\_R04.20130210.pdf](http://www.cloudsat.cira.colostate.edu/sites/default/files/products/files/2C-SNOW-PROFILE_PDICD.P_R04.20130210.pdf).
- Wood, N. B., L'Ecuyer, T. S., Heymsfield, A. J., and Stephens, G. L. Microphysical Constraints on Millimeter-Wavelength Scattering Properties of Snow Particles. *J. Appl. Meteor. Climatol.*, 54(4):909–931, January 2015. ISSN 1558-8424. doi: 10.1175/JAMC-D-14-0137.1. URL [http://journals.ametsoc.org/doi/10.1175/JAMC-D-14-0137.1](https://journals.ametsoc.org/doi/10.1175/JAMC-D-14-0137.1).

# APPENDIX A: FORWARD MODEL

## A.1 SCATTERING MODEL

**Table A.1.1:** Branched 6-arm spatial particle with porosities, 2D, mass oriented scattering scheme at 24.0GHz.  $\mathbf{r}$ , particle size of the snow particle;  $\mathbf{m}(\mathbf{r})$ , particle mass;  $\sigma_{\text{bk}}(\mathbf{r})$  and  $\sigma_{\text{ext}}(\mathbf{r})$ , backscattering and extinction cross-section, respectively.

$\mathbf{r}$ [ $\mu\text{m}$ ]	$\mathbf{m}(\mathbf{r})$ [kg]	$\sigma_{\text{bk}}(\mathbf{r})$ [ $\text{m}^{-2}$ ]	$\sigma_{\text{ext}}(\mathbf{r})$ [ $\text{m}^{-2}$ ]
35.27	$1.68529 \times 10^{-10}$	$8.85111 \times 10^{-17}$	$4.85381 \times 10^{-17}$
41.73	$2.79128 \times 10^{-10}$	$2.00612 \times 10^{-16}$	$1.28776 \times 10^{-16}$
47.87	$4.21355 \times 10^{-10}$	$4.792 \times 10^{-16}$	$2.9959 \times 10^{-16}$
53.76	$5.96809 \times 10^{-10}$	$1.02733 \times 10^{-15}$	$6.08871 \times 10^{-16}$
59.45	$8.07074 \times 10^{-10}$	$1.68272 \times 10^{-15}$	$1.09633 \times 10^{-15}$
70.34	$1.3368 \times 10^{-9}$	$5.7444 \times 10^{-15}$	$3.61096 \times 10^{-15}$
80.69	$2.01798 \times 10^{-9}$	$1.0899 \times 10^{-14}$	$6.93961 \times 10^{-15}$
90.63	$2.85939 \times 10^{-9}$	$2.244 \times 10^{-14}$	$1.42249 \times 10^{-14}$
100.20	$3.86421 \times 10^{-9}$	$3.7814 \times 10^{-14}$	$2.73019 \times 10^{-14}$
109.50	$5.04313 \times 10^{-9}$	$7.05869 \times 10^{-14}$	$5.36211 \times 10^{-14}$
118.60	$6.40785 \times 10^{-9}$	$1.16874 \times 10^{-13}$	$9.74644 \times 10^{-14}$
127.40	$7.94266 \times 10^{-9}$	$1.67227 \times 10^{-13}$	$1.56602 \times 10^{-13}$
144.50	$1.15894 \times 10^{-8}$	$3.41952 \times 10^{-13}$	$4.19048 \times 10^{-13}$
160.90	$1.60002 \times 10^{-8}$	$7.30397 \times 10^{-13}$	$1.05187 \times 10^{-12}$
176.80	$2.12278 \times 10^{-8}$	$1.13638 \times 10^{-12}$	$2.00359 \times 10^{-12}$
192.30	$2.73147 \times 10^{-8}$	$2.05333 \times 10^{-12}$	$3.63531 \times 10^{-12}$
236.50	$5.08103 \times 10^{-8}$	$5.94138 \times 10^{-12}$	$1.5256 \times 10^{-11}$
278.10	$8.26154 \times 10^{-8}$	$1.57715 \times 10^{-11}$	$4.31927 \times 10^{-11}$
317.70	$1.23171 \times 10^{-7}$	$3.68719 \times 10^{-11}$	$9.71916 \times 10^{-11}$
355.80	$1.73012 \times 10^{-7}$	$6.46005 \times 10^{-11}$	$1.89057 \times 10^{-10}$
392.60	$2.32439 \times 10^{-7}$	$1.29191 \times 10^{-10}$	$3.5246 \times 10^{-10}$
428.20	$3.01577 \times 10^{-7}$	$1.7526 \times 10^{-10}$	$5.67393 \times 10^{-10}$
463.00	$3.81242 \times 10^{-7}$	$3.58177 \times 10^{-10}$	$8.76374 \times 10^{-10}$
496.90	$4.71265 \times 10^{-7}$	$5.86279 \times 10^{-10}$	$1.30417 \times 10^{-9}$

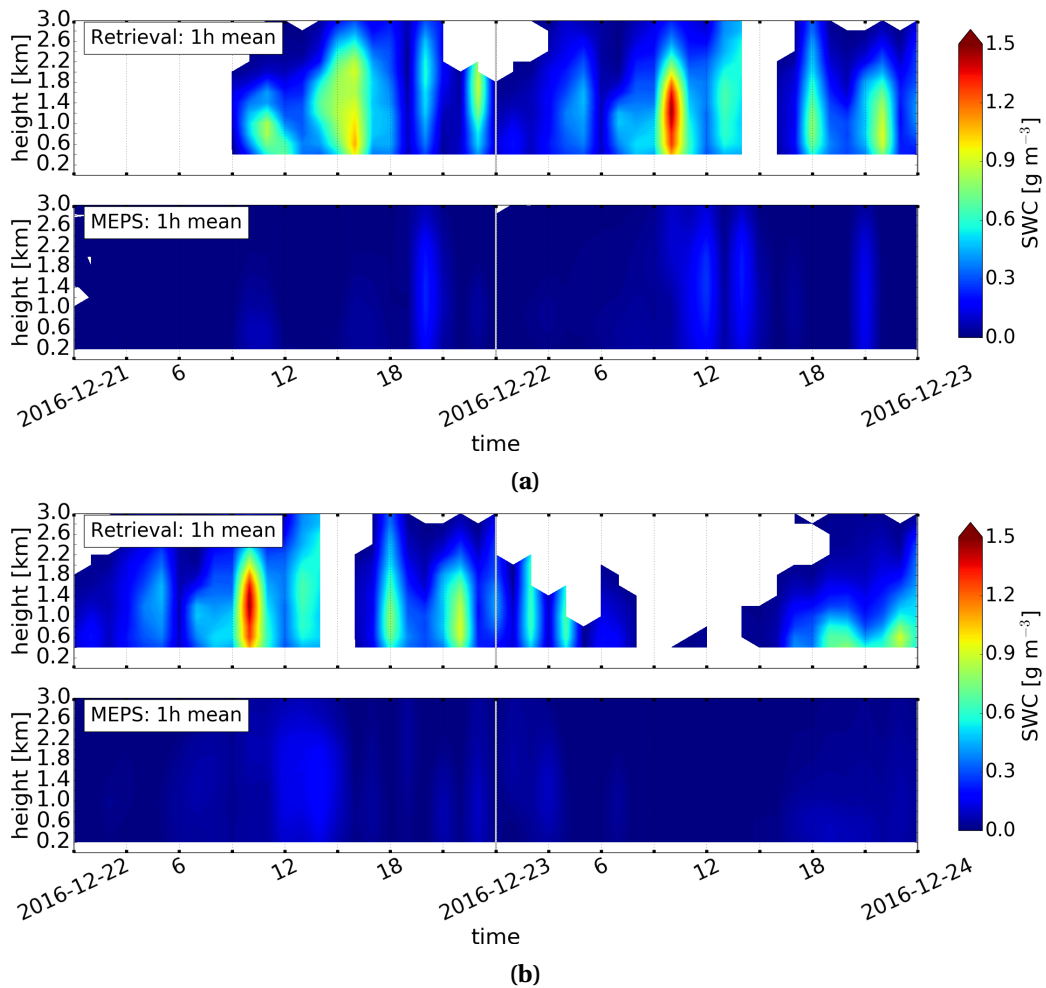
*Continued on next page*

Table A.1.1 *Continued from previous page*

<b>r</b> [μm]	<b>m(r)</b> [kg]	<b>σ<sub>bk</sub>(r)</b> [m <sup>-2</sup> ]	<b>σ<sub>ext</sub>(r)</b> [m <sup>-2</sup> ]
530.10	$5.72178 \times 10^{-7}$	$8.50141 \times 10^{-10}$	$1.8862 \times 10^{-9}$
562.60	$6.84002 \times 10^{-7}$	$1.04566 \times 10^{-9}$	$2.60854 \times 10^{-9}$
594.50	$8.07074 \times 10^{-7}$	$1.54514 \times 10^{-9}$	$3.68176 \times 10^{-9}$
625.80	$9.41379 \times 10^{-7}$	$1.61704 \times 10^{-9}$	$4.48578 \times 10^{-9}$
656.60	$1.08733 \times 10^{-6}$	$2.10709 \times 10^{-9}$	$5.71184 \times 10^{-9}$
687.00	$1.24546 \times 10^{-6}$	$3.31567 \times 10^{-9}$	$7.85938 \times 10^{-9}$
717.00	$1.41584 \times 10^{-6}$	$3.73598 \times 10^{-9}$	$9.50817 \times 10^{-9}$
746.50	$1.59789 \times 10^{-6}$	$4.40591 \times 10^{-9}$	$1.14824 \times 10^{-8}$
775.60	$1.79214 \times 10^{-6}$	$5.1432 \times 10^{-9}$	$1.37371 \times 10^{-8}$
804.40	$1.99928 \times 10^{-6}$	$4.21261 \times 10^{-9}$	$1.59603 \times 10^{-8}$
832.90	$2.2194 \times 10^{-6}$	$7.0875 \times 10^{-9}$	$1.90438 \times 10^{-8}$
861.10	$2.45255 \times 10^{-6}$	$7.606 \times 10^{-9}$	$2.17023 \times 10^{-8}$
888.90	$2.69784 \times 10^{-6}$	$9.61605 \times 10^{-9}$	$2.52476 \times 10^{-8}$
916.50	$2.95703 \times 10^{-6}$	$1.20108 \times 10^{-8}$	$2.91329 \times 10^{-8}$
943.80	$3.22922 \times 10^{-6}$	$1.29326 \times 10^{-8}$	$3.30911 \times 10^{-8}$
970.80	$3.51437 \times 10^{-6}$	$1.53246 \times 10^{-8}$	$3.82595 \times 10^{-8}$
997.60	$3.81353 \times 10^{-6}$	$1.32687 \times 10^{-8}$	$4.344 \times 10^{-8}$

## APPENDIX B: MEPS SNOW WATER CONTENT

### B.1 ENSEMBLE MEAN: DETERMINISTIC AND FIRST PERTURBED MEMBER



**Figure B.1.1:** From upper to lower: Hourly averaged retrieved and hourly instantaneous ensemble mean forecast of deterministic and first ensemble member. Initialised 21 December 2016 and 22 December 2016 at 0 UTC. Shading according to the colour-bar.

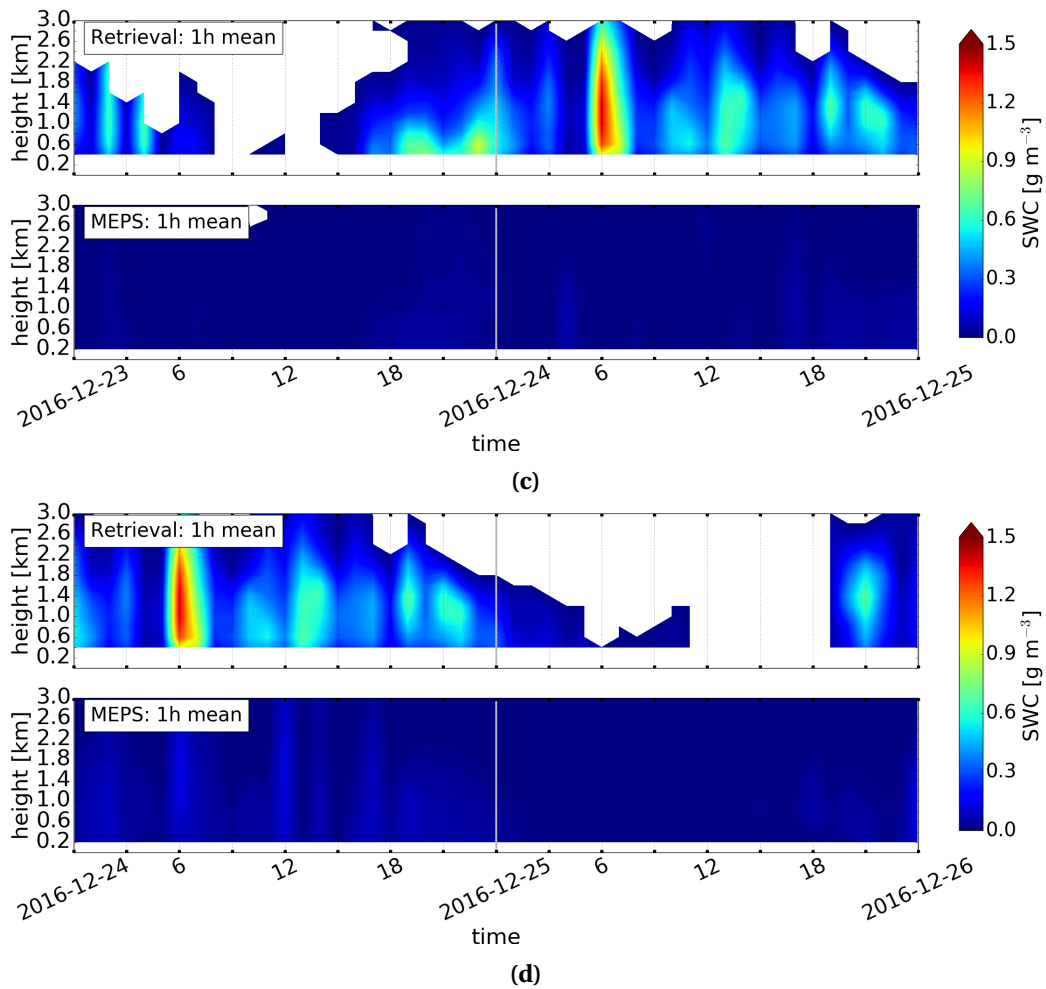


**Figure B.1.1:** (Continued from previous page.) Initialised 23 December 2016 and 24 December 2016 at 0 UTC.

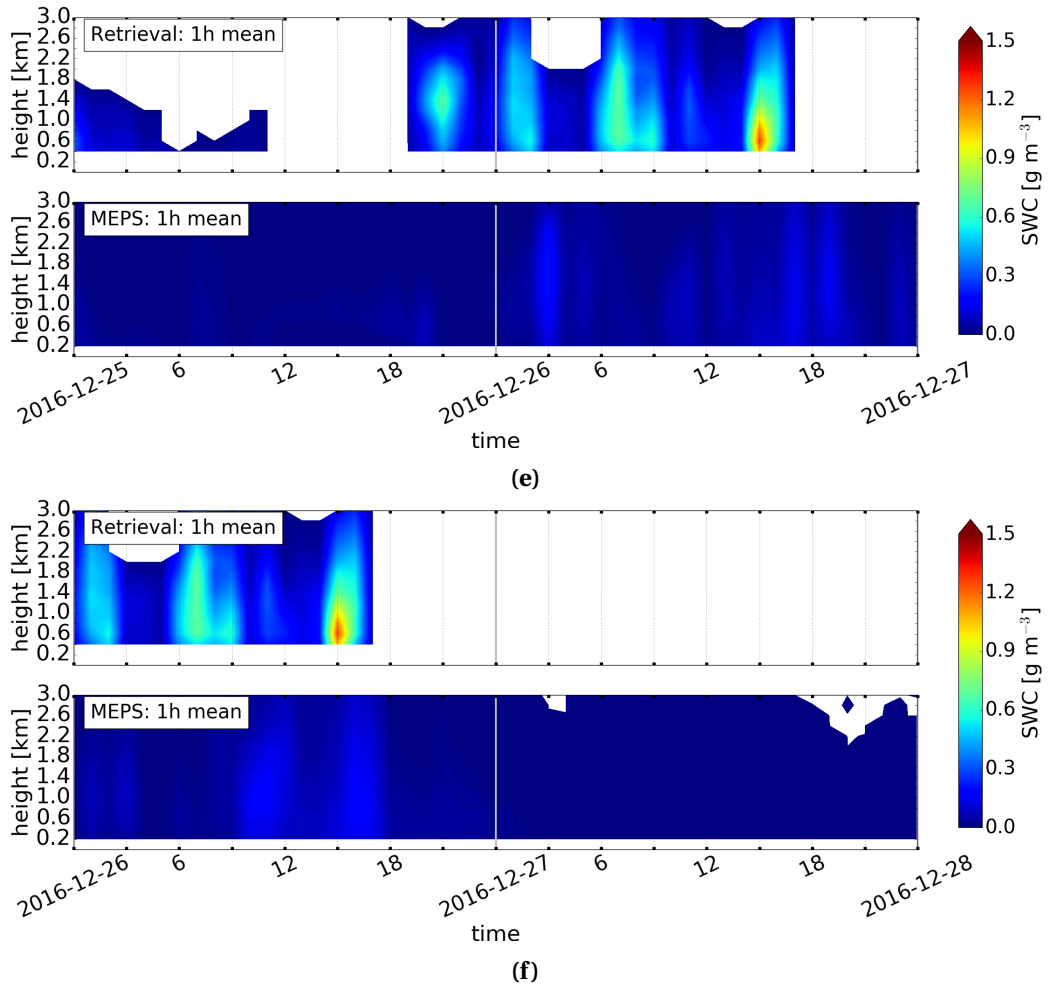
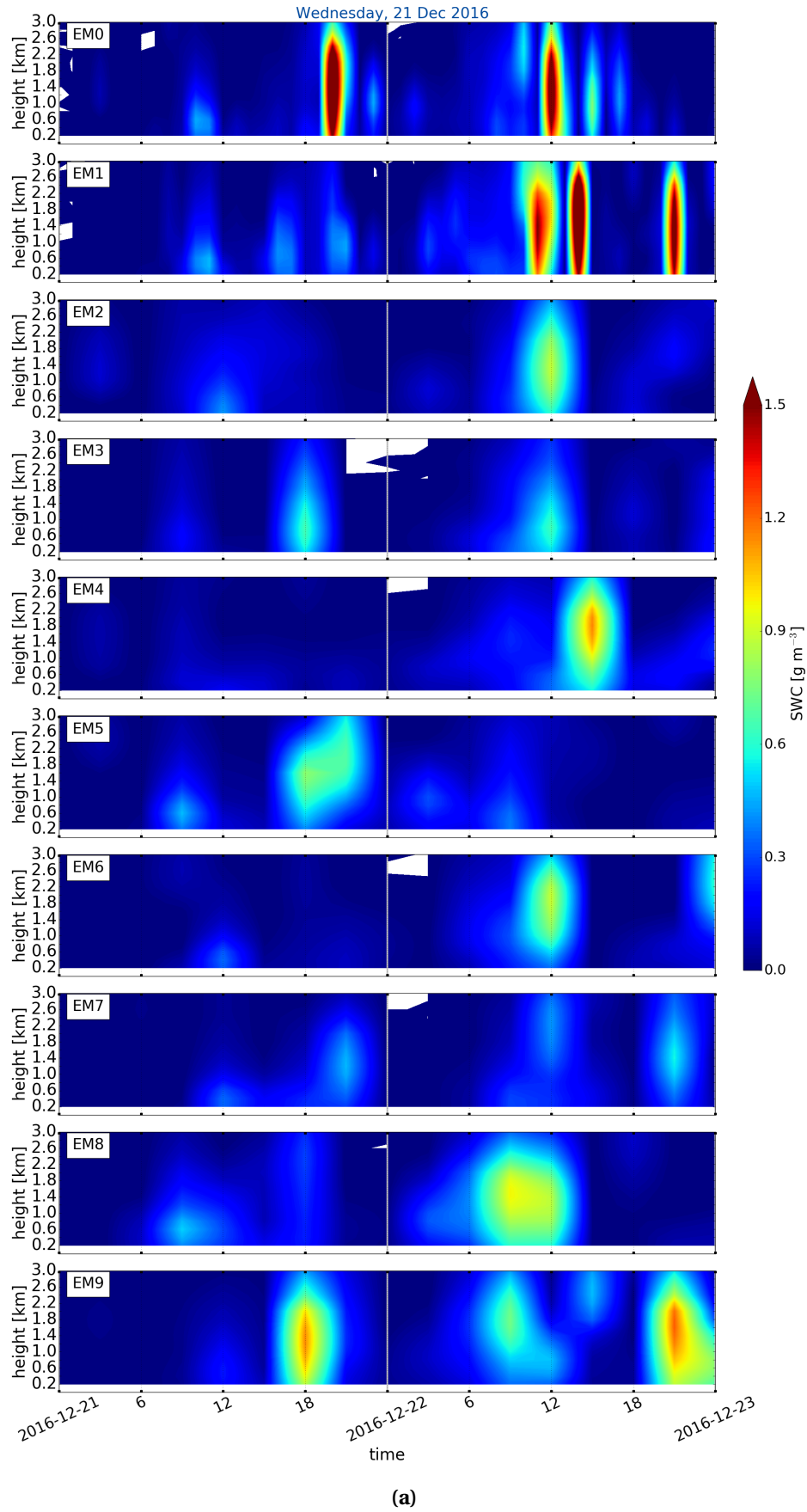


**Figure B.1.1:** (Continued from previous page.) Initialised 25 December 2016 and 26 December 2016 at 0 UTC.

## B.2 ALL ENSEMBLE MEMBER



(a)

**Figure B.2.1:** Snow water content of each individual ensemble member forecast for 48 h. EM0 is the deterministic forecast and EM1 to EM9 are the associated perturbed ensemble member. Shading according to the colour-bar. Initialised 21 December 2016 at 0 UTC.

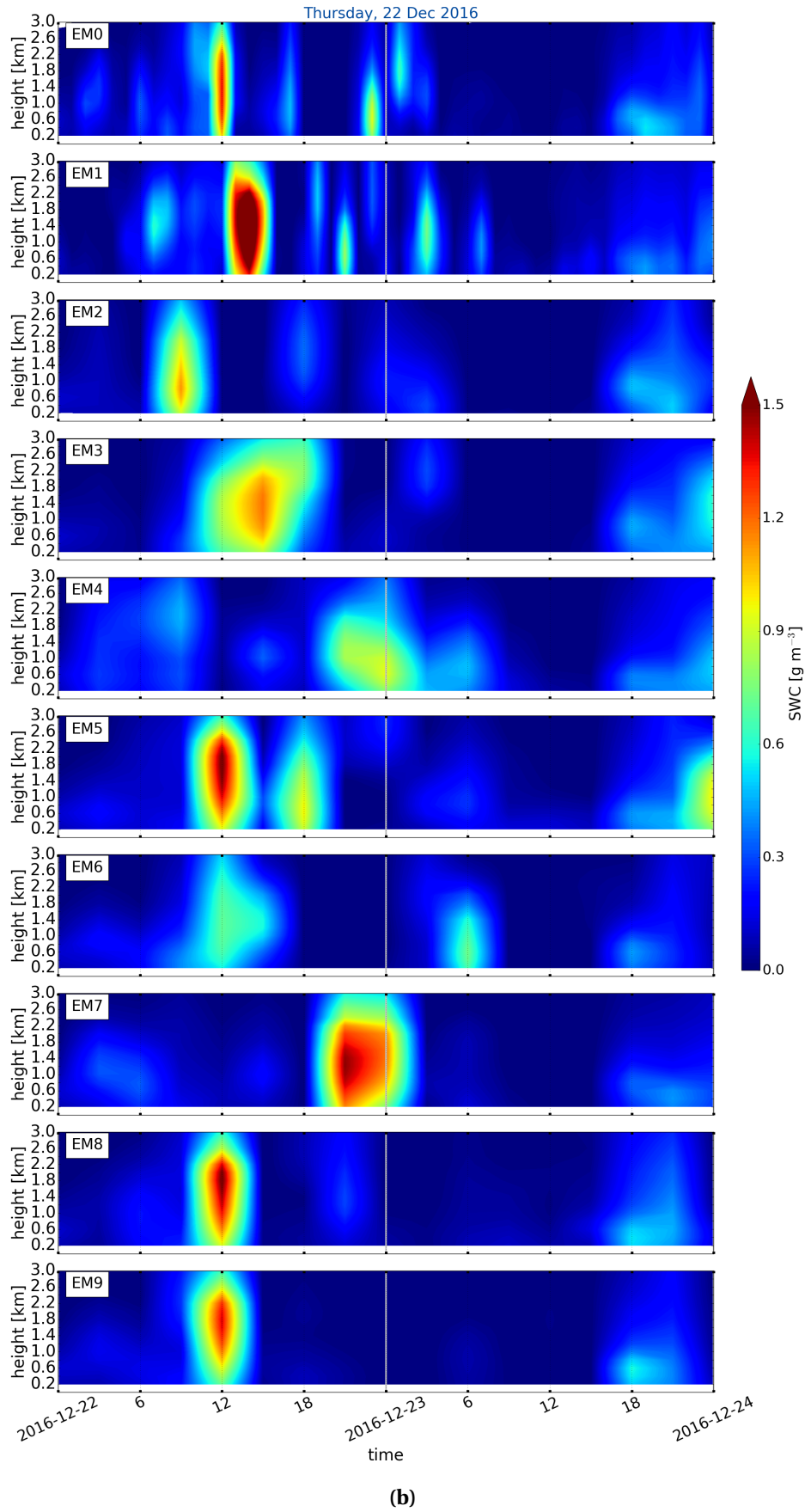


**Figure B.2.1:** (Continued from previous page.) Initialised 22 December 2016 at 0 UTC.

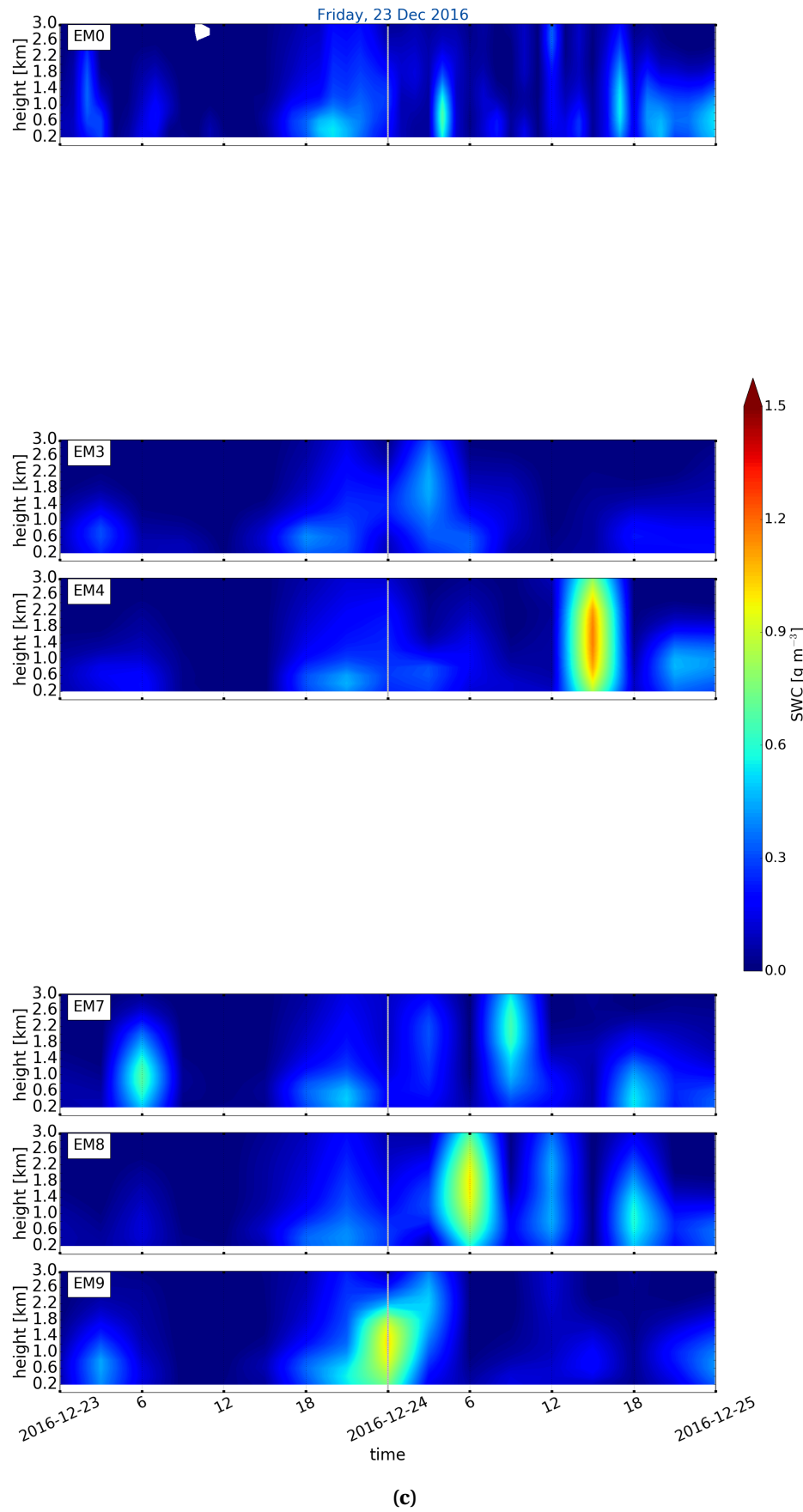


**Figure B.2.1:** (Continued from previous page.) Initialised 23 December 2016 at 0 UTC.

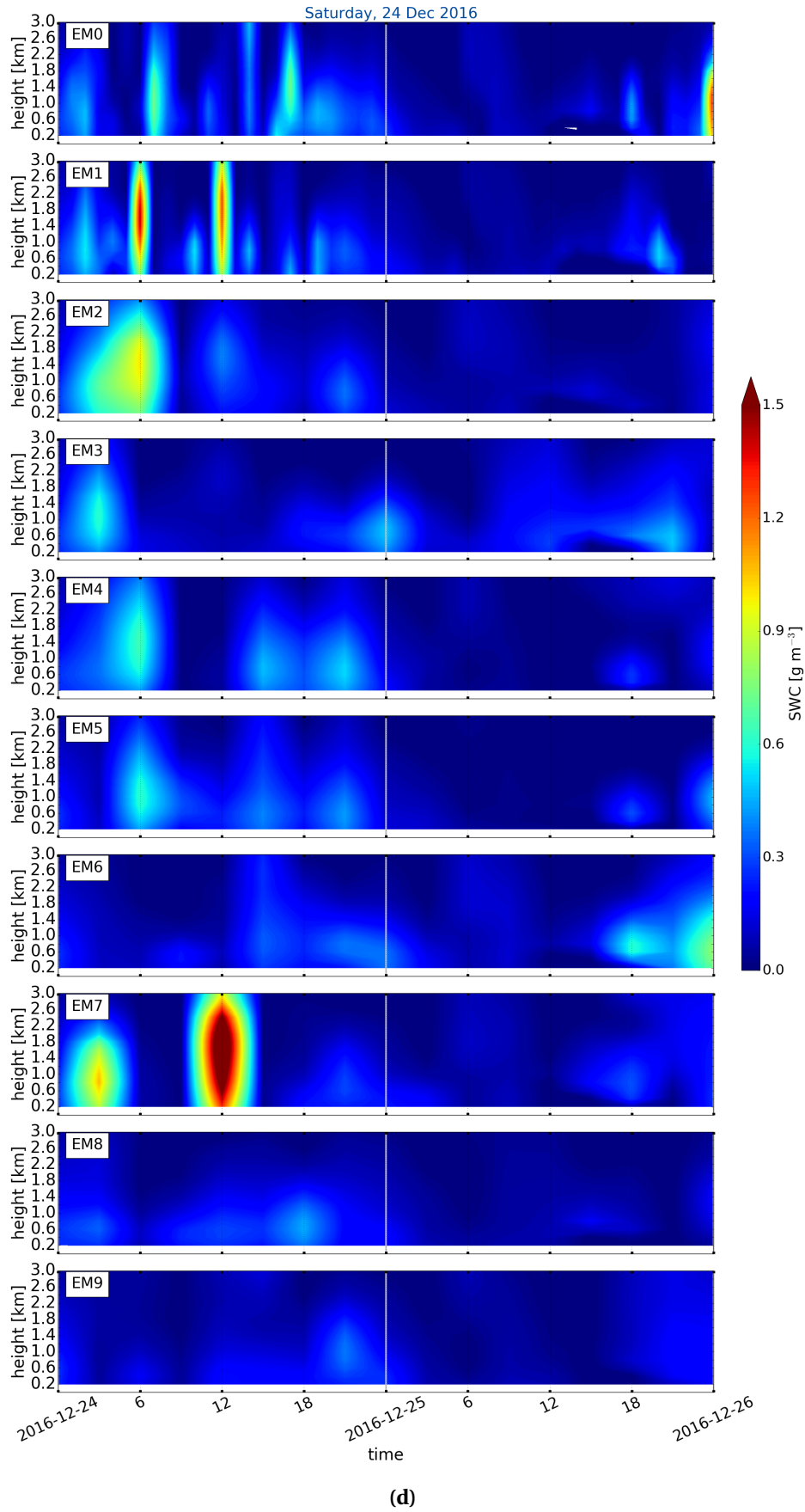


**Figure B.2.1:** (Continued from previous page.) Initialised 24 December 2016 at 0 UTC.

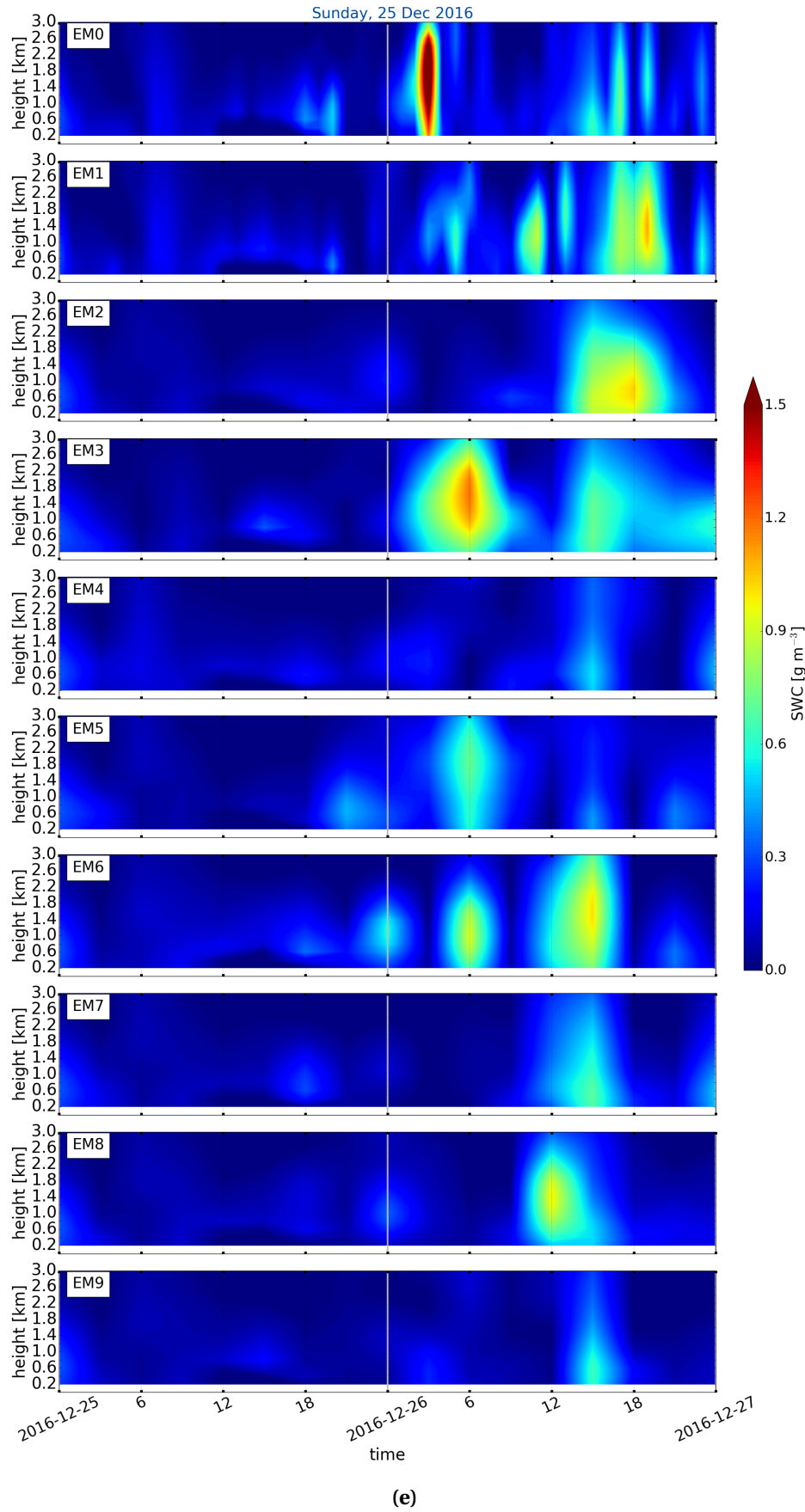


**Figure B.2.1:** (Continued from previous page.) Initialised 25 December 2016 at 0 UTC.

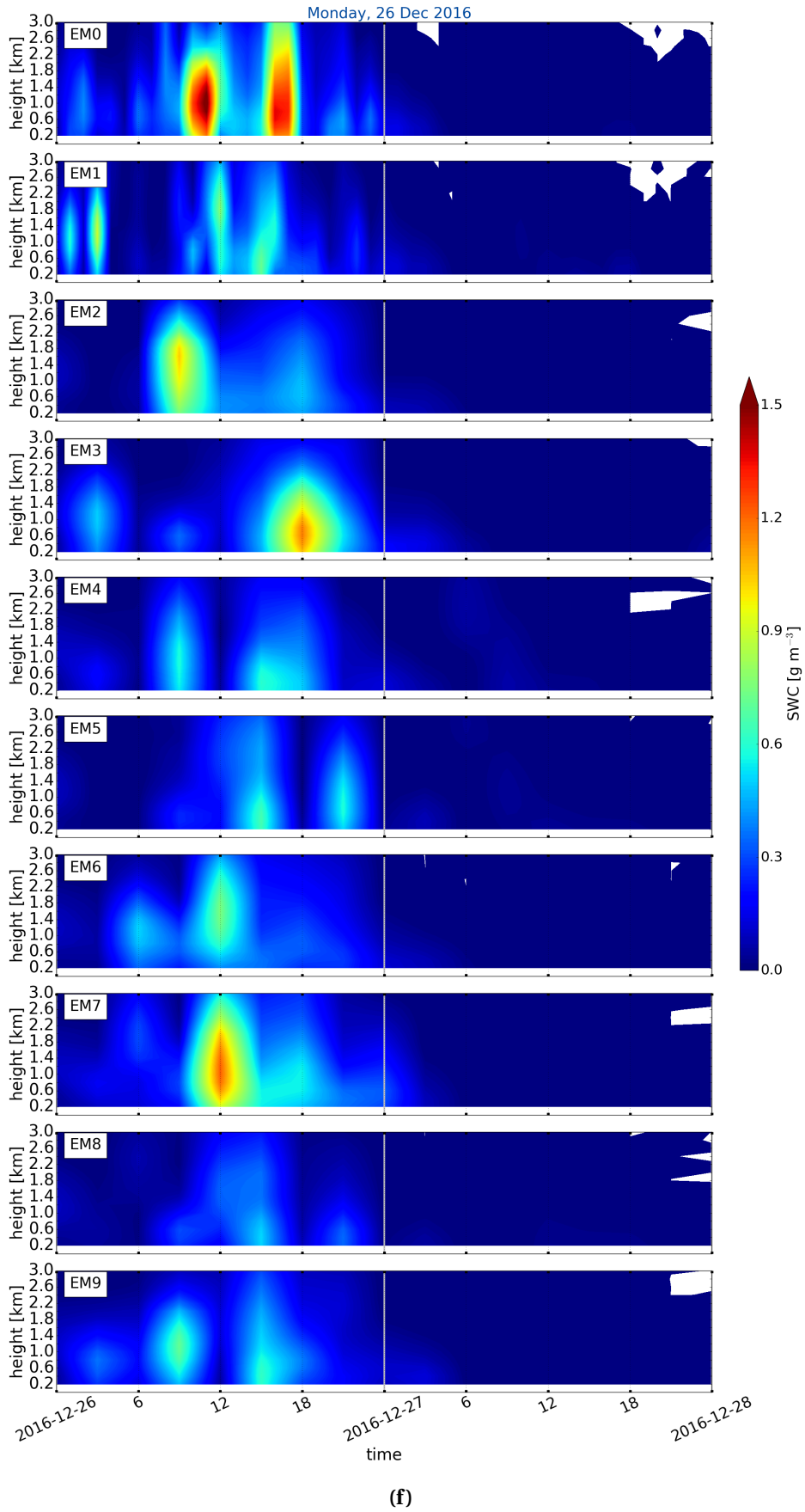


**Figure B.2.1:** (Continued from previous page.) Initialised 26 December 2016 at 0 UTC.

## ACKNOWLEDGEMENT

First and foremost, I would like to thank my supervisor, Richard Moore, for helpful discussions and giving me the opportunity to work with an interesting thesis. I would also like to thank my co-supervisor, Steve Cooper, for all the help with the optimal estimation retrieval, good guidance and scientific discussions. A big thank goes to Bjørg Jenny Kokkvoll Engdahl for all the help to understand the ensemble prediction model and for helping me with miscellaneous questions I had throughout the year. I would also like to thank Kirstin Krüger for her large effort in giving me constructive and detailed feedback on my scientific writing, and discussing results in the last minute.

I want to thank my fellow students at MetOs for a nice environment and good social and professional conversations. I also want to thank all the other friends I met during my studies in Germany and during my exchange at UNIS. It would not have been the same without you.

A very special thank you goes to all my good old friends and my family in Germany, who were always there for me and have supported and encouraged my choices all times. Last but not least, thanks to Dag Åsbø for proofreading, scientific discussions and listening to my complaints during time of frustration.



## DECLARATION

I hereby declare that except where specific reference is made to the work of others, the contents of this thesis is made independently. I have explicitly marked all material which has been quoted either literally or by content from the used sources.

Furthermore, I certify that this research thesis or any part of it has not been previously submitted for a degree or any other qualification at the University of Oslo or any other institution in Norway or abroad.

Franziska Hellmuth  
Oslo, June 2018